Optofluidic Applications of Diblock Copolymer Derived Nanoporous Polymers

Gopalakrishnan, Nimi; Kristensen, Anders; Christiansen, Mads Brøkner

Publication date:
2011

Document Version
Publisher's PDF, also known as Version of record

DTU Nanotech
Department of Micro- and Nanotechnology

Ph.D. Thesis

Optofluidic applications of diblock copolymer derived nanoporous polymers

Nimi Gopalakrishnan

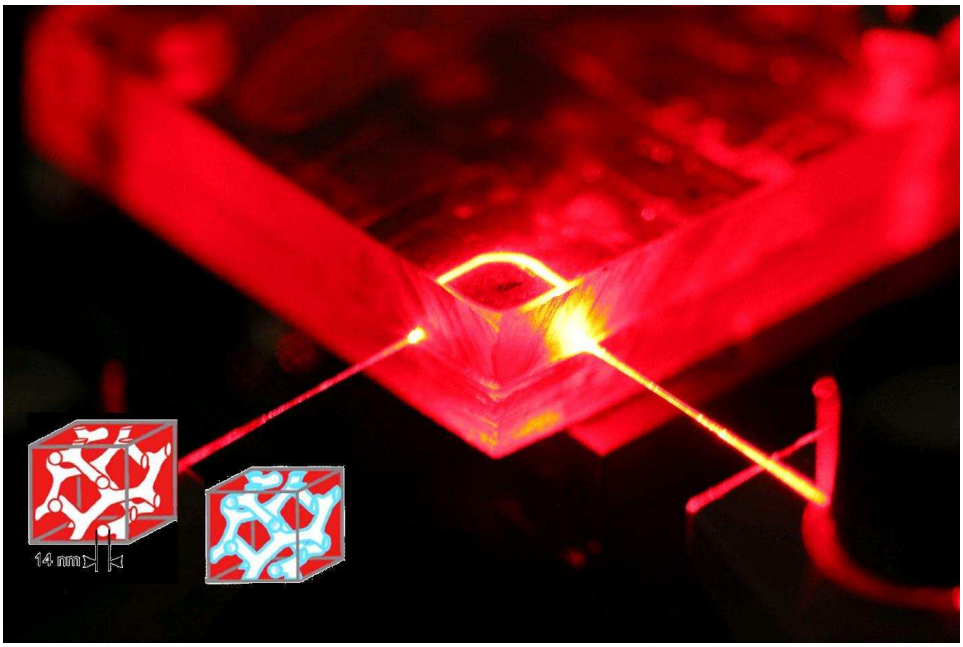

Supervisor: Anders Kristensen

Department of Micro- and Nanotechnology
Technical University of Denmark

31 May 2011

Abstract

To confine light in a liquid and thereby form a liquid core waveguide, the surrounding cladding materials must have a lower refractive index than the liquid core. In the context of biosensing, it is a challenge to obtain the right cladding material, as most of the relevant liquids are aqueous and have refractive index around 1.33 i.e. close to water, the earth's most abundant liquid. The objective of this Ph.D study is to design and develop a liquid core waveguide platform from nanoporous polymer materials rendering refractive indices below 1.33, and to investigate the optical waveguiding in these devices.

Nanoporous materials with refractive index below 1.33 are obtained from self assembling polymers called block copolymers by selectively etching one of the polymer blocks from the self assembly. The effective index of the porous material is a weighted average of the refractive indices of the polymer and air in the self assembly. Using UV-assisted surface modification, the hydrophobic nanoporous materials are selectively made hydrophilic. On infiltration with water, the pores in the UV exposed region are filled, thereby increasing the effective index in these regions by a value of δn=0.17. The index contrast is exploited to confine light in the exposed infiltrated regions. As light and liquid are confined in the same volume and the scale of heterogeneity in these regions are lower than the guided wavelength, they form solid-liquid core waveguides.

Two different surface modification methods have been tried: photo-oxidation and thiol-ene click chemistry. The former uses UV irradiation in presence of oxygen to hydrophilize the polymer surfaces, while the latter grafts functional groups onto the polymer. To perfom thiol-ene chemistry, two thiols: mercaptosuccinic acid (MSA) and sodium mercaptoethanesulfonate (MESNA) are used. The prepared devices are characterized by measuring their propagation loss using substitution method. A propagation loss of 0.62$\pm$0.03 dB/mm are obtained in the photo-oxidation modified waveg-

uides. The MSA and MESNA modified waveguides yield a propagation loss of 0.26±0.05 dB/mm and 0.54±0.05 dB/mm respectively.

Nanofiltering via integrated liquid core waveguides is also demonstrated and described in this PhD thesis. With fluorescence spectroscopy and microscopy it is proved that large particle ≈ 22 nm fluorescing beads are restricted from entering the waveguides, while small molecules (Rhodamine B) uniformly penetrate. Nanoporous liquid core waveguides can thus exclude scattering particles, making them an ideal integrated platform for analysis of turbid solutions like blood or milk. We explore the example of filtering large fatty particles (≈2 μm) from milk.

These developed waveguiding particle filters can be a promising platform for optofluidic and biosensing applications.

Resumé

For at lede lys i en væskekanal, og dermed forme en lysleder med flydende karne, er det nødventigt at det materiale der danner kappen har lavere brydningsindex end den flydende kerne. Inden for biodetektion er det en udfordring at finde det rette materiale til kappen, fordi analytten typisk er vandbaseret, og derfor har et brydningsindex omkring 1.33, altså tæt på vands, jordens mest udbredte væske. Målet med arbejdet bag denne afhandling var at designe og udvikle en platform for bølgeledere med flydende kerne, baseret på nanoporøse polymerer, som kan have brydningsindex under 1,33, og undersøge de fabrikerede bølgelederes optiske egenskaber.

De nanoporøse materialer med brydningsindex under 1.33 fremstilles af selvstrukturerede polymerer, såkaldte blok co-polymerer, ved selektivt at ætse den den ene polymerblok. Det effektive brydningsindex af det porøse materiale er et vægtet gennemsnit af brydningsindexerne af polymeren og luften i porerne. Ved at lave en UV-assisteret overflademodifikation kan man selektivt gøre de hydrofobe porer hydrofile. Når der trænger vand ind i de UV-belyste områder øges det effektive brydningsindex med δn=0.17. Denne indexkontrast bliver udnyttet til at lede lyset i de eksponerede og væskefyldte regioner. Da lyset og væsken er fanget i de samme områder, og længdeskalaen for den heterogeniteten er langt kortere end lysets bølgelængde, danner de lysledere med porøse kerner.

To forskellige metoder til overflademodification er blevet brugt: Fotooxidation og thiol-ene kemi. Førstnævte metode bruger UV belysning under tilstedeværelse af oxygen til at gøre polymeroverfladerne hydrofile, mens den sidstnævnte binder funktionelle grupper direkte til polymeren. Til thiol-ene kemien er der brugt to thiolmolekyler: Mercaptoravsyre (MSA) og mercaptoethansulfonsyre natrium salt (MESNA). De fremstillede bølgeledere er karakteriseret ved at måle udbredelsestabet ved substitutionsmetoden. Tab på 0.62±0.03 dB/mm er opnået i de fotooxiderede bølgeledere. De MSA- og MESNA-modificerede bølgeledere havde tab på hhv. 0.26±0.05 dB/mm

og 0.54±0.05 dB/mm.

Nanofiltrering i bølgelederne er også demonstreret og beskrevet i denne PhD afhandling. Med fluorescens-spektroskopi og -mikroskopi er det vist at større partikler (≈22 nm fluorescerende kugler) ikke kan trænge ind i bølgelederne, mens små molekyler (Rhodamin B) fordeler sig jævnt i dem. Nanoporøse bølgeledere med flydende kerne kan altså udelukke partikler som spreder synligt lys, hvilket gør, at de er en ideel integreret platform til at analyserer uigennemsigtige væsker som blod eller mælk. I denne afhandling bruges filtrering af fedtpartikler (≈2μm) fra mælk som demonstrationseksempel.

De udviklede bølgeledende partikelfiltre kan være en lovende platform til anvendelser inden for optofluidik eller biodetektion.

Acknowledgement

I would like to extend my gratitude to all those who has either directly or indirectly contributed towards the success of my doctoral study at the Technical University of Denmark. First and foremost, I would like to thank my PhD supervisor Dr. Anders Kristensen for guiding and training me as a researcher. His timely suggestions and reminders has helped me to stay in track with the research. I also would like to thank my co-supervisor Dr. Peter Thomsen, who helped me with a better understanding of the biological problem we were looking into. I sincerely thank my co-supervisor Dr. Mads Brøkner Christiansen for his enthusiasm and encouragement during the project. I also thank him for patiently bearing me and enlightening me whenever I showed up at his office door with my doubts. I would also like to sincerely thank all my colleagues in the Optofluidics group especially Dr. Cameron Smith. He is a good friend and officemate, who always gave positive feedback and a patient ear to my bad mood braggings.

Thanks to Kaushal S Sagar and Anton Berthold, my colleagues as well as good friends, without whom this thesis would not have been in its present form. I thankfully acknowledge the support given by Dr. Sokol Ndoni without whom getting aquainted with the chemisty in the project would have been a nightmare for me.

I also would like to thank my friends, Dr. Irene Fernandes Cuesta, Jesper Kenneth Olesen and Anna Chiara Brunetti, who always helped me ease out the stress over a beer. I am also grateful to my colleagues at DTU Nanotech for providing me with a wonderful working environment.

I use this opportunity to thank my wonderful family, my dad, mom and my sweet sister who loved me, supported me and above all been with me throughout best and worst moments in my life. Last, but not least, I would like to thank my sweetheart Vinu, who encouraged, inspired and supported me to chase my dream. Thank you Vinu, for making me feel always strong.

Nimi Gopalakrishnan
Lyngby, 30 May 2011

Contents

List of Figures

List of Tables

Abbreviations and Symbols

Abbreviation	**Description**
ARROW	Anti Resonant Reflecting Optical Waveguides
BCC	Body Centered Cubic
CA	Contact Angle
D_3	Cyclosiloxane
DCP	Dicumylperoxide
DI	De-Ionized
DMPA	2-dimehoxy-2-phenyl acetophenone
FEP	Fluorinated Ethylene Propylene
FTIR	Fourier Transform Infra Red
HC-PCF	Hollow Core Photonic Crystal Fibers
L^2	Liquid-Liquid
LCW	Liquid Core Waveguide
MESNA	Sodium Mercaptoethanesulfonate
MM	Multi Mode
MSA	Mercaotosuccinic Acid
MVD	Molecular Vapour Deposition
NA	Numerical Aperture
NP	Nanoporous Polymer
ODT	Order disorder temperature
OOT	Order order temperature
PB	Polybutadiene
PCF	Photonic Crystal Fibers
PDMS	Polydimethylsiloxane
PI	Photo Initiator
PL	Propagation Loss
RI	Refractive Index
RIE	Reactive Ion Etching
SEM	Scanning Electron Microscope
SLCW	Solid-Liquid Core Waveguide
SOI	Silicon On Insulator

TBAF	Tetrabutylammoniumfluoride
TE	Transverse Electric
THF	Tetrahydrofuran
TIR	Total Internal Reflection
TM	Transverse Magnetic
UV	Ultra Violet

Symbol	Description	Unit
$\mathbf{r}$	Position vector	m
x, y, z	Position coordinates	m
θ	Angle of incidence	rad or $^\circ$
$\mathbf{E}$	Electric field vector	V/m
$\mathbf{K}$	Bloch wave vector	m^{-1}
n	Refractive index	
n_{eff}	Effective refractive index	
ε	Dielectric function	
ε_0	Vacuum permittivity	8.854×10^{-12} F/m
c	Speed of light in vacuum	299792458 m/s
ω	Wave frequency	rad/s
f	Volume fraction	%
λ	Vacuum wavelength	m
k	Vacuum wavenumber	m^{-1}
β	Propagation constant	m^{-1}
Φ_{RT}	Phase shift	rad
d_p	Penetration depth	m
c	Concentration	$\mathrm{mol/m}^3$
Λ	Periodicity	m
χ_N	Flory Huggins interaction parameter	

Chapter 1

Introduction

This Ph.D thesis provides the description of a liquid core waveguiding technology platform developed from diblock nanoporous polymers. The author has attempted to elucidate the underlying physical principles before outlining a proof-of-concept and fabrication procedure. This chapter is an introduction to the thesis.

For the last couple of decades the growing need for fast, efficient and low cost detection has led to developements in optical measurement techniques. The instrumentation used in traditional optical measurements has typically relied on bulk optics, with individual components at least several centimeters in size. Recent advancements in microfabrication techniques have enabled the dramatic scaling down of optical measurement systems that integrate multiple components onto small, planar chips where complex optical components can be confined to a plane of area less than a mm^2 of the chip [1]. Integrated optics has some compelling advantages compared to their bulk couterparts, offering a high degree of design flexibility and control. Compared to bulk optics, light can be delivered at desired amplitude and phase to any point in an integrated chip. The only limiting factor is the topological constraints in laying out elements on the chip surface [2].

Most integrated optical systems are made with solid materials [3]. Polymer materials are a prefered integrated biosensor substrate as they are transparent, compatible with bioassays and cost efficient to structure. In certain applications, however, it becomes advantageous to use fluids for optical systems, owing to the unique properties they possess. Examples of such properties include: a large variety of refractive indices and gain [4]; optically

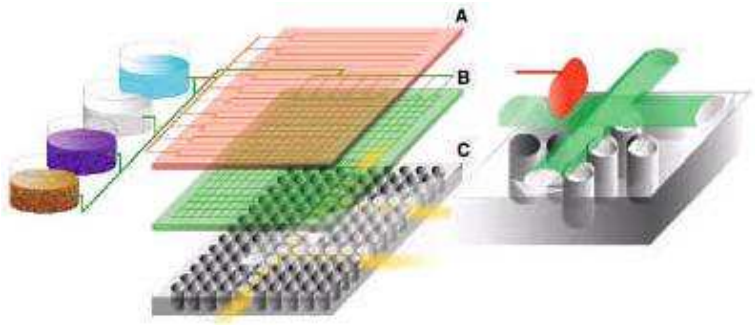

***Figure 1.1**: Optofluidic devices. (a) A layer for microfluidic controls, like microfluidic pumps or valves incorporated to this layer; (b) microfluidic channel layer; (c) Layer with optical structure like waveguide, photonic crystal structure etc. Light is guided in this layer (adapted from [3]).*

smooth interfaces for making low loss devices [5]; ability to suspend complex mixtures of particles with optical relevance (quantum dots, nanoparticles, fluorescent dyes etc.) [6] and appropriate diffusion parameters to form controlled gradients of optical characteristics. Thus, the physical properties of fluids confined on micro/nanoscales are used to make functional devices. Optofluidics refers to the class of such integrated optical systems that incorporate the use of fluids for their function.

1.1 Optofluidics

Optofluidics combines optics and fluidics, opening new frontiers in developing optical systems [3]. Optofluidic devices can be broadly classified as (1) devices that exploit fluidic properties for making tunable, reconfigurable and adaptive optical elements and (2) devices that use optical effects to study or analyse the properties of fluids or biological solutions [7, 8]. Examples of optical elements already developed include tunable lenses [9, 10], waveguides, resonators [11], light sources [12] and optical switches [13]. Optofluidic devices that use optical effects to study the properties of fluids consists of three elements as shown in Fig. 1.1. A microfluidic channel that confines the fluidics in a microscale volume, a microfluidic control part which controls the flow and other physical properties of the fluid, and an optical structure that guides light [3]. Interaction between the optical field generated by the optical element and fluids form the basis of detection in these devices. In applications such as chemical and biosensing, highly sensitive detection demands maximum interaction between the probing element (optics) and fluids. When the fluidic channel and the optical element are seperate, sensing is done using evanescent coupling [14, 7, 15]. In these de-

vices, the evanescent field interacts with the fluid and is restricted over a short penetration depth of light, i.e. small interaction volume. To increase sensitivity, a possible method is to increase the optical pathlength but this often compromises compactness, ease of fabrication or cost of such devices. To maximize the interaction, the microfluidic channel and optical structure can be built as a single entity such that optical field and liquid is confined or guided in the same volume. Generally, strong mode confinement and guiding of light in a medium is obtained by surrounding the medium with lower refractive index materials. However, most available materials that confine fluids have a higher refractive index than the confined fluid. Thus when the medium to confine light becomes a fluid, choice of suitable surrounding materials are low. Liquid core waveguides (LCW) are a class of such devices that confine light and liquid in the same volume by solving this problem. In recent years, two main approaches have been developed to address the problem of confining light in liquid. On one hand, the development of low index materials, while on the other, different light confining and guiding principles are applied. Following this, LCWs can be broadly categorized based on their light confining properties either as index guided LCWs, or interference/reflection based LCWs. While index guided LCWs deal with difficulties in finding suitable materials for total internal reflection (TIR) based guiding, the other methods surpass this difficulty with different approaches like guiding light either along a low index medium surrounded by a high index clad or using multiple reflections such that the electromagnetic fields interfere constructively or desctructively.

In this project we have developed a technique such that light and fluid can be confined in the same physical volume. Fig. 1.2 gives a schematic representation of what is done in this project, highlighting novel aspects compared to available techiques. The approach to tackle the problem of confining light in liquid is to develop a low index material from diblock copolymers. The research in block copolymer chemistry is combined with UV lithography to develop an innovative platform for implementing liquid core waveguiding technology. Our material, nanoporous polymer is made from self assembled coblock polymers by selectively etching one of the block polymer. The nanoporous polymers fabricated are made surface wettable using UV induced chemistry. This allow confinement of light and liquid in the exposed region. Unlike available LCWs, where light is confined in the fluid, the developed technique confines light in a matrix of liquid and solid. This approach is therefore no longer restricted by choice of low index surrounding materials since light is not solely confined in the liquid.

The upcoming chapter in LCWs is intended as an overview of the available LCW technologies that address the problem of low index material requirements. A comparison of the LCW scheme presented in this thesis with competing technologies is provided.

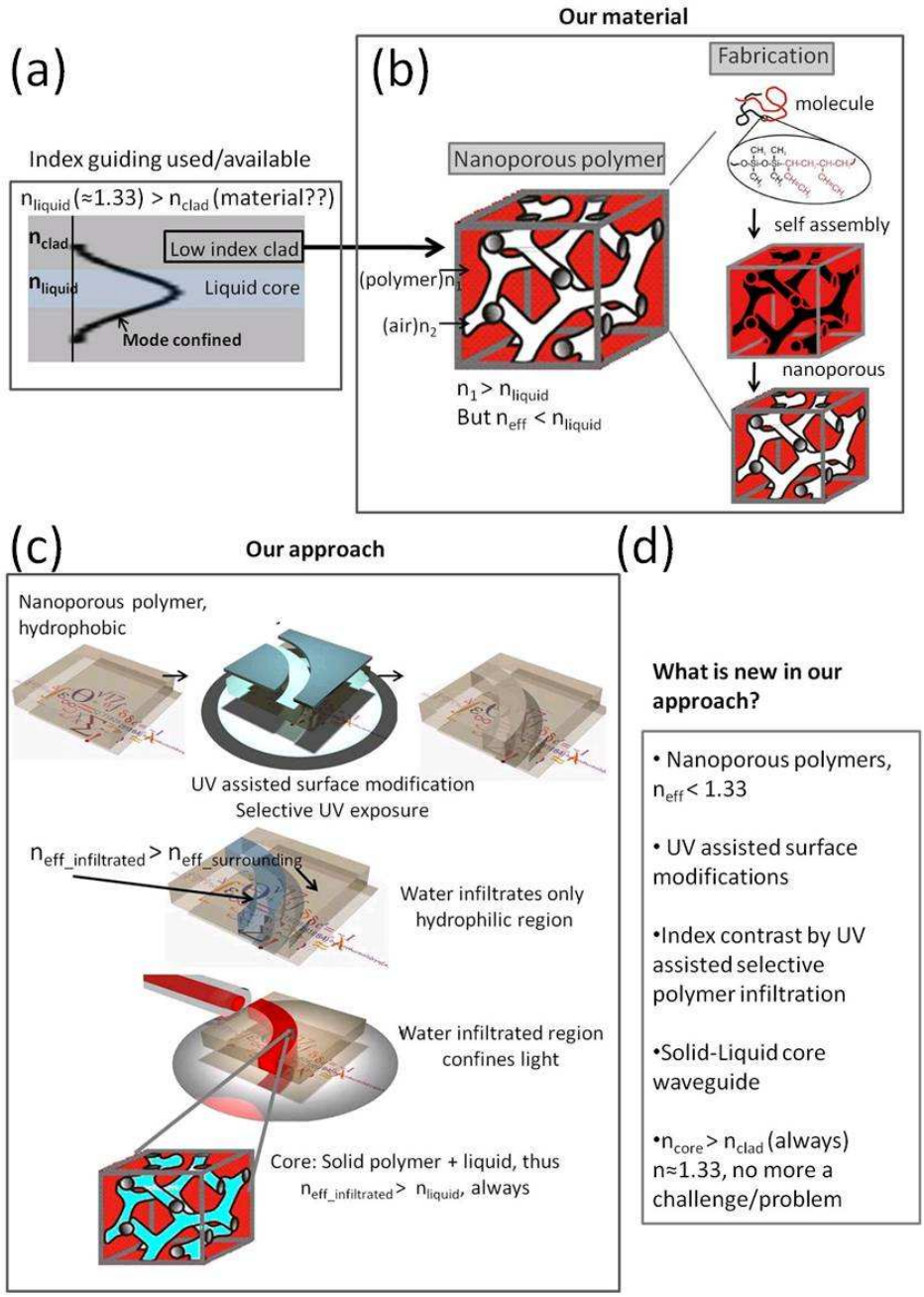

Figure 1.2*: Schematic representation of the liquid core waveguide technology presented in this PhD project. (a) The problem we are solving; (b) our material: a new LCW platform; (c) our approach: light and liquid confinement by UV assisted surface modification of the nanoporous polymer; (d) what is new in our approach.*

1.2 Objective

This PhD project is part of a project at the Technical University of Denmark: **Li**quid **Cor**e waveguide **T**echnology (LiCorT), funded by Danish council for Strategic Research (grant no. 09-063776/DSF). In past decades the developments in polymer materials and microfabrication techniques have resulted in research and applications to develop polymer-based medical apparatus and devices. The LiCorT project aims to combine state-of-the-art research in block copolymer chemistry, UV lithography and optofluidics to make polymer based LCW sensors for medical diagnostics. The material design, synthesis and modification of nanoporous materials to prepare polymeric components were developed by LiCorT project partners from DTU Nanotech under Dr. S. Ndoni's leadership. Cleanroom compatible processes for fabricating surface modified nanoporous polymer, especially material properties and processing, was developed at the Danish Polymer Centre, DTU chemical Engineering by K. S. Sagar under guidance of Dr. S. Ndoni. The objective of this PhD thesis is to explore the potential of the diblock copolymer derived nanoporous polymer materials for liquid core waveguiding and other optofluidic applications. LCWs are designed and fabricated from nanoporous polymers by selectively surface modifying the developed nanoporous materials and their waveguiding properties are characterized. Optofluidic applications of these nanoporous polymer waveguide as LCWs are explored.

1.3 Outline of the thesis

This Ph.D thesis consists of seven chapters. The subsequent chapter 2 gives an outline of the competing technologies for the work in this thesis. The chapters 3, 4 and 5 are dedicated to discuss the theoretical background required to understand the project, fabrication and development of the materials used and characterization of the device fabricated respectively. The chapters 6 discuss some optofluidic applications for the devices developed and the thesis is concluded with a summary and possible future implications.

Chapter 2: This chapter gives a review of the current competing technologies for the presented work. The basic principles of LCW and the challenges faced are discussed with reference to available solutions for the problem presented. The chapter is structured based on the light guiding methods implemented in the state-of-the-art LCWs, especially addressing total internal reflection based guiding. This is concluded with references to the work presented in this thesis, especially, where nanoporous LCW development stands with respect to the current available technologies. The chapter is

mainly based on review articles and book chapters on optofluidic waveguides [16, 17, 18, 19].

Chapter 3: This chapter is intended to provide the theoretical background for the presented work. The chapter focuses on optical waveguide theory, in particular total internal reflection and mode confinement. The effective index in nanoporous polymers is detailed and derived in this chapter. In addition, the chapter also includes a section on attenuation in waveguides with an approach similar to the work presented. A discussion of optofluidic applications for the nanoporous materials is presented. Surace effects like contact angle and surface tension is also touched upon. For reference, the chapter is concluded by highlighting the relevant theory used in this work. The approach used in this chapter is based on book chapters [20, 21, 22, 23].

Chapter 4: This chapter contains a description of the fabrication procedures of nanoporous polymer waveguides developed in this project. These include fabrication of nanoporous polymers from starting materials of polybutadiene polydimethylsiloxane diblock copolymers. Each step of fabrication is explained with a brief introduction to the concepts and mechanisms used. The description of the nanoporous polymer fabrication is ended with a summary, where all the relevant fabrication parameters used in this project are given. The material design, synthesis, modification and process development was mainly performed by Lars Schulte, Anton Berthold (DTU Nanotech) and Kaushal. S. Sagar (DTU Chemical Engineering), and other partner members of the LiCorT project. The section of nanoporous polymer waveguides discusses how LCW waveguides are made from the developed nanoporous polymers. The process development and the surface modification was mainly done by Kaushal. S. Sagar (DTU Chemical Engineering).

Chapter 5: Characterization of the liquid core waveguiding in the developed nanoporous polymer waveguides is discussed in this chapter. The chapter is introduced with studies for checking the success of the chemistry used in the nanoporous LCWs. A note on why some modification approaches and chemistry was discarded is also given. Three different modification techniques are explained. Furthermore, all the approaches were compared and a most prefered mechanism is suggested. The chapter is summarized noting the relevant results obtained in the characterization. A table comparing the approaches can be referred to for a quick review. Some of the characterization approaches, especially checking the success of chemistry, was done in close collaboration with Kaushal. S. Sagar (DTU Chemical Engineering).

Chapter 6: The potential optofluidic applications of the nanoporous polymer waveguides are explored in this chapter. The chapter analyses the importance of combined filtering and waveguiding in optofluidic devices analysing turbid solutions. An optofluidic application is discussed where an existing problem can be solved using nanoporous polymer waveguides.

The nanofiltering approach does not require any additional processing for the materials, making it a very promising tool for a range of applications. Different analytical techniques and their results are also given. A more simple analytical technique is referenced with some discussion on why this method was not implemented in this work. The chapter is concluded giving all relevant achievements.

Chapter 7: This is the final chapter that concludes the thesis. All the relevant achievements in the PhD study are summarized. Some future prospects of NP based LCW technology are also discussed.

Chapter 2

Liquid core waveguides

This chapter reviews state-of-the-art in the field of liquid core waveguides (LCWs), especially their optical characteristics and challenges. The starting point of this review is a broad classification of LCWs based on their guiding principles followed by a detailed evaluation of index guided LCWs. This chapter aims at providing a review for state-of-the-art LCWs.

Bio and chemical sensing mainly use properties of fluids to extract important information regarding the probed system. Microfluidics-based sensors allow controlled manipulation of low volumes of fluids, providing an increased functionality to the devices. Integrating optical systems with fluids promises to enhance sensing and detection of these devices. Optofluidics, the integration of optics with fluidics, is an emerging field to this end. Fluid-based optical systems have many advantages as mentioned in Chapter 1. This allows fabrication of optical elements with added functionalities. However, high index materials surrounded by low index regions confine light strongly, and since there is an abundance of solid materials with appropriate indices to achieve this, integrated optical systems are typically formed in combinations of solids [24, 25]. Furthermore, most supporting microfluidic structures have higher index than the confined liquid, such as aqueous solutions/water ($n \approx 1.33$), causing light to be only weakely confined to the fluid volume. This is especially true in biosensing, where optical properties of the fluids closely compare to water ($n = 1.33$) as biological solutions are basically aqueous in nature.

As mentioned in Chapter 1, optofluidic devices have an optical structure which forms the optical element of the system and a fluidic structure that supports the fluids. Fig. 2.1 shows an optofluidic structure. Due to difficul-

ties in confining light in low index liquids, light is mainly confined in solid optical elements and is either evanescently coupled or delivered to the fluid [26, 27]. For evanescent coupling, the optical delivery elements can be bragg gratings [28], waveguides [29] or photonic crystals [7]. The interaction of the evanescent field with the fluid can be used to extract information. The larger the interaction between the field and fluid, the larger the sensitivity of the device. However, most of the light is confined in the solid element, the interaction between liquids and light is small (Fig. 2.2). To increase sensitiviy in evanescent sensors, one possible technique is to increase the optical path length. Unfortunately, this compromises ease of fabrication and cost, especially in devices that use optical structures like photonic crystals, gratings etc [30]. Waveguides, being the simplest optical element, can be made with long optical path lengths, but concede compactness. Optofluidic ring resonators solve these issues and are very effective evanescent sensors [31, 14, 15]. Despite their good performance, evanescent coupling based ring resonators are limited by the fluid-light interaction over a short penetration depth of light, ie, small interaction volume. Penetration depth, d_p defines the distance to which the bound waveguide mode extends beyond the confined/core-liquid material interface. This distance where the electric field amplitude drops to $\frac{1}{e}$ of its value at the interface can be written as

$$d_p = \frac{\lambda}{2\pi\sqrt{n_{eff}^2 - n_{fluid}^2}} \tag{2.1}$$

where λ is the wavelength of the guided light, n_{eff} is the effective refractive index of the confined waveguide mode (ref Chapter 3: Modes in planar waveguides) and n_{liquid} is the refractive index for the liquid layer analysed [32]. Fig. 2.2 shows optofluidic devices using evanescent based sensing.

Another technique to enhance sensitivity is direct coupling, where fluids and light are confined in the same space. Integration of liquid and optical elements in the same plane can make compact and robust optofluidic devices. Waveguides are the simplest optofluidic devices used for this purpose. Maximum integration and functionality will be possible if both light and liquid is guided through the same physical volume. However, as mentioned earlier, liquid based waveguiding is difficult to achieve due to the problem of finding a low index surrounding or cladding material. This is the main bottle neck that restricts wide scale implementation of such a sensitive method.

Liquid core waveguides (LCW) form a class of waveguides which use liquid as their core material for guiding light. Due to light and liquid confinement, small analyte volume, easy integration onto other optical chip devices, LCWs represent a very suitable technology for bio-sensing [18, 19]. In recent years, many advancements occured in the field of LCWs which in particular address the problem of finding a low index cladding material. These devices

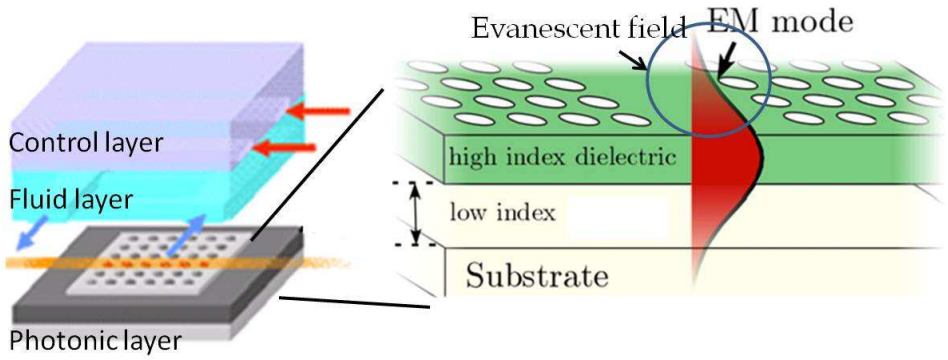

***Figure 2.1**: Optofluidic elements. The photonic layer/optical element confines light in a high index dielectric. The evanescent tail in the low index regions interact with fluids. Figure adapted from http://www.mae.cornell.edu/erickson/research.html*

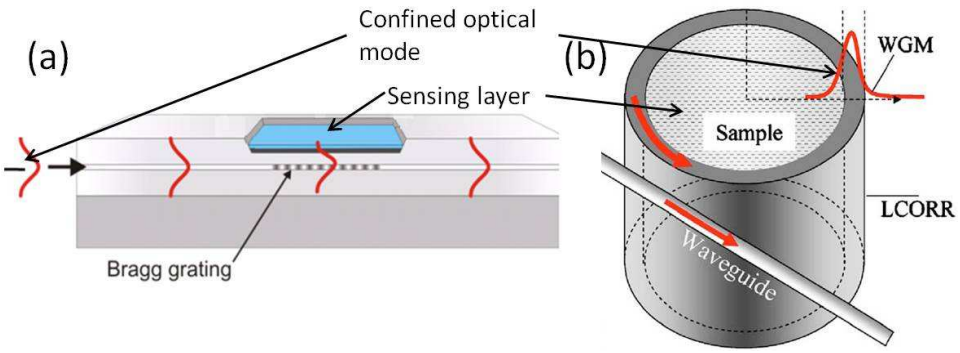

***Figure 2.2**: Evanescent based sensing in optofluidic devices. (a) Optical element used is Bragg grating. The evanescent tail at the low index regions interact with samples [28]; (b) ring resonators [33].*

operate based on index guiding principles where light is confined in liquids surrounded by low index index materials. In addition to these, some LCWs confine light in liquids surrounded by high index materials. This is achieved by adapting different light guiding and confining principles than index guiding. These devices with different guiding principles are not restricted by the problem of finding a suitable low index cladding layer as for index guided waveguides.

As the LCWs developed in this project confine light with index guiding principles, they fall under the class of index guided LCWs. But the method with which waveguiding is achieved in these devices ensures higher indices at the liquid confining region, no matter how low the indices of the liquid are. This is similar to the freedom achieved by the latter type of LCWs. So the developed LCWs from nanoporous polymers are expected to take LCW based detection to an improved level. The state of art study for the index guided LCW approach is given in detail in the upcoming sections of this chapter. A brief explanation of the other approaches, especially interference based waveguides, is also given.

2.1 Index guided LCW

In a generic index guiding waveguide, a higher index core (n_c) is surrounded by low index cladding material (n_{cl}) as shown in Fig. 2.3. The spatial distribution of the electromagnetic field in these waveguides is explained in detail in Chapter 3. As water/aqueous solutions (n $\approx$ 1.33) form the core of LCWs used in biosensing, the major challenge is in finding a suitable solid cladding material with refractive index below 1.33. Most applied technologies in index guiding LCW either use materials of low refractive index as the cladding layer or make porosity in high index materials to reduce their refractive index [34]. The former use either fluorinated polymers such as Teflon AF (n$\approx$1.29) [35] or use another liquid with lower refractive index [36].

2.1.1 Teflon AF cladding based waveguides

The most straight forward and easy method of implementing a LCW is to use index guiding. A class of fluorinated polymers like Teflon AF are available which have lower refractive indices. Perfluorinated polymers like poly (tetrafluoroethylene) (PTFE), poly (tetrafluoro-ethylene-co-hexafluoro propylene) (FEP) and poly-(tetrafluoroethylene-co-perfluoro propyl vinyl ether) (PFA) have slighly higher indices than water, 1.35, 1.34 and 1.35

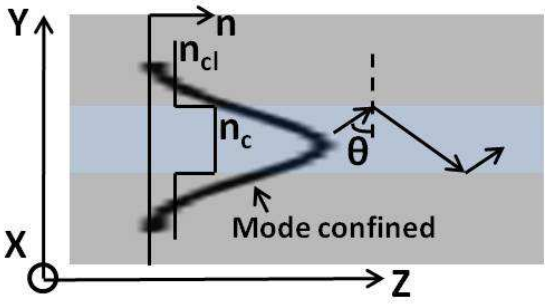

***Figure 2.3**: In index guided waveguides, the light confining region is of higher index (n_c) than the surrounding (cladding, n_{cl}) layers. In a ray representation, the ray propagates by reflection from the core-clad interface into the high index core medium. Light is confined mostly in the core, with basic TE mode confinement shown.*

respectively. So for aqueous or water core waveguides the most sought after fluorinated polymers are the amorphous copolymers of tetrafluoroethylene and 2,2-bistrifluoromethyl-4,5-difluoro-1,3-dioxole known as Teflon AF. There are two types of Teflon AF available, Teflon AF 1600 and 2400, with indices 1.31 and 1.29 respectively. In Teflon-based waveguides, the fluid supporting structures are substrates with higher indices, so index guiding is achieved by coating a thin layer of these teflon materials onto the substrates [37]. Pioneering works in the field mainly used capillary tubing based waveguiding. Guiding losses as low as 0.016 dB/cm is observed from glass LCW in glass tubing coated with Teflon AF 2400 [38, 39, 40]. The technology soon became adapted in planar device based guiding [41, 42]. Many recent works efficiently integrate LCWs using Teflon AF onto microfluidic systems [35]. Nowadays Teflon-based waveguides are widely used as sensors since the larger interaction length provided by these low loss guiding platforms enhance optical sensitivity [43, 44]. The commerical availability, low loss guiding make Teflon AF based waveguides a strong competing technology for the work developed in this project. However, in comparison our LCW scheme provides improved and tunable optical properties, compatibility with chemical functionalization and larger surface area for interaction. Fig. 2.4 shows an example of a Teflon AF coated PDMS microfluidic device.

Another interesting fluorinated polymer similar to Teflon AF is Cytop. It is an amorphous perfluoro polymer developed by *Asahi Glass Co.* [45] and has a refractive index slightly higher than water (n= 1.34). Agnarsson et al. shows some promising evanescent sensors using these Cytop polymers [32, 46]. Compared to Teflon AF these polymers are much more robust and compatible with chemical functionalization.

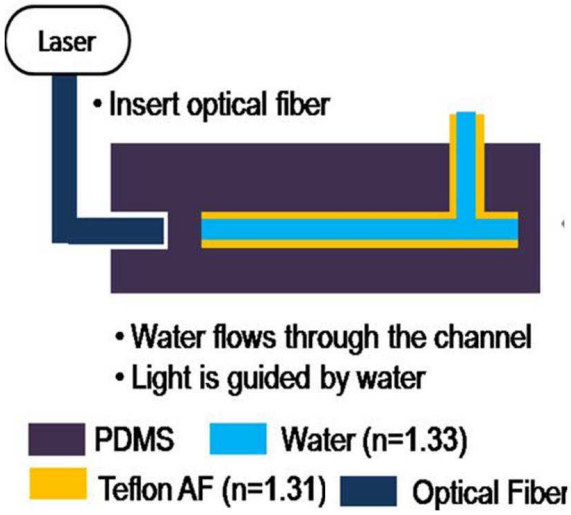

***Figure 2.4**: Teflon AF based index guided waveguide. Microchannels of 200 µm ×70 µm dimensions fabricated in PDMS are coated with 5-15 µm thick Teflon AF. A waveguide loss of 2.13 dB/cm at 488 nm is seen in these devices. Adapted from [35].*

2.1.2 Liquid-liquid waveguides

Instead of using a solid cladding, liquid-liquid (L^2) waveguides use an optically dense flowing fluid as a core within an enveloping sheath of lower index liquid. Pioneering works in this field were performed by Takiguchi et al. (Fig. 2.5a) [47] where sheath flow was used to construct an L^2 waveguide. Miscible and immiscible liquids can be used for this purpose. Such purely fluidic systems have several advantages over fluid-solid waveguides. The fluid profile in L^2 waveguides is independent of its supporting micro/optofluidic system. Thus a change in relative flow profile and flow rate of the liquid can be used to direct light in these waveguides [48, 49, 50]. In addition, the interface between two fluids can be made optically smooth by selecting the right combination of fluids (immiscible fluids). It is also possible to achieve small-featured waveguides by controlling and manipulating the fluid flow in L^2 waveguides. So compared to solid waveguides, these L^2 waveguides have a high level of reconfigurability for making tunable optical devices. Yet despite these advantages, L^2 waveguide technology is not widely used. They are susceptible to vibrations and diffusion effects which cause diffusion from the core into the cladding. Aside from the intermixing problem of core and cladding liquids, a major limitation in this technology is that light confinement is implemented primarily in one dimension. In other dimensions, cladding considerations persist. Recently Lim et al. [36] demonstrated a 3-D focused flow using 3-D hydrodynamic focusing (Fig. 2.5b). A propagation

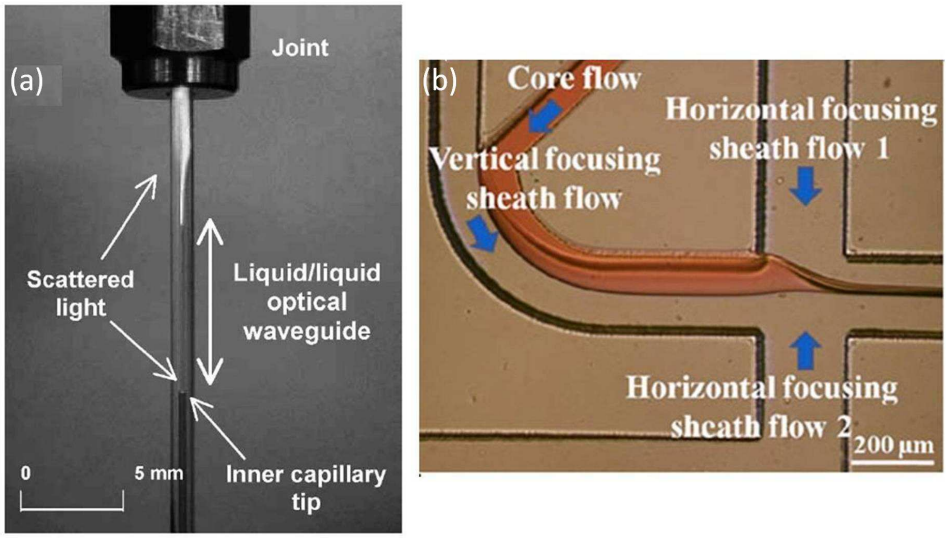

***Figure 2.5**: L^2 index guided waveguides (a) L^2 waveguides in a sheath flow capillary [47]; (b) 3-D focused flow using hydrodynamic focusing [36].*

loss of 0.55 dB/cm is observed in these devices. This might be a suitable way of solving cladding issues in the vertical plane. Still, fluid control elements can limit the functionality and implementation of these devices in real time sensing, and these are clear challenges to deploy these devices in field/in-vitro applications.

2.1.3 Nanoporous cladding waveguides

Another approach towards a low index cladding material is to use high index materials and render them porous. By making nanosized pores into the matrix of a high index solid material, the effective refractive index (n_{eff}, ref Chapter 3) of the system reduces. Many approaches are available in this field. Risk et al. uses a sacrificial porogen approach in which an organic macromolecule is selectively separated from a phase separated organic/inorganic polymer hybrid [51]. An alternative method for preparing nanoporous cladding is suggested by Korampally et al. where dielectric nanoparticles are deposited and porosity arises from the voids formed between these individual particles [34]. A NP clad system is quite advantageous as the cladding index can be tuned over a wide range via the choice of solid material and pore volume ratio. The materials offer high surface area that can be utilized to increase the density of binding probes to enhance detection sensitivity [52]. Fig. 2.6 shows some available NP cladded waveguides. So far only one dimensional confinement is shown in these devices. Also, the fabrication complexities compromise the performance of these waveg-

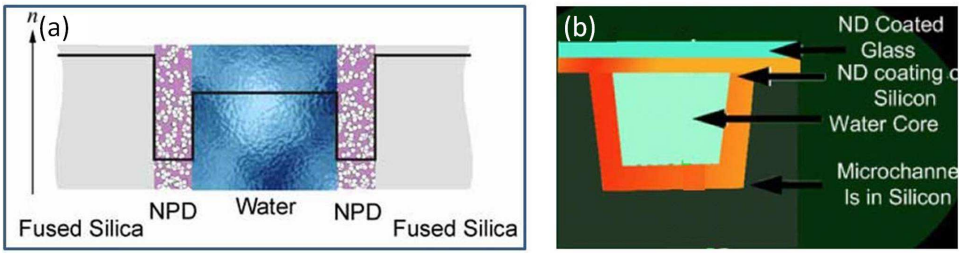

***Figure 2.6**: Nanoporous cladding index guided waveguides. (a) Cross sectional view of waveguides used in the works of Risk et al. [51]. Aqueous core and clad with low index nanoporous dielectric (NPD) film deposited on fused silica substrate; (b) from [34]. Microchannels etched in silicon and coated with nanoporous dielectric layer of low refractive index hold the aqueous solution.*

uides. The developed LCW in this project can be classified as a nanoporous cladding waveguide. As mentioned, fabrication of nanoporous materials can be a limiting complexity for these waveguides. However, the large surface area is a promising factor.

In summary, these are the main index guided waveguides used in LCWs. As mentioned earlier, index guiding is generally achieved in a high index region surrounded by low index region. As described in the next section, Almeida et al. shows that light can be confined strongly in a low index region even with index guiding principles [53] using so-called slot waveguides.

2.2 Slot waveguides

In high index contrast interfaces, Maxwell's equation states that for the normal component of electric flux density D to be continuous, the electric field, E, must undergo a high degree of discontinuity where its amplitude is highest in the low index region. In other words, to satisfy the boundary conditions (ref Chapter 3: Modes in planar waveguides) in a confined situation, at the high-low index interface, the electric field peaks within a very small distance (of the order of a few nm) and decays exponentially thereafter. In high index contrast situations, the field amplitude observed is significantly higher. The field in the low index region is greater than the high index region by a factor of $\frac{n_H^2}{n_s^2}$, where n_H is the index at the high index region and n_S is the index of the slot region (low index region), shown in Fig. 2.7. The main factor in confining fields within the low index region is that the width of the region should be lower than the penetration depth of the evanescent wave in the high index region. Almeida et al. shows that by embedding a nanometric scale low index slot between two high index slabs, the electric field can be confined in the low index region. Fig. 2.7a, b shows

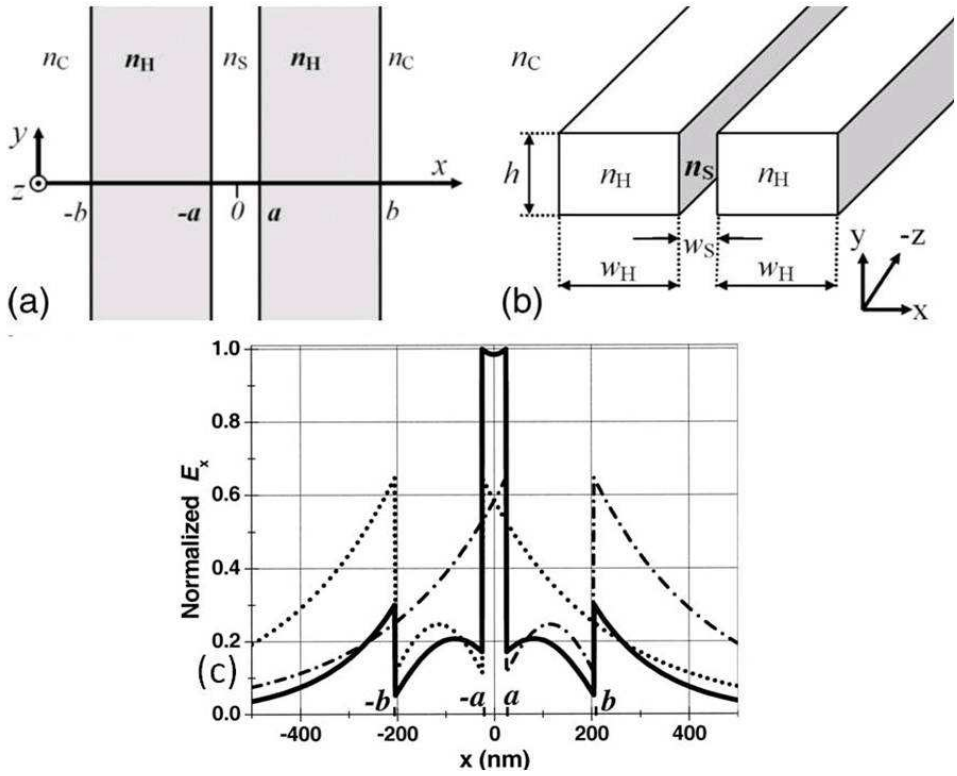

***Figure 2.7**: Slot waveguides. (a) Schematic of slot waveguides with infinite height; (b) with finite height; (c) normalized transverse electric field distribution of the fundamental TM eigenmode, (adapted from [53]), to illustrate discontinuity and high electric field confinement in the slot.*

a schematic representation of the slot waveguide structure with infinite and finite height. Fig. 2.7c shows how the normalized transverse electric field is distributed (fundamental TM mode). The dotted and dashed curves show the modes in the high index regions. Since the index contrast is an important requirement, SiO_2 based SOI (silicon on insulator) wafers (high index substrates) are normally used to make these slot waveguides. Ridges are etched down to the buried oxide layer using reactive ion etching (RIE) to make the nano sized slots. With chemical vapour deposition the top of the silicon can be coated making a sealed slot. Filling this slot with low index liquids gives liquid core based slot waveguides [54]. Slots with losses as low as 7 dB/cm has been made. Confinement of light in aqueous core is not as efficient as in air core slot waveguides as the index contrast reduces with liquid core. In addition, Si is used as the slot waveguide material, hence only infra red propagation is possible using these devices. Accordingly, slots are not very widely used as LCWs, instead, as light can be very strongly confined they are efficiently used as optical traps [55].

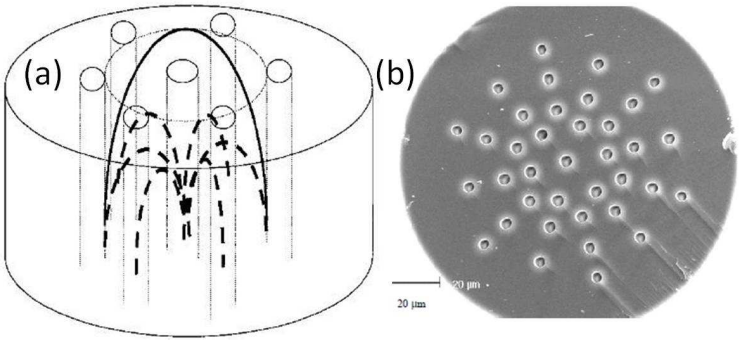

***Figure 2.8**: (a) Schematic representation of field superposition leading to a peak intensity in the hole at the centre (adapted from [57]); (b) water core Fresnel fiber [56].*

2.3 Fresnel waveguides

Like in slot waveguides, strong confinement of field at low index region can be attained by using Fresnel waveguides [56]. Fresnel waveguides have a distribution of holes incorporated into the solid clad which acts as a Fresnel zone to confine light. Through fresnel effects, the fibers guide light in the low index region, i.e. when the holes coincide with the Bessel distribution of the propagating optical field. Light scattered from the air silica interface constructively add to produce strong field at the centre [57, 58]. The central hole, when filled with liquid, forms liquid core Fresnel waveguides. Fig. 2.8 shows the field distribution in a fresnel fiber. The transmission losses observed in these water-core Fresnel fiber are of order ≈7dB/m. Compared to the LCWs developed in this project, a better light guiding is observed in these devices. However, most of the available Fresnel waveguides are in the near infra red wavelengths. In addition, these structures cannot be easily integrated onto a planar chip.

2.4 Interference based waveguides

Another approach to solve the low index cladding problem in LCWs is to apply a different guiding mechanism. In interference based waveguides, the liquid core is surrounded by high index solid clad material. The reflections from the solid-liquid interface are increased to confine light in the liquid core. The common principle behind these waveguides is to use interference to localize the electomagnetic field in the core. This is done by varying the refractive index profile of the cladding structures such that even with a low refractive index in the core, light remains confined in the core.

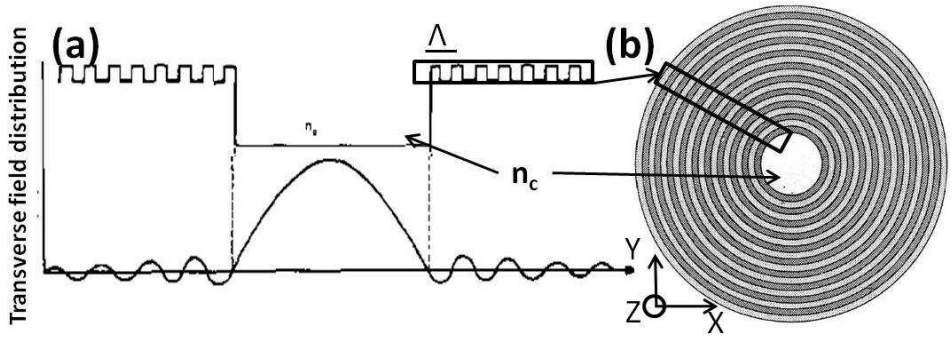

***Figure 2.9**: (a) Transverse field distribution of the fundamental modes in Bragg waveguides (adapted from [63]); (b) a Bragg fiber [62].*

Bragg fibers: Bragg fibers are an example of interference based waveguides. The principle is similar to that of Bragg reflections in X-ray analysis of crystalline materials. The periodic cladding layer is equivalent to a one-dimensional lattice. An electric field propagating in the periodic medium is expressed by a Bloch wave vector, **K**, which depends on the periodicity of the structures, Λ, wave frequency, ω and indices of the dielectric materials, given by

$$E_K(x,z) = E_K(x)e^{iKx}e^{i\beta z} \tag{2.2}$$

where E_K(x) is a periodic function with period Λ [59]. The real value of **K** corresponds to propagating Bloch waves, with the imaginary part relating to an evanescent regime corresponding to the forbidden bands (wavelength range that is forbidden from propagating through the structure) of the periodic medium. For liquid core Bragg waveguides, the Bragg lattice has to be highly reflective, i.e., **K** should be imaginary and the transverse component of the wave vector β should fulfull the same phase resonance condition as in the index guiding cases to propagate light along the z-axis. Fig. 2.9 shows the cross section of a Bragg fiber. A low index core is surrounded with periodic layers of high index materials forming Bragg layers [60, 61, 62]. When a low index core is used, these fibers usually provide efficient performance in infra red range. By increasing the core index, the transmission wavelength can be shifted to the visible range. However, with low index liquids like water, these waveguides are lossy below 600 nm. Furthermore, like in Fresnel waveguides, these structures cannot be easily integrated onto planar chips. To mention, Bragg fibers are known as one-dimensional photonic crystals.

Photonic crystal waveguides: Photonic crystals are materials with high and low dielectric constants peridically structured on a length scale of order half wavelength. Only certain modes or wavelengths of light are allowed to propagate in these structures, resulting in photonic band gaps or disallowed

bands. Like in semiconductors, intentionally introduced defects can localize field. In hollow core photonic crystal fibers (HC-PCFs) the working principle is similar to photonic crystals. In Fig. 2.10a, a hollow core is surrounded with a periodic arrangement of holes inside a silica network [64, 65]. If the core can support one of the modes in the band gap, light can be confined in the low index region without much loss. Loss as low as 1.2 dB/km is observed in HC-PCFs with air core. Sensing is obtained in these devices, either by filling the core with liquid or filling the holes in the clad region with liquid [66]. PCF sensors based on surface Raman scattering are the recent advancements in this field [67]. 2D photonic crystal waveguides uses similar photonic bandgap structures as shown in Fig. 2.10b. Photonic crystal defects exploit the band gap mechanism to confine light. A line defect forms a waveguide. Low index guiding is achieved by increasing the radius of holes in one row, thus introducing a line defect [68, 69, 70, 71]. Though these devices offer strong light confinement, operating wavelengths in these devices have to predetermined and is not widely tunable.

ARROW: Antiresonant reflecting optical waveguides (ARROWs) are a type of interference based LCWs which do not require periodicity as in photonic crystals. A single dielectric layer is sufficient in these interference based guiding devices. ARROW has two alternating cladding materials. The light from the low index core (n_c) is refracted into the ARROW high index layers (n_{cl1}, n_{cl2}). When the thickness of layers are such that the round trip phase shift Φ_{RT} for the transverse wave component in the medium is $m\pi$ (m odd), a low loss light propagation in the low index region can be achieved [72]. The loss (TE mode) in these waveguides can be expressed as a function of core thickness and cladding layers N as ([19]),

$$\alpha = \frac{\lambda^2}{n_c d^3 \sqrt{n_{cl1}^2 - n_c^2}} \sqrt{\frac{n_{cl2}^2 - n_c^2}{n_{cl1}^2 - n_c^2}}^N \tag{2.3}$$

where n_{cl1} and n_{cl2} are the indices of the two cladding materials (shown in Fig. 2.11a). Solid state ARROWs use silicon dioxide on top of a silicon substrate [74] as ARROW cladding materials. Duguay et al. shows waveguiding in silicon dioxide (SiO_2) as the core layer. One side of the core is subjected to total internal reflection while the other side is highly reflective from the antiresonant character of the lower layers in the structure (Fig. 2.11b). Losses as low as 0.4 dB/cm is shown for TE modes.

The first hollow core ARROW implementations were demonstrated by Delonge and Fouckhardt [75]. With improved fabrication techniques the losses in these hollow core devices were reduced [76]. Waveguides with loss as low as 1.13 dB/cm have been developed [77, 78]. Silicon nitride and silicon

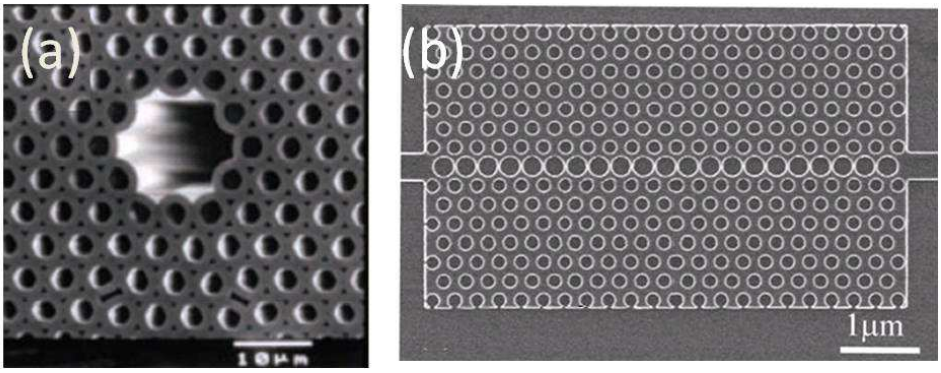

***Figure 2.10**: Photonic crystal based (a) fibers [64] (b) waveguides [73]).*

dioxide based ARROWs with liquid cores is recent advancements in this field [79]. Combined liquid core/liquid clad ARROWs have been developed that reduce optical losses in 2D-ARROWs and also allow L^2 guiding in low index fluids [80]. These platforms are used for many applications like optical trapping [81] and single molecule detection. Fig. 2.11 shows ARROW hollow core waveguide designs. Fig. 2.11c is fabricated on a planar substrate while the Fig. 2.11d is on a pre-etched substrate [76]. Like the nanoporous devices developed in this project, complexities in device fabrication can be a limiting factor for these devices.

These are some of the different LCW technologies currently available. Nowadays, liquid core based waveguiding are industrially adopted. Liquid core fibers offer good performance in UV and visible wavelengths, that can be used for applications like dental curing, fluorescent detection etc. Companies like *efibertools* [82] and *LUMATEC* [83] offer liquid core waveguides deep into the UV region commercially.

To conclude the chapter, we have provided information regarding the works in the field of liquid core waveguiding. Though different waveguiding principles and types of LCWs are available, the sensing specificity and other requirements mainly decide the choice of the LCW in an application. The chapter mainly discusses liquid core waveguides that solve the problem of low index cladding material. These are index guided waveguides. In some other LCWs using multiple reflections or interference, light is guided in a low index material surrounded by high index material. Even though interference or multiple reflection based waveguides strongly confine light and offer high performance, index based guidance have a leverage in waveguiding as they allow wide range of operating wavelengths [84]. This Ph.D project offers an alternative LCW technology. Although the developed system in this project uses index guiding principles, our waveguiding platform is not limited by the restrictions of finding suitable cladding materials.

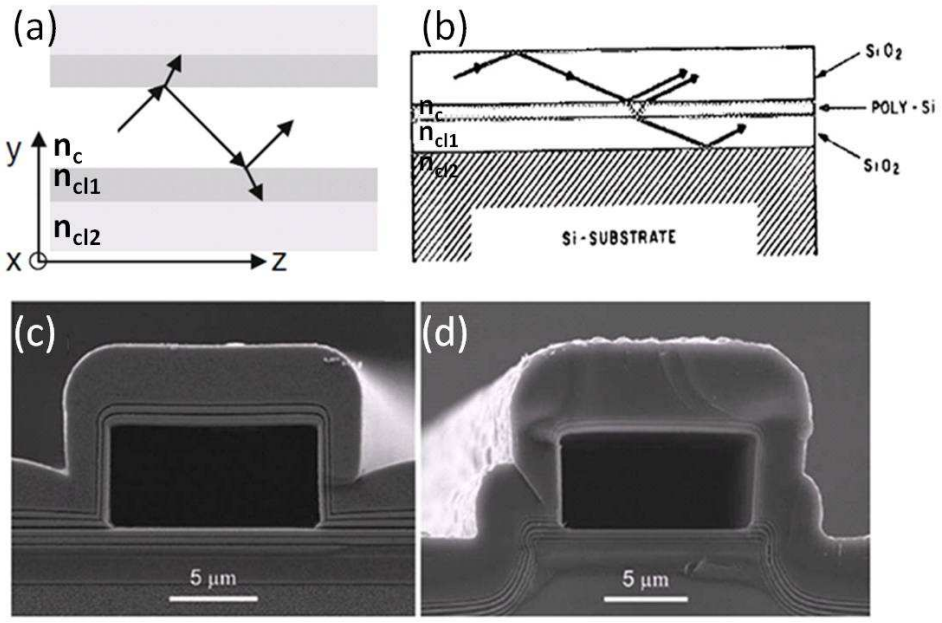

***Figure 2.11**: (a) Schematic representation of ARROW waveguides [19]; (b) Waveguiding in SiO_2 using antiresonant reflection on silicon wafer [74]. ARROW hollow waveguide design. Scanning electron microscope images (adapted from [76]); (b) ARROW hollow waveguide on a planar substrate; (c) hollow core ARROW on a pre etched substrate. SiO_2 and SiN are the used ARROW cladding materials.*

Chapter 3

Theoretical background

This chapter gives the theoretical background needed to understand the presented work. The chapter is introduced with basic properties of dielectric waveguides. Total internal reflection (TIR) and mode confinement in optical waveguides are explained briefly, in a similar approach to [20]. We characterize our waveguides in this work by their transmission, for which this chapter defines the most important concepts and characterization parameters. In the effective refractive index section, Section 3.2, the approach used to determine the effective index of the infiltrated polymer matrix is derived. A brief description of Lambert-Beer law is provided as it pertains to the determination of analyte concentrations. Surface effects like contact angle and surface tension is also mentioned in this chapter.

3.1 Fundamental properties of optical waveguides

An optical waveguide is a dielectric structure that propagates light of wavelengths lying in the infrared (IR), visible and UV range of the electromagnetic spectrum. The propagation of light in a dielectic structure can be visualized using TIR.

3.1.1 Total Internal reflection

Light incident on the interface of two mediums of different refractive index is reflected and transmitted according to Snell's law.

$$\sin\theta_2 = \frac{n_c}{n_{cl}} \sin\theta_1, \tag{3.1}$$

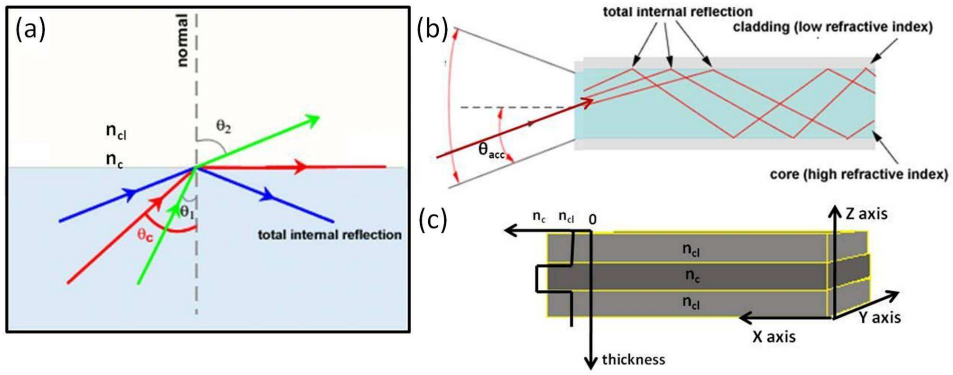

***Figure 3.1**: Conceptual illustration of total internal reflection. (a) TIR is observed when incident light hits the medium interface at an angle larger than critical angle; (b) TIR observed in a an optical waveguide as the core refractive index is higher than the cladding; (c) diagram of basic three layer planar waveguide structure, with refractive index profile.*

where $n_c > n_{cl}$. When $\theta_2 = 90^0$, θ_1, angle of incidence is called the critical angle. TIR is observed at the boundary of two dielectic mediums when a ray of light hits the boundary at an angle larger than the critical angle (angle of incidence), shown in Fig. 3.1a. Thus in an optical waveguide where the dielectric structure that transports energy is of higher refractive index than the surrounding medium, TIR is observed as light enters the dielectric within a certain angle, known as the acceptance angle (θ_{acc}) (Fig. 3.1b). For an optical waveguide with step refractive index profile, the acceptance angle is determined from indices of refraction of dielectric medias as:

$$NA = n \sin \theta_{acc} = \sqrt{n_c^2 - n_{cl}^2}, \tag{3.2}$$

were NA is the numerical aperture of the waveguide (Fig. 3.1c).

To fully describe the modal behaviour of waveguiding systems Maxwell's wave equation is used. The description is adapted from Optical Waveguide Modes, Integrated Optics by Hunsperger [20].

3.1.2 Modes in planar waveguides

In a basic three layered dielectric structure were the middle core layer has higher index n_c than the neigbouring top and bottom cladding layers (n_{cltop}, n_{clbot}), as shown in Fig. 3.2, confinement of light can be described using Maxwells wave equation. The layers are assumed to extend to infinity in x and y directions, and the cladding layers are also assumed to extend to infinity for both top and bottom layers. The electromagenetic wave equation

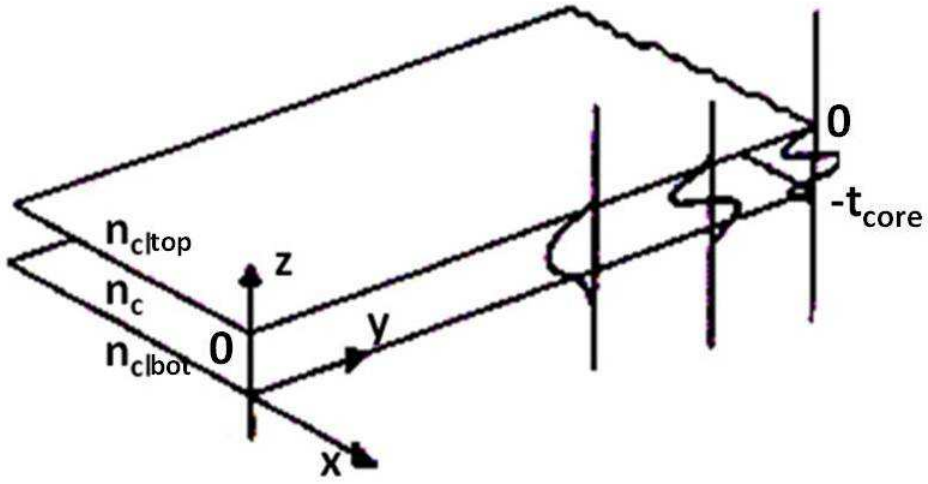

Figure 3.2: *A three layered planar waveguide. Distribution of the electric field for the first three modes are also shown. Adapted from [20].*

is a second order partial differential equation that describes propagation of electromagnetic wave through a medium. Expressed in terms of the electric field, E, the wave equation is

$$(\nabla^2 - \frac{n^2}{c^2}\frac{\partial^2}{\partial t^2})\vec{E}(\vec{r},t) = 0, \tag{3.3}$$

where n is the index of refraction and c is speed of light in vacuum. For monochromatic waves, the solution to the wave equation is,

$$\vec{E}(\vec{r},t) = \vec{E}(\vec{r})e^{i\omega t} \tag{3.4}$$

where $\omega = 2\pi f$ is the angular frequency of the wave, r is the position vector. Thus for a TE-polarized plane wave travelling in y direction, E_y=0 and other field components E_x, H_z and H_y are non zero. Thus

$$\vec{E}(\vec{r}) = E(x,z)exp(-i\beta y) \tag{3.5}$$

where β is propagation constant. Substituting Eq. (3.4) in Eq. (3.3), gives

$$\partial^2 E(z,x)/\partial z^2 + \partial^2 E(z,x)/\partial x^2 + \left[k^2 n^2(\vec{r}) - \beta^2\right] E(z,x) = 0. \tag{3.6}$$

When the dimensions are assumed to be infinite in the x direction, there is no dependence on the x direction so the equation becomes

$$\partial^2 E(z)/\partial z^2 + \left[k^2 n^2(\vec{r}) - \beta^2\right] E(z) = 0. \tag{3.7}$$

In the dielectric structure, t_{core} stands for thickness of the core region. Regions of different refractive index can be divided based on their thickness;

region 1 of $n = n_{clbot}$, lies in $-\infty < z \leq -t_{core}$, region 2 of $n = n_c$ lies in $-t_{core} \leq z \leq 0$ and region 3 of $n = n_{cltop}$ lies in $0 \leq z < \infty$. With different indices in each region, Eq. (3.7) can be expressed with corresponding indices. According to boundary conditions in the z direction, E(z) and its differential should be continuous at the interfaces so only certain solutions are possible in Eq. (3.7); either sinusoidal or exponential functions of z. For conditions where $n_c > n_{cltop}$ and $n_c > n_{clbot}$, only certain feasible solutions that satisty the boundary conditions exists. These feasible solutions are called modes. In other words, mode is a spatial distribution of optical energy in one or more dimensions. Thus the transverse component of the electric field in each region can be expressed as

$$E(z) = \begin{cases} C(\exp[-q(z)]) & \infty > z \geq 0 \\ C(\cos(hz) - \frac{q}{h}\sin(hz)) & 0 \geq z \geq -t_{core} \\ C\left[\cos(ht_{core}) + \frac{q}{h}\sin(ht_{core})\right]\exp(p(t_{core}+z)) & -t_{core} \geq z \geq -\infty \end{cases} \tag{3.8}$$

where C is a normalization constant and q, h and p are defined as

$$\begin{aligned} q &= \sqrt{\beta^2 - n_{cltop}^2 k^2} \\ h &= \sqrt{n_c^2 k^2 - \beta^2} \\ p &= \sqrt{\beta^2 - n_{clbot}^2 k^2} \end{aligned} \tag{3.9}$$

where k is the wave number and c is the speed of light in vacuum. The constants are solved by using the boundary conditions at the parallel planar boundaries at z=0 and z=-t_{core} where E(z) and its differential should be continuos. β has only discreet values and fulfills the equation

$$\tan(ht_{core}) = \frac{p+q}{h(1-\frac{qp}{h^2})}. \tag{3.10}$$

So each discreet value of β corresponds to a solution of Eq. (3.3) of the form Eq. (3.8), which are the modes in these waveguides. If only one mode is available it is called a single mode waveguide. Eq. (3.10) can be solved numerically and the values provide the refractive indices of the modes, determined by

$$\tilde{n_m} = \frac{\beta_m}{k} = \frac{c}{w}\beta_m = \frac{\lambda}{2\pi}\beta_m \tag{3.11}$$

where λ is the free space wavelength of light. The mode index defines the confinement of the electric field within the waveguide core as $\tilde{n} \longrightarrow n_c$ for $t_{core} \longrightarrow \infty$. For single mode waveguide structures in the LiCorT project, t_{core} should be less than 470 nm (n_{cl}=1.26 and n_c=1.43), which is difficult to fabricate using current photolithography techiniques due to diffraction limit. Fig. 3.3 shows the field confinement in a single mode structure. The waveguide structures applied in our scheme are of the order 500-100 μm in core thickness [22, 21, 20].

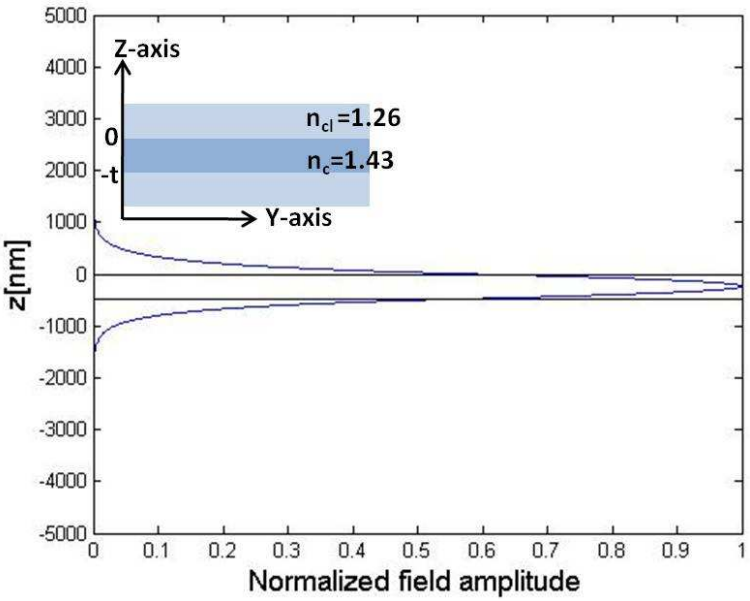

***Figure 3.3**: Field distribution according to Eq. (3.8) for a core thickness of 465nm, overlayed with the waveguide structure. A symmetrical index profile is assumed.*

3.1.3 Attenuation in waveguides

Attenuation is the loss of intensity/power of light through a medium. This can be caused by absorption, scattering or radiation losses. Volume and surface scattering contributes to the types of scattering losses in an optical waveguide. As volume scattering strongly depends on the volume imperfection (like cracks, foreign particles, pores) and the relative size compared to the wavelength of light in the material, this can be assumed to be very negligible in most waveguides. Surface scattering effects are prominent in waveguides with higher order modes as they interact more strongly with the surfaces of the waveguide.

If we define *P(y)* as the field power at a point y in the waveguide, the power attenuation coeffient, $\alpha(y)$, is defined as

$$\alpha(y) = -\frac{1}{P(y)}\frac{dP(y)}{dy}. \tag{3.12}$$

Hence $\alpha(y)$ is the rate of power loss per unit length of the medium. The attenuation is usually measured in decibels (dB). The decibel is a ratio of two power levels: in optical waveguides, it is the ratio of output optical power from the waveguide to the input power. To account for a large range of variations, logarithmic representation is typically chosen. Thus the attenuation in dB (L) for an optical waveguide with input optical power P_{in}

and output optical power P_{out} is defined as

$$L = 10 \log_{10} \left(\frac{P_{in}}{P_{out}} \right). \tag{3.13}$$

Four types of attenuation or losses may occur in an optical coupling setup containing a rectangular waveguide with bends: coupling loss, transition loss, propagation loss and radiation loss [85].

Coupling loss: When light propagates from one medium to another with different refractive index, light is reflected back and subject to losses. Coupling losses are also observed when light is coupled from an optical fiber to an optical waveguide. This corresponds to facet roughness and the mismatch of modes propagating in the optical fiber and the optical waveguide. Fresnel reflection loss at the interface between two different refractive index media mainly contributes to the coupling loss. When light is coupled from an optical fiber to a waveguide, the presence of an air gap between the two guides can increase the reflection loss. The ratio of light reflected back is given by

$$R = \left(\frac{n_1 - n_0}{n_1 + n_0} \right)^2 \tag{3.14}$$

where n_1 is the refractive index of the fiber core and n_0 is the refractive index of the medium between the optical fiber and waveguide. Fresnel reflection also occurs at the waveguide output. Another main source of extrinsic coupling loss is due to poor fiber to waveguide alignment (longitudinal, lateral and angular misalignment) (Fig. 3.4).

Transition loss: An optical waveguide can have different straight and curved regions. Losses due to modal mismatch and the transition between modes as they propagate form one type of waveguide region to another is defined as transition loss.

Propagation loss: Propagation loss is defined to be loss occuring when light propagates for a certain length in a medium. Cutback is a destructive technique used to determine the propagation loss in a waveguide. Measurements are carried out by obtaining the power at the output of a waveguide of certain length. The waveguide is then cut and measurements are repeated, keeping the coupling efficiency of light consistent with previous measurements. Subtracting the results from the shorter length gives the propagation loss in the residual length of the waveguide. An alternative to the cutback technique is the substitution method, where instead of cutting, measurements are repeated in a shorter waveguide with the same characteristics. The

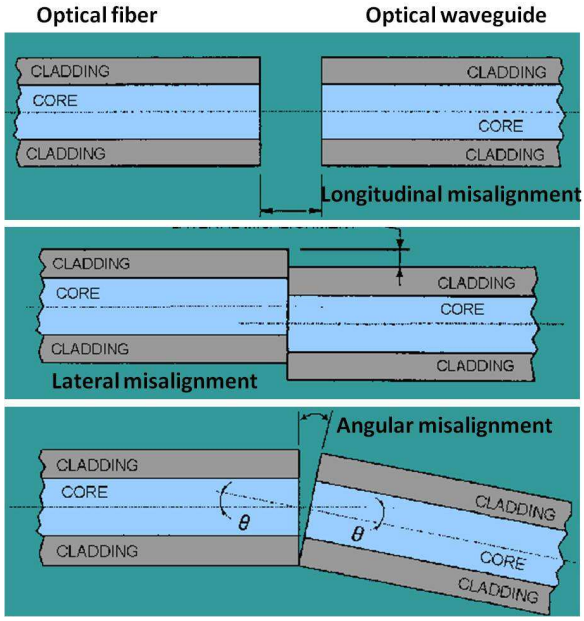

***Figure 3.4**: Sources of coupling loss when light gets guided from one waveguide (optical fiber) to another (optofluidic waveguides).*

substitution method is used to measure propagation losses in this project. As propagation loss is determined by the length of the waveguide, linearly fitting loss in dB as a function of propagation length gives the propagation loss per unit length of the waveguide (Fig. 5.7) [86, 69, 68, 78]. Propagation loss corresponds to the absorption and scattering loss in a waveguide.

Radiation loss: Radiation loss or bending loss is due to distortions of the optical field when guided waves travel through a bend in the waveguide. The loss depends on how well confined light is within the core of a waveguide. Bend loss in a waveguide is determined by the core-cladding index difference, core radius, bend radius and the wavelength of light. Optical guides with larger NA have larger core clad index difference, thereby confining light tighter in the core; hence these waveguides suffer lower bend losses. In a bend waveguide, light is lost from the outer surface of the bend, thus some bend radius criterias must be satisfied to achieve efficient light propagation. We adopt the velocity approach developed by Marcatili and Miller. Consider a cicular bend section as shown in Fig. 3.6. n_2 and n_1 corresponds to the core and cladding refractive index respectively. There is certain radius $(R + X_r)$ beyond which the evanescent field cannot travel fast enough to keep with the rest of the mode. Thus an optical mode propagating in the cirular bend of radius R, with a porpagation constant β_z in the waveguide and β_0 in

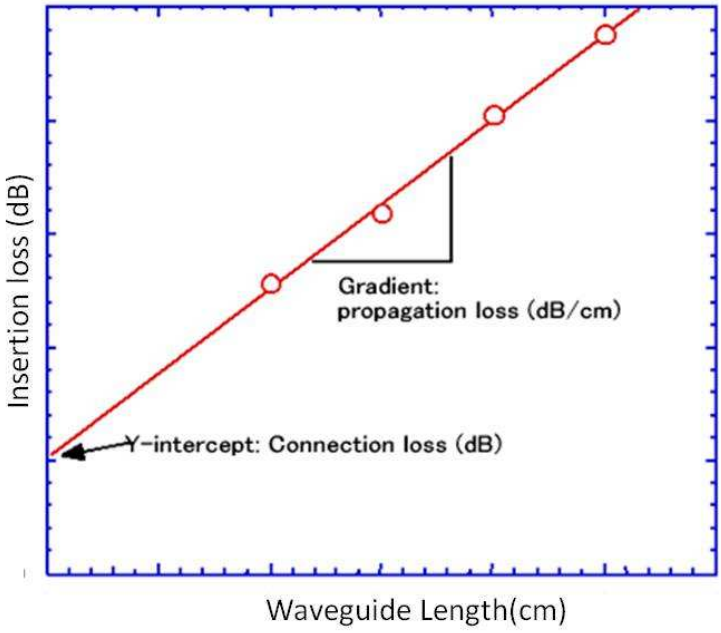

***Figure 3.5**: Propagation loss measurements using the substitution techniques.*

vacuum gives X_r

$$X_r = \frac{\beta_z - \beta_0}{\beta_0} R \tag{3.15}$$

While designing a bend, care is to be taken such that the evanescent field should not exceed the value X_r [20].

3.2 Effective index of nanoporous materials

(The derivations are based on [87, 23, 88, 89])

In presence of an electric field, a local electric dipole moment is induced in dielectric materials. The displacement field D is defined in CGS units as

$$D = \epsilon E = (1 + 4\pi\chi) E = E + 4\pi P \tag{3.16}$$

where E is the electric field applied, $\epsilon(=n^2$, refractive index of the medium) is the dielectric constant of the medium relative to vaccuum, χ is the dielectric susceptibility which describes how easily a dielectric medium polarizes in response to an electric field and P is polarization defined as the dipole moment per unit volume. Thus if we consider the propagation of a wave in a homogeneous isotropic non magnetic medium, the effective field experienced by the j^{th} dipole in the medium, i.e., the local field at the dipole, can be

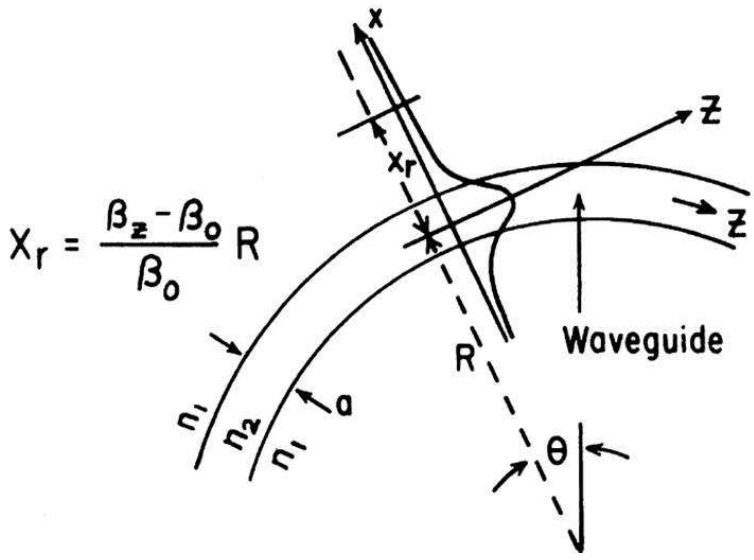

***Figure 3.6**: Diagramatic illustration of the velocity approach determining the radiation loss in a bend waveguide [20].*

expressed as the sum of the incident field (E) and contributions from all the other dipoles. Fig. 3.7 shows the field in a medium. A simple cubic lattice of polarizability points is used to assist the derivation.

$$E_{loc} = E + \frac{4\pi}{3}P \tag{3.17}$$

If the polarizability of each point in the medium is given by α, the dipole moment corresponds to

$$p = \alpha E_{loc} \tag{3.18}$$

thus the dipole per unit volume within the imaginary cavity as shown in Fig. 3.7 is

$$P = \frac{1}{V}\sum_i p_i \tag{3.19}$$

where V is the volume of the system. Thus from Eq. (3.18),

$$P = np = n\alpha E_{loc} \tag{3.20}$$

where n is number of points (dipoles) per unit volume. Thus replacing P in Eq. (3.17) and Eq. (3.16)

$$\begin{array}{l} \epsilon E = E + 4\pi n\alpha E_{loc} \\ E_{loc} = E + \frac{4\pi}{3} n\alpha E_{loc}. \end{array} \tag{3.21}$$

Representing E_{loc} in terms of E, gives

$$\begin{array}{ll} \frac{\epsilon-1}{\epsilon+2} = \frac{4\pi}{3} n\alpha & (CGS) \\ \frac{\epsilon-1}{\epsilon+2} = \frac{1}{\epsilon_0} n\alpha & (SI), \end{array} \tag{3.22}$$

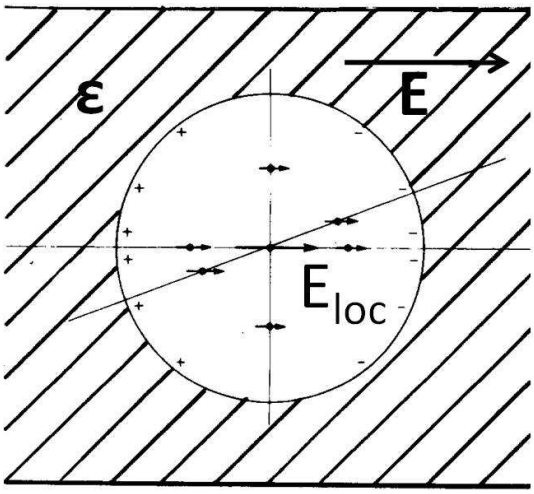

***Figure 3.7**: A dielectric medium subjected to electric field E. An effective field at one of the dipoles is expressed as E_{loc}, which is the field at the centre of the imaginary cavity.*

which can be expressed in refractive index, n as:

$$\frac{n^2-1}{n^2+2} = \frac{1}{\epsilon_0} n\alpha \quad (SI). \tag{3.23}$$

This is referred to as the Lorentz-Lorenz relation.

The dielectric constant at optical frequencies arises from electronic polarizability. In a heterogeneous medium, with two components, polarization contribution from the whole system can be expressed as (in CGS)

$$P = (n_a\alpha_a + n_b\alpha_b)E_{loc}. \tag{3.24}$$

Thus Eq. (3.22) can be expressed in terms of an effective dielectric constant ϵ_{eff}

$$\frac{\epsilon_{eff}-1}{\epsilon_{eff}+2} = \frac{4\pi}{3}(n_a\alpha_a + n_b\alpha_b). \tag{3.25}$$

When represented in terms of volume fraction of the phases where f_i is the volume fraction of the i^{th} phase: $f_i = \frac{n_i}{\sum_j n_j}$

$$\frac{\epsilon_{eff}-1}{\epsilon_{eff}+2} = f_a\frac{\epsilon_a-1}{\epsilon_a+2} + f_b\frac{\epsilon_b-1}{\epsilon_b+2}. \tag{3.26}$$

Thus when $\sum_i f_i$=1, f_a=1-f_b, substituting in Eq. (3.26) becomes

$$\frac{n_{eff}^2-1}{n_{eff}^2+2} = f_a\frac{n_a^2-1}{n_a^2+2} + f_b\frac{n_b^2-1}{n_b^2+2} \tag{3.27}$$

$$\frac{n_{eff}^2-1}{n_{eff}^2+2}-\frac{n_a^2-1}{n_a^2+2}=f_b\left[\left(\frac{n_b^2-1}{n_b^2+2}\right)-\left(\frac{n_a^2-1}{n_a^2+2}\right)\right] \tag{3.28}$$

$$\frac{3n_{eff}^2-3n_a^2}{\left(n_{eff}^2+2\right)\left(n_a^2+2\right)}=f_b\left[\frac{3n_b^2-3n_a^2}{\left(n_b^2+2\right)\left(n_a^2+2\right)}\right] \tag{3.29}$$

$$\frac{n_{eff}^2-n_a^2}{n_{eff}^2+2}=f_b\left(\frac{n_b^2-n_a^2}{n_b^2+2}\right). \tag{3.30}$$

The equation is the Lorentz-Lorenz effective medium expression. Thus effective index of a nanoporous material with two components 1 (majority component) and 2 (minority component) is given as

$$\frac{n_{eff}^2-n_1^2}{n_{eff}^2+2}=V_2\left(\frac{n_2^2-n_1^2}{n_2^2+2}\right) \tag{3.31}$$

where n_1 and n_2 are the refractive indices of the majority and the minority component respectively, and V_2 is the volume fraction of the minority component.

3.3 The Lambert-Beer Law

Transmittance (T) of a solution is the amount of light allowed through it. This is expressed as the ratio of intensity of light transmitted, I_t, to the incident light intensity, I_0:

$$T=\frac{I_t}{I_0}. \tag{3.32}$$

Thus absorbance of a medium/solution can be expressed in terms of its transmittance as:

$$A=\log(\frac{1}{T}). \tag{3.33}$$

The absorption of light can be attributed to the properties of the medium or solution through which light is transmitted. Lamberts Beer law relates the transmittance of light through a medium to be logarithmically dependent on the absorption coefficient, α, of the solution and distance, d, travelled by light within the medium/solution. Thus

$$T=10^{-\alpha d} \tag{3.34}$$

where α is dependent on the molar absorptivity (how strongly the medium absorbs) of the absorber, ϵ, and the concentration of absorbing species, C:

$$T=10^{-\epsilon dC} \tag{3.35}$$

Thus substituting T in Eq. (3.35) with Eq. (6.2)

$$A = \epsilon C d. \tag{3.36}$$

The Lambert Beer law is valid only for dilute solutions. As a thumb rule, materials showing absorbance up to 0.5-0.6 obeys Lambert Beer law, beyond these values the law does not hold. The law is applied to analyze the concentration of the absorber species in a solution. The absorption spectrum of the absorber is noted, in particular the peak absorbing wavelength. At a constant propagation length, the absorbance of this wavelength is linearly dependent on the concentration of the absorber. Thus with a known relation, an unknown concentration of the absorber can be determined. Absorption spectroscopy uses the same principle to determine the concentration of the absorbers in a solution [90].

The above sections present the relevant theoretical background to understand the optical techniques applied in this PhD thesis. For understanding the fluidics, some of the important theories are mentioned below.

3.4 Surface effects

Due to large surface to volume ratio, surface effects are predominant in microfluidic and nanofluidic devices. Of these, capillary effects seen at the interface between a liquid and another material: gas, solid or liquid, are very consequential. At the interface of two materials, surface tension is observed as molecules at the surface have more energy than in the bulk.

Surface tension: The surface tension of an interface is defined as the Gibbs free energy (G) per area for fixed pressure and temperature ([91]). Parameters like pressure, p, temperature, T, and particle number N controls Gibbs free energy of a system, which is minimum at equillibrium or quasi equillibrium states. Thus δG=0 at equillibrium. To form an interface it costs energy,

$$Energy = \gamma A \tag{3.37}$$

where γ is the surface tension (in Jm^{-2}) and A is the area of the surface [91]. It can also be expressed as force per unit length (Nm^{-1}). Since surface exerts forces (to reduce the surface and thus to reduce the interface and attain equillibrium), liquids are compelled to form shapes (spheres or curved surfaces) on surfaces. Across a curved surface at equillibrium, non-zero surface tension results in Young Laplace pressure drop, $\Delta \mathrm{p}_{surf}$, i.e. the pressure is highest at the medium where centres of the curvature are placed.

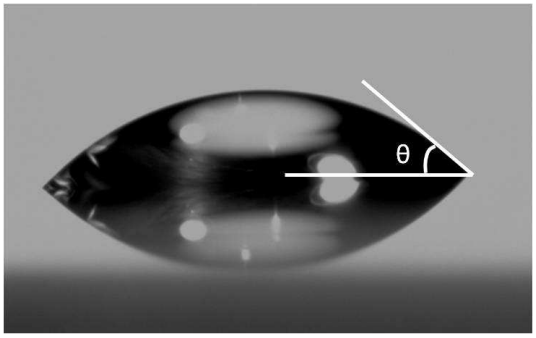

***Figure 3.8**: The contact angle θ is angle between solid/liquid and liquid/gas interface at the contact line.*

Another important surface effect occurs at the contact between three different phases: contact angle. This can be used to understand the capillary forces acting on the surface.

Contact angle: It is defined as the angle between the solid/liquid and liquid/gas interfaces at the contact line where three immiscible phases meet as shown in Fig. 3.8. In equillibrium, contact angle (CA) can be expressed in terms of surface tension as,

$$\cos\theta = \frac{\gamma_{sg} - \gamma_{sl}}{\gamma_{lg}} \tag{3.38}$$

where γ_{sg}, γ_{sl} and γ_{lg} are surface tensions of solid/gas, solid/liquid and liquid/gas interfaces respectively. The above equation is known as Young's equation. Surfaces with contact angle $\theta < 90°$ are surface wettable and hydrophillic, while those above 90° are hydrophobic in nature [91]. Molecules that have affinity to surfaces are called surfactants. These change surface tension of a surface. By using surfactants, a non wetting surface can be made surface wettable.

Capillary filling: Capillary filling or action is the ability of a liquid to flow against gravity. Surface tension and adhesion forces between the liquid and the medium leads to this effect. Poiseuille flow is observed when liquid is driven across a channel by introducing pressure differences at the ends of the channel. In the polymers used in this thesis, a similar flow pattern is assumed, where the viscous drag implies the flow [92, 93]. For perceiving the flow of liquids in such extreme spatial confinements, a better understanding of fluid parameters like viscosity η or surface tention γ is required. For a capillary/microchannels with circular cross section, r (radius), if its dimensions are so small that the total external pressure is low compared to

viscous drag, the flow rate Q can be expressed according to Hagen-Posieuille relation as [94, 91],

$$Q = \frac{\pi r^4}{8\eta L}\Delta p_{surf} \tag{3.39}$$

where Δp_{surf} is the Young Laplace pressure drop and L is the length/position of the liquid flow in the propagation direction. The pressure drop can be expressed in terms of surface tension as,

$$\Delta p_{surf} = \frac{2\gamma}{r}\cos\theta \tag{3.40}$$

where θ is the contact angle for channel-liquid-air system. The rate of penetration of fluids for time, t, $\frac{dL(t)}{dt}$ over a distance in this system can be yielded from mass conservation of the flow in the channel, for Poiseuille flow, at postion = L(t),

$$\frac{dL(t)}{dt} = \frac{r^2\Delta p_{surf}}{8\eta L}. \tag{3.41}$$

The differential equations can be solved as,

$$L(t) = \sqrt{\frac{r\gamma\cos\theta}{2\eta}t}. \tag{3.42}$$

For porous systems, the penetration of liquid into pores can be equivalent to the penetration of n different capillaries, thus the volume flow rate in porous systems can be expressed as [92],

$$\frac{dV(t)}{dt} \ \alpha \ \frac{\Delta p_{surf}}{\eta L(t)} \tag{3.43}$$

thus the mass flow rate becomes,

$$\frac{dm(t)}{dt} \ \alpha \ \frac{\rho\Delta p_{surf}}{\eta L(t)} \tag{3.44}$$

where ρ is the mass density of the fluid. Hence the mass uptake (volume uptake) in a porous system can be expressed by Lucas-Washburn relation [92] as,

$$m(t) \ \alpha \ \left[\rho\sqrt{\frac{\gamma}{\eta}\cos\theta}\sqrt{t}\right] \tag{3.45}$$

where m(t) depends on $\sqrt{t}$ and square root of its fluid parameters, γ, η, and θ [95].

Subsequently, to fill a 1 cm long capillary of nanometer scale radius (comparable to that of the nanopores in the system studied), the time required

can be assessed from Eq. (3.42). The nanoporous polymer developed is assumed to have a similar surface tension as its homopolymer. This is due to the fact that, even though the etched out polydimethyl siloxane may leave some residue, they do not cover the entire pore surface. To calculate the penetration time, we consider the liquid (water) surface tension of Poly (1,2-butadiene), γ, which is 30.35 $\times 10^{-3} \frac{N}{m}$. The viscosity of water at a temperature of 25°, η is $8.9 \times 10^{-4} \frac{Ns}{m^2}$ [96, 97, 98]. Therefore the time taken to fill a centimeter long cylindrical nanopore of radius 7±3 nm with contact angle 40±10° (the assumed values are comparable with the nanoporous system addressed in this work) can be obtained from,

$$t = \frac{2L^2\eta}{r\gamma\cos\theta} \tag{3.46}$$

yielding a time of 11-38 min to fill cylindrical pores of radii 7±3 nm. A material with lower contact angle (high surface wettability) and larger pore size is filled faster. As the pore size reduces, the hydraulic resistance increases since it is proportional to r^{-4}. As such, a lower cylindrical pore size corresponds to a longer penetration time.

The theory provided gives a generalised picture on capillary filling in a nano-sized channel. We observe that the devices used in this study fill more quickly than the values calculated. This may be attributed to concerns relating to the interpenetrating network geometry and other unaccounted-for polymer chemistries within the pores. Experiments to evaluate the filling rate in such a nanoporous system would be a recommended undertaking for future work.

Chapter 4

Nanoporous polymer liquid core waveguide fabrication

This chapter introduces the material and fabrication procedure developed in the LiCorT project for making nanoporous liquid core waveguides. The nanoporous polymer (NP) in our study was made from 1, 2-Polybutadiene (PB) which is a transparent rubbery polymer at room temperature (RT). The chapter discusses synthesis of the starting material of our work, a self-assembled diblock copolymer of Polybutadiene and Polydimethylsiloxane (PB-*b* -PDMS) by anionic polymerization. The NP polymer was obtained by selective etching of the minority block PDMS from the PB-*b* -PDMS block copolymer. The NP polymer material design and syntheis was developed by Lars Schulte and Anton Berthold, DTU Nanotech. The concepts and technique for fabrication of NP liquid core waveguide devices, in particular relating the surface modification chemistry was developed in close collaboration with Kaushal S. Sagar, DTU Chemical Engineering. In this project, the known/developed NP polymer fabrication procedure and surface modification was used to device index contrast and waveguiding. The last sections of this chapter detail the two approaches developed in this project for fabricating waveguides from NP polymers. The photo-oxidation technique was developed based on works of Ndoni et al. [99] and thiol-ene click chemistry based functionalization was initiated from works of Berthold et al. [100].

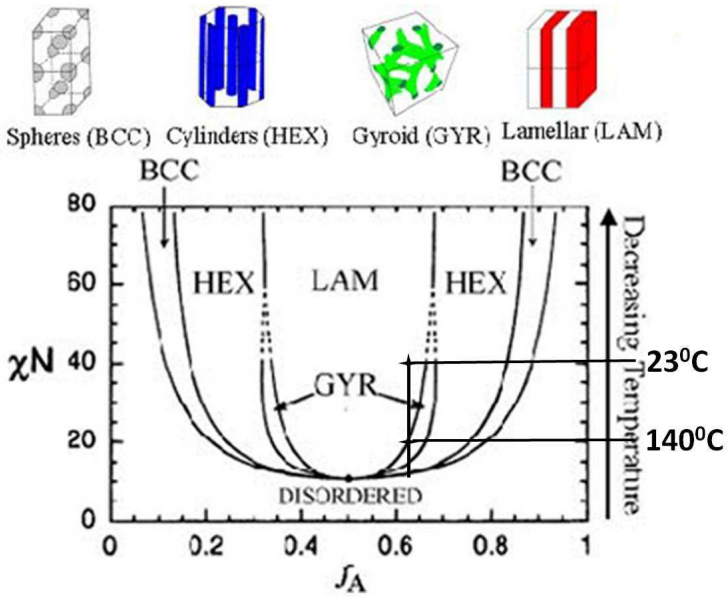

***Figure 4.1**: General phase diagram of linear block copolymers: χ_N is the Flory Huggins interaction parameter at a described size for polymer given by N. f_A is the volume fraction of one of the block polymer (A) (adapted from [101]).*

4.1 Self-assembled block copolymers

Polymers are macromolecules made up of smaller repeating units called monomers. Two or more polymers are mixed to make polymer blends. This is done to improve processing time or to achieve certain properties for applications. Such blends can be made either from compatible or incompatible polymers. In incompatible blends, different polymers remain in seperate phases in the blend. Self assembling materials can be formed by covalently connecting two incompatible polymers [102, 103]. Block copolymers are a class of polymers that can form such nano structured self assemblies. On polymerization, incompatible polymers phase separate, much like oil and water. In block copolymer systems, due to the existing covalent bond instead of phase separating, polymers form ordered morphologies such that the two phases will have little contact with each other. Material composition, sizes of polymers described as number (N) of repeating units, Flory Huggins interaction parameter, χ etc., decides on the morphology adapted by the polymer self assembly. However in all situations, the spacing between these ordered morphologies lie between 5 nm and 50 nm, making them potential materials in nanotechnology. Even though many complicated self assembling schemes or block structures are available, in our work we focus on linear AB di-block copolymers. Of the four equilibrium morphologies: lamellar, hexagonally packed cylindrical, bi-continuous gyroid and BCC spherical (all the

four morphologies are shown in Fig. 4.1), diblock developed in this work comes under gyroid morphology with the minority block polymer forming a bicontinous interpenetrating network [104, 105]. At high temperatures, the structures become disordered; this transition is called the order-disorder temperature, T_{ODT}. The transition temperature from one morphology to another is called order to order temperature, T_{OOT}.

The starting material of our work was a self assembled diblock co polymer of PB-*b* -PDMS synthesized by anionic polymerization. The starting material (PB-*b* -PDMS) was lamellar at room temperature $\approx 23°C$. Lamellar morphology was changed to gyroid (see Fig. 4.1) by heating up the polymer to its $T_{OOT} \approx 140°C$. The cross linker, activated at this temperature, covalently bonds the polymers, freezing the gyroid morphology such that even when the polymer is cooled the morphology is not destroyed.

4.2 Anionic polymerization

Polymerization can occur in different ways. One of the methods is free radical polymerization, where an initiator molecule produces some free radicals which in turn create free radical monomers. The polymer chain grows by addition of building blocks onto these free radical sites. Polymerization normally ends by termination of polymer chains either by transfering their radicals to a non radical species or forming non radical species. When the ability of polymer chains to terminate is removed, this forms the living polymerization method. This technique predetermines molar mass and controls the end groups for the polymer. Thus for tailor making a diblock polymer, living polymerization offers a high degree of control over polymer chain structures. Anionic polymerization is a living polymerization technique which offers sequential monomer addition [106]. In this technique, the added initiator attacks a monomer and transfers charge, which further attacks a new monomer and thus the chain propagates. The reaction goes on as follows:

$$\begin{gathered} step(1) : I^- + M \Rightarrow I - M^- \\ step(2) : I - M^- + M \Rightarrow I - M - M^- \\ ..... \\ step(n) : I - [M - M^-]_n - M^- \end{gathered} \tag{4.1}$$

where step (1) is the initiation step in which the initiator (I) transfers charge to monomer (M), step (2) is the propagation and transfer step in which the monomer transfers charge to another, and step (n) is the termination step. An acid is used to terminate the process. Polymerization is possible at all stages and times of the reaction as a macro anion is always present until it is terminated. A new monomer can be added without introducing a new initiator in this technique, providing control over the degree of polymerization.

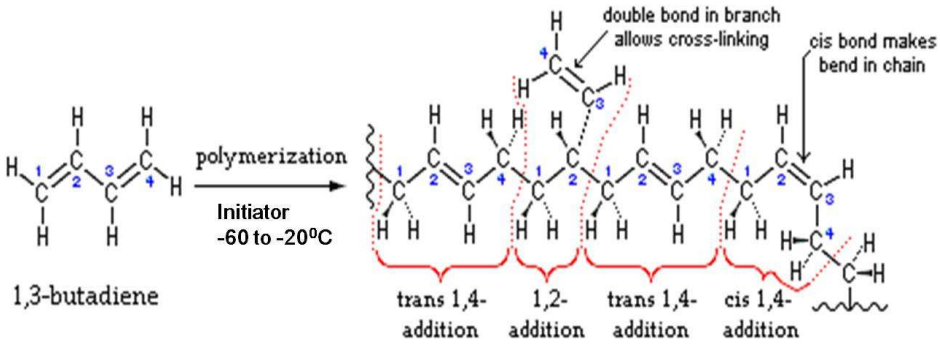

***Figure 4.2**: Synthesis of 1,2 PB from polybutadiene [107]*

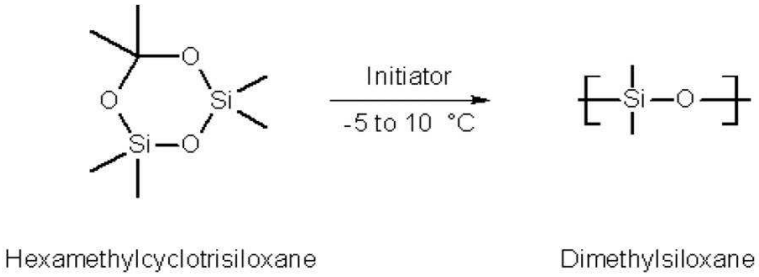

***Figure 4.3**: Synthesis of polydimethyl siloxane*

The diblock polymers in this work are synthesized using anionic polymerization, allowing us to maintain the molecular weight and distribution in a controlled fashion. The nanoporous material used in this project was made of polybutadiene (PB). This was obtained from the diblock copolymer PB-*b* -PDMS made by anionic polymerization. The sequence of adding different monomers to the living polymerization matters a lot as the reactivity of the living anion differs with type of monomers. Thus in this work, the initiator *sec*-butyl lithium was added with Polybutadiene monomer before adding the PDMS monomer, i.e., $PB^{-}li^{+}$ is prepared first and then the D_3 (PDMS). In this case, reverse addition does not work. The reactions can be terminated by adding an acid.

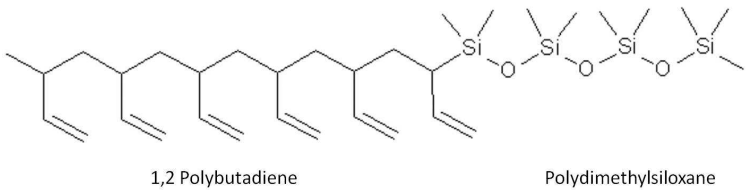

***Figure 4.4**: The structure of developed PB-b* -PDMS block copolymer

PB was synthesized from 1,3-butadiene gas, which is highly reactive at room temperature and polymerizes quickly. Normally polymerization of butadiene is carried out using a free radical polymerization technique as shown in Fig. 4.2. Based on the reaction conditions, choice of initiators and added amounts of monomers, the ratio between 1,2-PB and 1,4-PB can be controlled. In our polymerization 1,2-PB is formed to 85-95%. Synthesis of PDMS was obtained with ring opening polymerization of cyclic siloxane, hexamethyl cyclotrisiloxane (D_3) as shown in Fig. 4.3. Here the PB-macro anion in anionic polymerization acts as the initiator for the reaction.

4.2.1 Synthesis of PB-*b*-PDMS block copolymer

(The work was carried out by Lars Schulte under Dr. Ndoni, DTU Nanotech, Denmark).

Anionic polymerization was used to synthesize PB-*b*-PDMS block copolymer. Tetrahydrofuran (THF) was used as the reaction solvent (purity$\geq$ 99.9%, GC grade from *Sigma Aldrich*). THF and the monomers (1, 3 butadiene (1,3-BD) and cyclic siloxane) were purified to remove oxygen. THF was added to a dry, argon filled reaction vessel. The temperature was reduced to -60°C on addition of anionic initiator, sec butyllithium. On addition of 1, 3-BD, the temperature was raised to -20°C. After 3 h, cyclic siloxane was added. Butadiene polymerization is very quick compared to PDMS polymerization. The reaction was terminated using an acid, chlorotrimethylsilane. Solvent was removed in a rotavapor and the polymer was precipitated in methanol (purity $\geq$ 99.9%, HPLC grade from *Sigma Aldrich*). A viscous white polymer was yielded. The structure of the final block copolymer obtained is shown in Fig. 4.4. Fig. 4.5 shows the anionic polymerizaiton of PB-*b*-PDMS block copolymers. The reaction is explained step by step.

4.3 Synthesis of NP polymers from self-assembled PB-*b*-PDMS

(The work was carried out in close collaboration with Kaushal S Sagar, DTU Chemical Engineering, Technical University of Denmark, Denmark).

4.3.1 Cross linking

Cross linking (Fig. 4.6) is a process where two or more polymers are chemically joined by a covalent bond. These processes are carried out in the presence of cross linkers/cross linking reagents which are molecules containing reactive ends that attach chemically to a specific functional group in

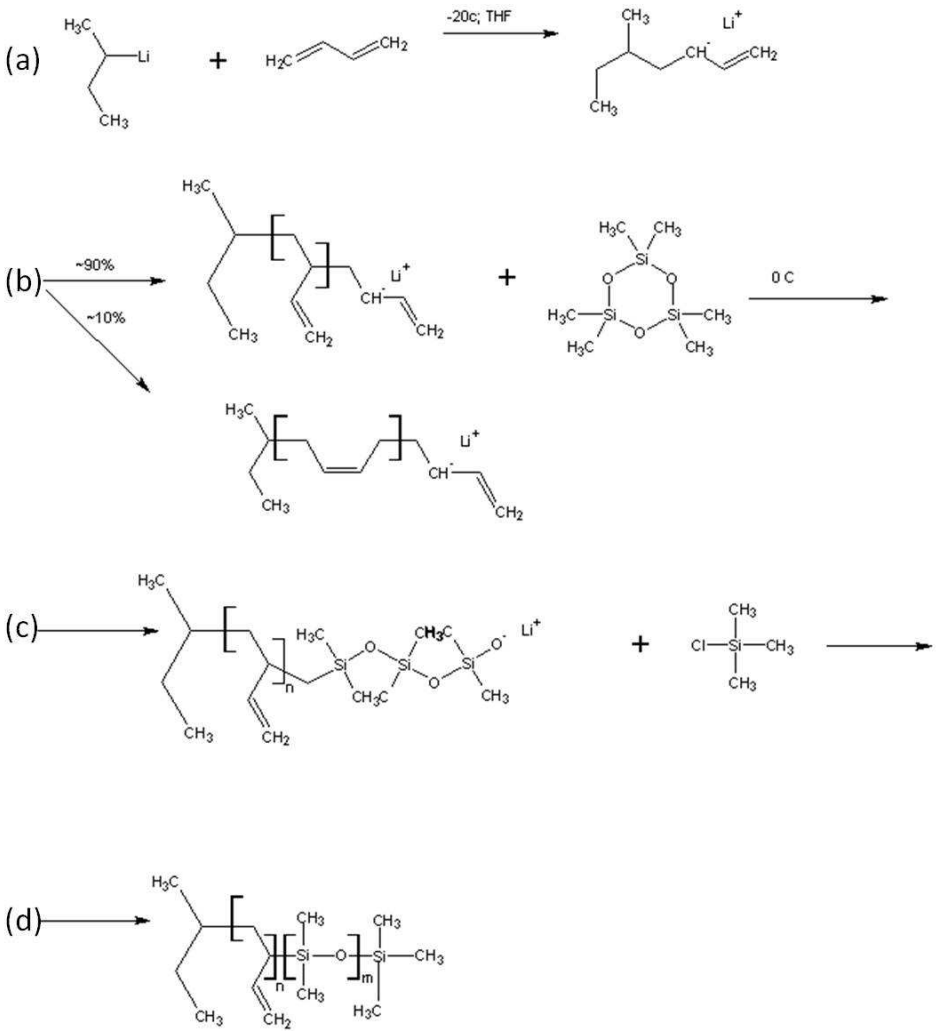

Figure 4.5*: Living anionic polymerization of PB-b-PDMS block copolymers. (a) 1,3 butadiene treated with intiator make the PB-macro anion (initiation step); (b) on addition of D_3 (cyclic siloxane) dimethylsiloxane monomers are added to the polymer chain (propagation step); (c) an acid is added to stop the polymerization (termination step); (d) the final PB-b-PDMS block copolymer.*

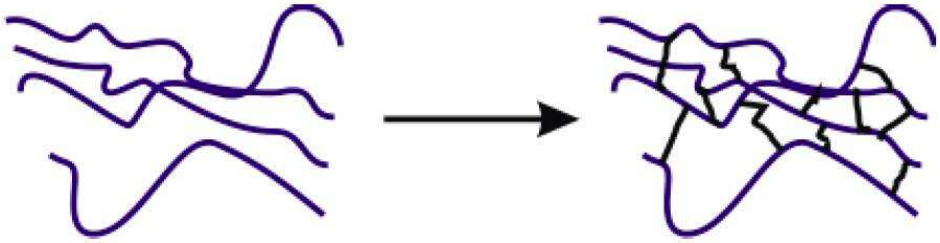

***Figure 4.6**: Cross linking of polymer chains.*

the polymer. Cross linkers are selected based on their chemical reactivity and other chemical properties. Crosslinking can be initiated in different ways using heat etc. In block copolymers, crosslinking close to the T_{OOT} allows selection of morphology. In this work, crosslinking is targeted above T_{OOT} for achieving gyroid morphology (see Fig. 4.1). Porosity in a block copolymer is introduced by removal of the expendable minority block. Such a removal provides considerable mechanical stress to the majority matrix components. As PB has very low T_g, crosslinking helps in achieving the required mechanical properties.

Cross linking in our system was initiated by heat. Dicumyl peroxide (DCP, (purity $\geq$ 97.0%, TLC grade from *Fluka*)) was used as the crosslinker since the radical forming temperature of DCP lies close to the gyroid phase of the copolymer. At initiation temperature the peroxide breaks down into two radicals, which in turn abstracts hydrogen from the tertiary carbon in the 1, 2-PB chain. This radical attacks the double bonded carbons in the other PB chains, transfering radicals. Thus only a small amount of crosslinker was required. To ensure high degree of cross linking (50-60%), 1 mol% of DCP was used with respect to the number of double bonds of the PB component. Initially, the PB-*b*-PDMS block copolymer was solvent-casted in THF with 1 mol% of DCP. The material is further cross linked at $140°C$ in an argon/nitrogen atmosphere for 2 h in order to fix the gyroid morphology. A volume fraction of 0.60 for the PB block in the original block polymer was controlled by the polymer synthesis and the obtained self-assembled morphology was of the cubic symmetry $Ia\bar{3}d$, known also as gyroid morphology [108, 99]. This morphology provides bicontinuous porosity and high transparency, which are important for our work.

4.3.2 Etching PDMS from PB-*b*-PDMS block copolymer

The PDMS minority block was removed using the etchant tetrabutylammonium fluoride (TBAF) dissolved in THF (1.0 M in THF from *Sigma Aldrich*).

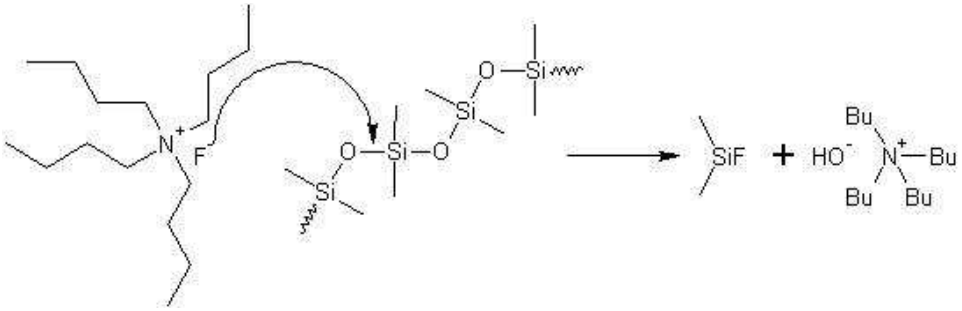

***Figure 4.7**: Fluoride ions attack the Si-O bond thus etching the PDMS minority block.*

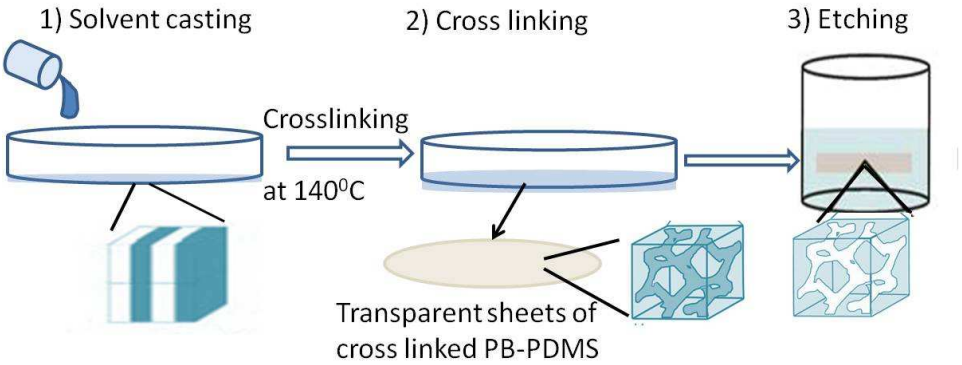

***Figure 4.8**: The starting material of PB-b-PDMS was solvent-casted onto a petridish mixed with THF and DCP. The petridish was placed in an argon/nitrogen chamber and the temperature was increased to 140° C. The crosslinked polymer was chemically etched and washed.*

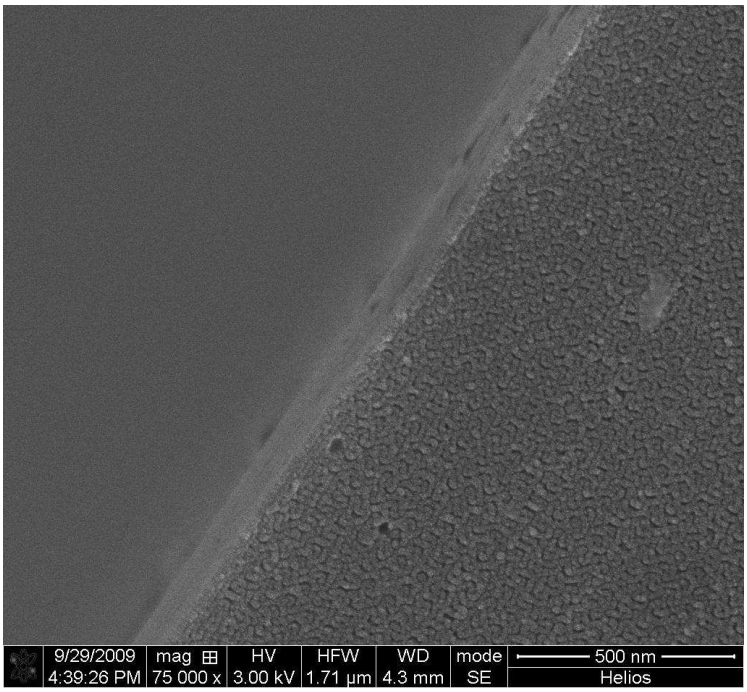

***Figure 4.9**: SEM image of NP polymer cross section.*

The released fluoride ions attack the Si-O bond, etching the PDMS block out of the diblock system. Fig. 4.7 shows how fluoride ions attack the Si-O bond. Swelling the matrix with THF can lead to cracking when the etched sample dries; steps were taken to optimize this part of the fabrication technique. The etching was done using TBAF at three times molar excess, relative to the repeating units of PDMS. Etching was carried out for 36 h followed by cleaning using THF and methanol. The NP polymer was cleaned initially using a mixture of 60% THF and 40% methanol for an hour, the percentages were reversed in the second wash and finally the solution was fully replaced by methanol. The step by step process of cleaning was used to introduce methanol slowly into the matrix and thus reduce the risk of cracking and shrinkage.

Fig. 4.8 shows a schematic representation of the fabrication of NP polymers. The NP polymers were prepared initially by solvent casting the PB-*b*-PDMS block copolymer in THF with DCP. The volume of the solvent casted polymer determines the thickness of the NP polymer. For obtaining NP polymer sheets of thickness 500 μm in a petri dish of radius 5 cm, corresponding volume (same as $3.14\times50^2\times0.5$) of solvent was casted. 1 mol% of DCP with respect to the number of double bonds of the PB component was used. The petri dish was placed in an air tight chamber that keeps an argon/nitrogen atmosphere. The material was cross linked at 140°C for 2 h. The cross

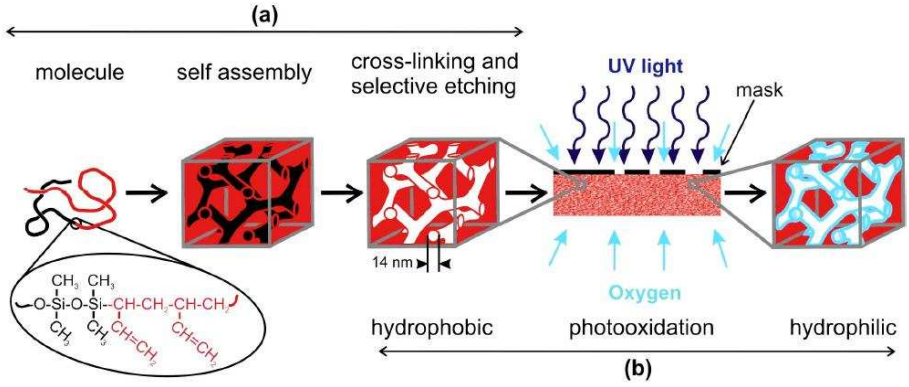

***Figure 4.10**: Conceptual illustration of UV patterned SLCW (a) NP polymer fabrication from starting material PB-b-PDMS (molecule highlighted in red is PB and in black is PDMS); (b) hydrophilization of polymer air interface using UV light in the presence of oxygen. A UV mask is used to obtain selective hydrophilization. Figure adapted from [99].*

linked PB-*b*-PDMS copolymer was removed from the petri dish and placed in TBAF etching solution. The amount used was three times molar excess relative to the repeating unit of PDMS. The copolymer was etched for 36 h. The end product was transparent robust sheet of nanoporous polymer. The NP polymer was then cleaned with THF and methanol solution for a total of 16 h [109]. Fig. 4.9 shows the scanning electron microscope (SEM) image of the NP polymer. The interpenetrating morphology is clearly observed in the picture.

4.4 NP waveguide fabrication

NP polymers derived from such self assembling precursors are materials with large internal surface and high structural order. They can play a major role as platforms in areas like sensing, chromatography, size separation etc. The self assembled block copolymer and the NP polymer obtained can be considered as binary alloys with length heterogeneity on a scale much lower than that of the wavelength of visible light. Thus visible light observes such a nanoporous diblock matrix as a single entity with some effective refractive index, n_{eff}. A detailed derivation of the effective index is given in Chapter 3. The n_{eff} of the block copolymer or NP can be calculated using Lorentz-Lorenz relation [23, 110].

$$\frac{n_{eff}^2 - n_1^2}{n_{eff}^2 + 2} = V_2 \frac{n_2^2 - n_1^2}{n_2^2 + 2}, \tag{4.2}$$

where n_1 and n_2 are the refractive indices of the majority and the minority component respectively, and V_2 is the volume fraction of the minority component of the polymer matrix, i.e., PDMS for the PB-*b*-PDMS self assembly and air for the 1,2-PB NP polymer matrix. Thus a 44% volume porosity in the polymer due to etching of minority block PDMS induces an n_{eff} change from 1.46 to 1.26 as PDMS (n=1.40) [111] is replaced with air (n=1). The n_{eff} of 1.26 makes 1, 2-PB NP polymer a very suitable cladding material for liquid core waveguiding as the value is lower than the refractive index of water $\approx$ 1.33. The NP polymer is a naturally hydrophobic material. Altering the chemical composition at the polymer-air interface, nanoporous polymers can be rendered hydrophilic. When immersed in water, such an altered polymer uptakes water in its nanopores, increasing the n_{eff} of the matrix as air (n=1) is replaced with water (n=1.33). This uptake induces a Δn_{eff} of 0.17. Such an index change obtained due to modification/functionalization of the polymer-air interface is exploited to guide light via total internal reflection technique. A selective hydrophilization of the polymer and water uptake will create regions of lower and higher refractive indices. This situation was utilized to guide light in the region of hydrophilization, making the hydrophobic NP polymer an efficient cladding layer. The index change induced in these systems is governed by the liquid infiltration in the hydrophilized regions, thus the core will always have higher n_{eff} than the cladding material. As water/liquid does not form the entire core of these waveguide systems, they do not fully fall under the criteria of liquid core waveguides. Hence, they are rephrased as solid liquid core waveguides (SLCW).

In our work we have adapted two different techniques for hydrophilizing the air-polymer surfaces. In one technique, photo-oxidation was used to modify the polymer-air surface. This method was developed based on works of Ndoni et al. [99]. The second approach was to functionalize the surface by thiol-ene photochemistry. Mercaptosuccinic acid (MSA) or sodium mercaptoethanesulfonate salt (MESNA) were grafted onto the pore wall by reacting with the pendant vinyl groups of 1,2-PB nanopores. This method was developed based on works of Berthold et al. [100].

4.5 UV patterned NP SLCW

NP polymers derived from self organized block copolymers has vast internal surfaces (50-500 m^2g^{-1}), which due to a bi-continuous interpenetrating network is readily accessible to gases. Ndoni et al. [99] showed that by controlled photo-oxidation, the polymer air interface of the NP polymer can be chemically modified without affecting the nanostructure. Photo-oxidation in general involves oxygen gas permeation into the material matrix under a photochemical reaction that is initiated or mediated by UV

radiation (300 nm< λ <350 nm) [99].

Photo degradation is the deterioration of a polymer molecule due to absorption of photons that lie in the IR, visible or UV range. Photo-oxidation is a type of degradation of polymer occurring in presence of oxygen or ozone. With UV irradiation, impurities present in the polymer matrix absorb radiation, forming radicals that attack tertiary or allylic hydrogen forming polymer radicals [112]. Oxygen in the surroundings reacts with the radicals to produce polymer peroxy radicals and thus create polymer hydro peroxides and new polymer radicals. Hydroperoxides are of the form ROOH where R is any organic group. α, β unsaturated carbonyls are formed by photolysis of these hydroperoxides [113]. Thus, such a photo-oxidation reaction is expected to result in the formation of hydroxyl (-OH), ether (R-O-R'), carbonyl (R-CO-R') and carboxyl (R-CO-OH) groups.

Fig. 4.10 shows the conceptual scheme of making UV patterned SLCW. The first part of the illustration describes how NP polymer is derived from the PB-*b*-PDMS molecule. A UV exposure (300-350 nm) for 24 h at a temperature of 36°C in the presence of oxygen, results in hydroxyl and carboxyl photo products at the air polymer interface making the hydrophobic surface hydrophilic [114]. A UV mask was used to produce selective hydrophilicity in the polymer matrix. Uncollimated polychromatic (300-400 nm) UV source of intensity 14-16 mW/cm^2 was used for modifying the devices.

4.6 Thiol-ene click chemistry functionalized NP SLCW

Owing to longer processing time for photo oxidative hydrophilization, an alternative technique called 'thiol-ene click chemistry' was opted. Thiol-ene simply indicates addition of thiol (S-H) to an -ene bond (double or triple bonds). Thiols react highly efficiently with carbon-carbon double bonds (C=C) by hydrothiolation. The thiol-ene reactions can be initiated thermally and photochemically. In photochemically (365 nm) initiated thiol-ene click chemistry, the process occurs by initiation using photoinitators (PI). In this project two types of initiators were used, cleavage type PI 2, 2-dimethocy-2-phenyl acetophenone (DMPA) and H- abstraction type PI benzophenone (BP) [115].

A typical chain process in thiol-ene click chemistry is schematically illustrated in Fig. 4.11. Thiol under treatment of PI and irradiation, results in thiyl radical, RS*, and some byproducts [116]. The cycle propagates by addition of thiyl radical to the C=C bond generating an intermediate carbon centered radical which attacks thiol, making thiyl radicals and byproducts.

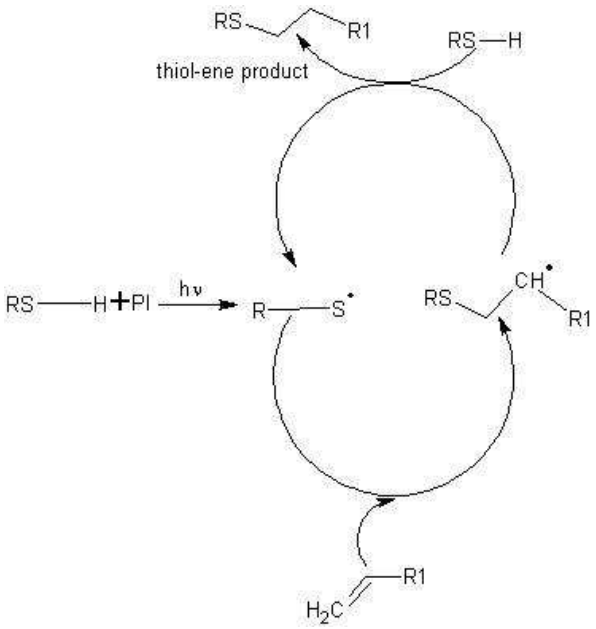

***Figure 4.11**: Mechanism of hydrothiolation of C=C bond in presence of a photoinititor and UV radiation [115].*

Two different types of thiols were used in this project, mercaptosuccinic acid (MSA) and sodium mercaptoethanesulfonate (MESNA). Photochemically initiated thiol-ene click chemistry was used to graft PB NP polymers with carboxylic acid groups. This will induce hydrophilicity in naturally hydrophobic PB polymers.

4.6.1 Thiol-ene click chemistry using MSA

Schematic of the working principle behind the thiol-ene click chemistry using MSA is illustrated in Fig. 4.12. Photo initiator BP absorbs photons and becomes a radical. On hydrogen abstraction reaction of MSA, sulfenyl radicals are formed which further attack the pendant double bond in the 1,2-PB NP polymer. The hydrothiolation of pendant C=C bond in 1, 2 PB NP grafts carboxylic acid groups onto the air-polymer interface. Functionalized PB abstract hydrogen from thiol/MSA making an active sulfenyl radical. The click chemistry is then repeated due to the active radical [115]. For cases with DMPA as photoinitiator, similar modification would be observed. As thiols are highly reactive, extreme care had to be taken to prevent stray light from making contact with the samples. A 500 mM thiol concentration was mixed in 10 mM DMPA/BP. The NP polymer was immersed in MSA thiol solution for 30 min allowing considerable loading time. Photolithography was done in a chamber as shown in Fig. 4.13. A flood exposure collimated

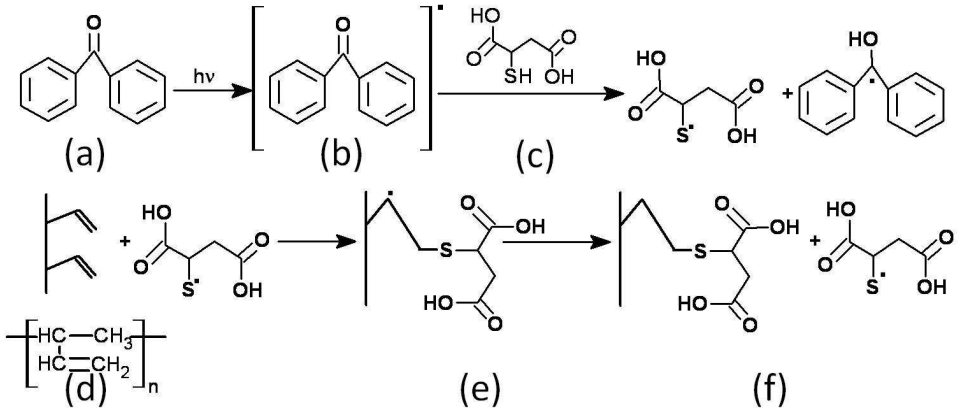

***Figure 4.12**: Schematic illustration of working principle of hydrophilization of 1, 2 PB NP polymer. (a) Photoinitiator(PI) Benzophenone(BP); (b) under absorption of photon, radicals are formed in BP; (c) the hydrogen abstraction reaction on thiol Mercapto Succinic Acid(MSA) makes a sulfenyl radical; (d) the pendant double bond in 1,2 polybutadiene chain is attacked by this radical; (e) hydrothiolation of C=C bond results in carboxylic acid groups in the PB pendant; (f) 1,2 PB abstract hydrogen from thiol to stabilize causing sulfenyl radicals and the click chemistry (reactions d, e and f) is repeated.*

source of 100 W (Xe)(Newport) at I line ($5.2 \pm 0.1\ mW/cm^2$) was used for thiol-ene grafting. Selective click chemistry was acquired using a photolithography UV mask (a laser beam or beam of electrons (e-beam writer) is used to transfer the desired pattern onto a layer of chrome supported on a fused quartz square substrate. This forms the mask for photolithography patterning). The NP polymers were aligned and adhered onto the photolithography mask. This was then placed on an aluminium chuck. The chuck was filled with an excess of thiol solution to reduce crystalization of thiol during exposure. The chuck acts as an antireflecting surface ensuring light exposure only in the selected regions. The whole setup was placed in a polycarbonate box with quartz window to avoid thiol leaking. After exposure for 30 min, the polymers were washed couple of times in ethanol for 30 min. To further reduce exposure time, MSA was replaced with MESNA.

4.6.2 Thiol-ene click chemistry using MESNA

MESNA is a thiol which consists of a sulphonated salt end group. Fig. 4.14 shows the chemical formula of MSA and MESNA thiol molecules. MESNA solution was prepared in 3:1 methanol and water mixture. The photoinitiator used was 10 mM DMPA. NP polymers were immersed in the thiol

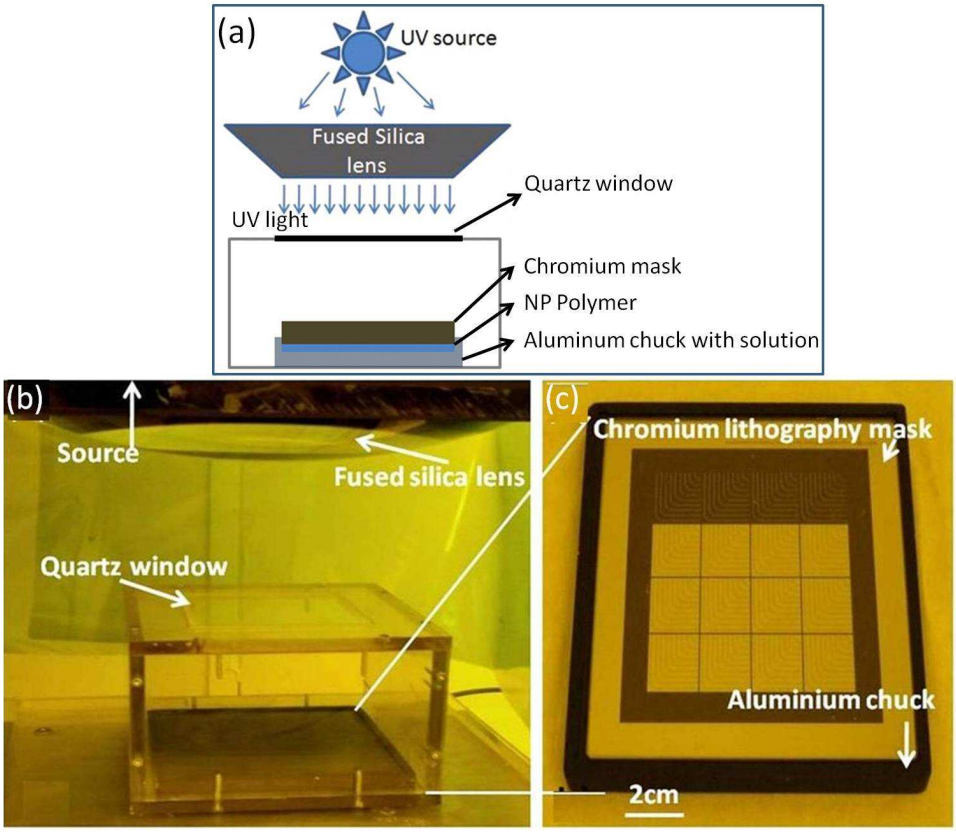

***Figure 4.13**: Thiol-ene click chemistry setup. (a) Schematic illustration of the chamber used for thiol-ene click chemistry; (b) Image of the chamber dedicated for thiol-ene photo grafting. Collimated Newport UV source used for irradiation; (b) enhanced picture of chromium lithography mask in aluminium chuck [117].*

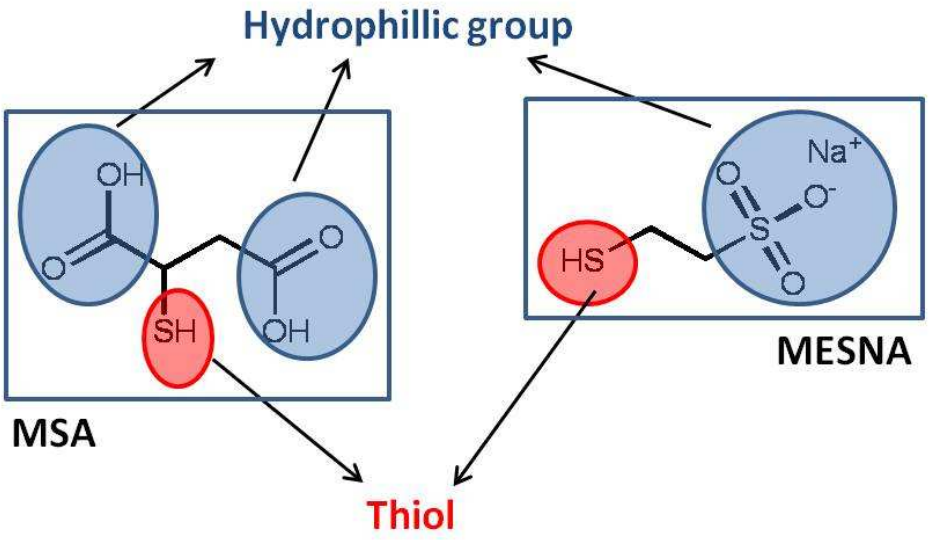

***Figure 4.14**: Chemical formula and representation of hydrophillic and thiol groups in the thiol molecules used for photografting.*

solution for 30 min to ensure complete loading. Similar exposure conditions as in MSA modification was used. Unlike in MSA, no excess solution was required during the exposure as the irradiaition time was only $\approx$ 5 min. The exposed polymers were washed in methanol water mixture for 30 min and the process was repeated with a fresh solution. A final wash in THF for 30 min removed all residual MESNA from the polymer pores. After adequate drying, loading of water infiltrates the exposed regions, inducing index increase and thus confinement.

To summarize, the starting material of SLCW fabrication, PB-*b*-PDMS self assembly, was made using anionic polymerization and cross linking. By selective etching of the minority block PDMS from the self assembly, 1, 2-PB NP polymers were fabricated. UV associated surface modification (photo-oxidation assisted or thiol-ene click chemistry modified) of these naturally hydrophobic polymers render them hydrophilic. Water infiltration in the hydrophilic regions increases the effective refractive index. This was exploited to selectively confine light in these regions and thus fabricate solid liquid core waveguides from NP polymers.

Chapter 5

Solid liquid core waveguide performance

For testing the performance of NP polymer LCW technology, a number of experiments were designed and carried out. These involve studying the confinement of light in hydrophilic regions with optical loss measurements. The chapter presents the design and characterization of SLCW developed in the LiCorT project. Performances of both photo-oxidation induced and thiolene click chemistry induced guiding is individually addressed, compared among themselves as well as with currently available state of art LCWs.

5.1 Photo-oxidation modified waveguides

5.1.1 Proof of concept

A UV patterned NP SLCW was fabricated as shown in Fig. 5.1. On UV treatment in the presence of oxygen, NP polymer turns hydrophillic. To verify water infiltration in the UV treated regions, contact angle measurements were performed (Fig. 5.2). Contact angle (CA), θ, quantitatively measures how much a solid surface is wetted by a liquid. Contact angle can be assessed directly by measuring the angle formed between the solid and the tangent to the drop surface as shown in Fig. 5.2. A high contact angle indicates poor wetting or high degree of hydrophobicity of the surface. At the begining of the measurement, NP polymers showed a CA of 69°. For untreated NP polymer, the value does not reduce much over time. The slight variation

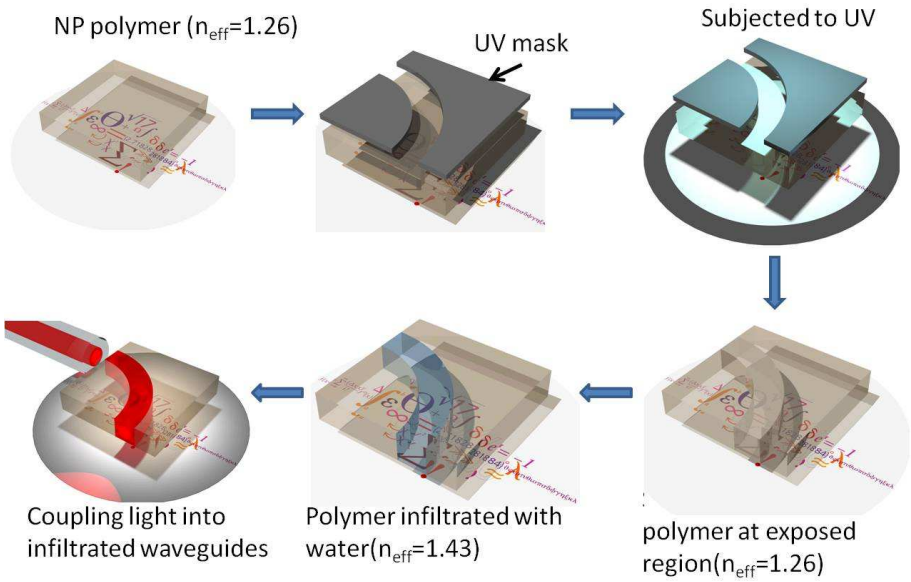

***Figure 5.1**: Schematic illustration of photo-oxidaiton of NP. On infiltrating the exposed region with water, the n_{eff} changes and exploited to couple light along.*

of CA may be due to evaporation of water. In UV treated samples, CA reduces to 0° within 7 min of measurement, indicating complete wetting of the devices.

In addition to contact angle measuremets, an organic fluorescent dye Rhodamine 6G [118] in aqueous solution was used to assess infiltration. Rhodamine 6G is an organic fluorescent dye which excites under green light (532 nm) and fluoresces around 590 nm. The fluorescence signal from the dye was used as an indication of infiltration into the nano pores (Fig. 5.3). The selectively exposed NP samples were immersed in dye solution of 0.92 μM concentration for 30 min. The polymer was then washed in deionized (DI) water and dried. A 14 mW solid state laser was used to excite exposed and unexposed regions. The emitted spectra were collected using a spectrometer (*OceanOptics* HR 2000). We observe fluorescence signal only from the exposed region.

Even though water evaporation occurs from the infiltrated pores over time, measurements within a range of a couple of minutes were not subject to major issues of evaporation. In photo-oxidation modified waveguides, water evaporation issues were not explored.

Fourier transform infrared (FTIR) spectroscopy was used to analyze the photo products obtained from photooxidation (*PerkinElmer* Spectrum One^{TM} FTIR Spectrometer using an Attenuated Total Reflectance (ATR) measur-

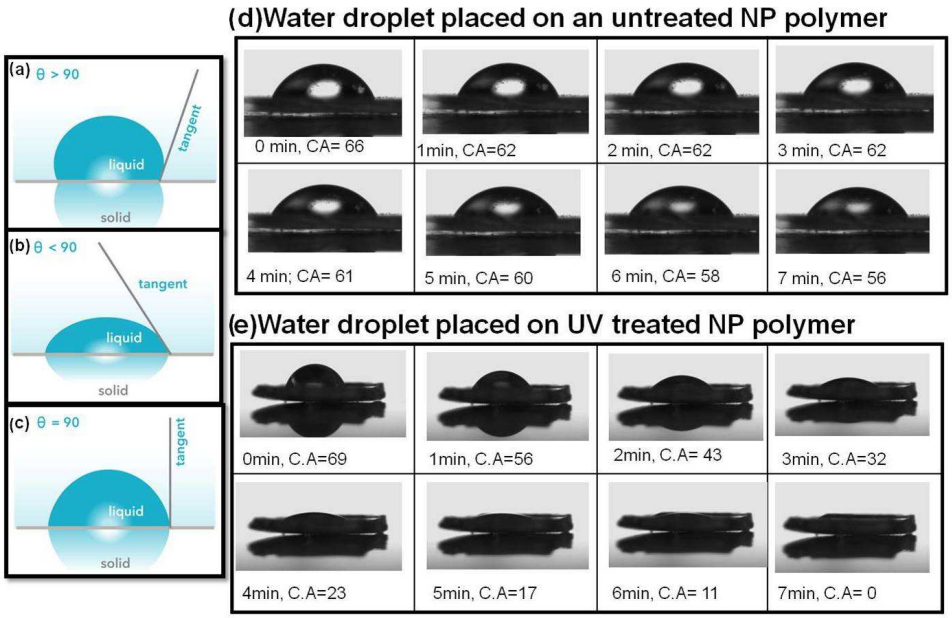

***Figure 5.2**: Contact angle θ gives a quantitative measure of wetting of a solid by a liquid. (a) θ >90° shows poor wetting, while ; (b) θ <90° shows better wetting; (d, e) Contact angle measurements on untreated and UV treated NP polymer. The measurements were taken every minute for 7 minutes.*

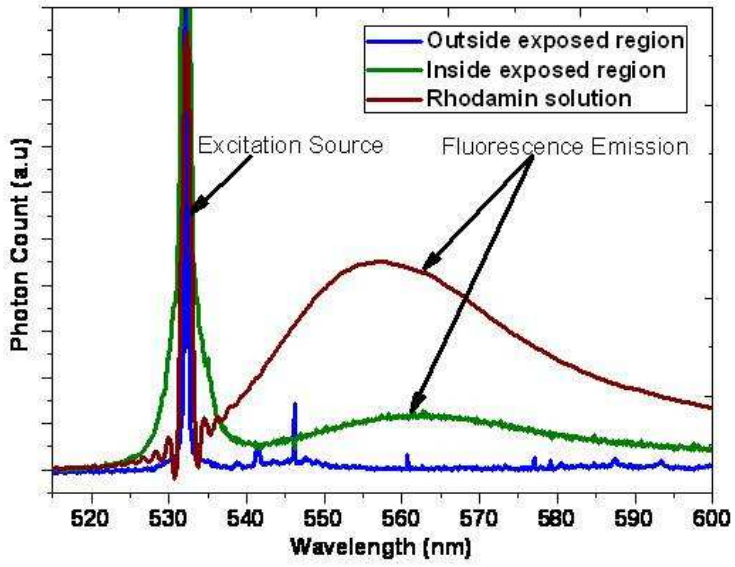

***Figure 5.3**: Spectra obtained from Rhodamine 6G treated NP polymer when excited with green light. Both exposed and unexposed regions were excited with green light. Rhodamine 6G solution spectrum is also provided for reference.*

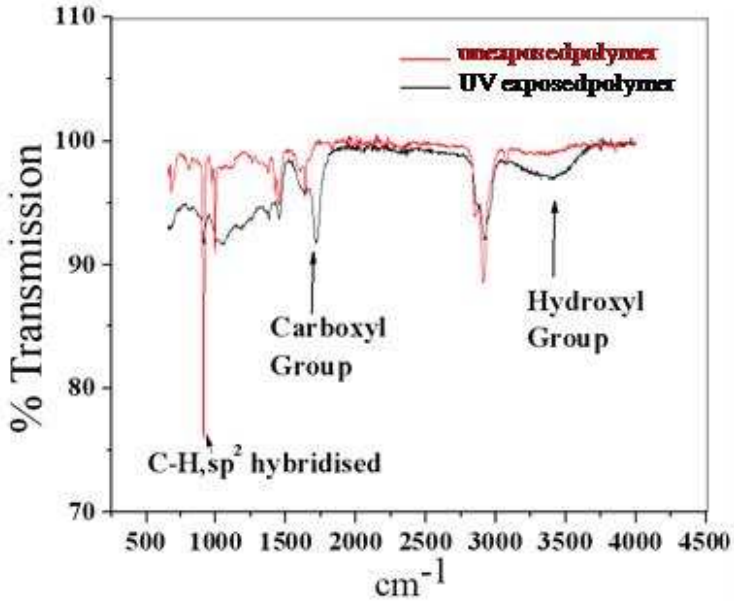

***Figure 5.4**: FTIR spectrum of NP polymer, red line representing the spectra of unexposed NP polymer while black line is the UV exposed NP polymer. The presence of carboxyl and hydroxyl group confirms hydrophilicity of the NP polymer.*

ing head with a resolution of 4 cm^{-1} and summation of 32 scans). Fig. 5.4 shows the FTIR spectra obtained from unexposed and UV exposed 1, 2-PB NP polymer. After UV treatment of the polymer, new absorption bands in the range 3100-3670 cm^{-1}, 1710 cm^{-1} and some overlapping peaks in 1500-650 cm^{-1} were seen in the spectrum. This corresponds to the hydroxyl and carboxyl groups introduced at the air-polymer interface. With exposure, these peaks grew while C-Hsp^2 hybridized peaks from the pendant double bonds reduced. The consumption of double bonds clearly indicate modification of the air-polymer interface. The level of hydrophilicity was determined by the population density of the hydrophillic (carboxyl and hydroxyl groups) species at the interface.

NP polymers were selectively UV exposed with a UV mask (500 μm) as shown in Fig. 5.1. The polymer was immersed in deionized (DI) water for 10 min. To check waveguiding, light of 655 nm was coupled onto the exposed region. In a dry/non infiltrated waveguide or device, light is scattered and travel in a straight path without getting guided as shown in Fig. 5.5a. On infiltrating with DI water for 10 minutes, light gets guided through the exposed regions (Fig. 5.5b). In addition to the proof of concept illustrations, confinement of light in waveguides was also studied. A bend waveguide of dimensions 500 μm$\times$500 μm was patterend using UV lithography. The device was immersed in water for 10 min to allow complete infiltration in the

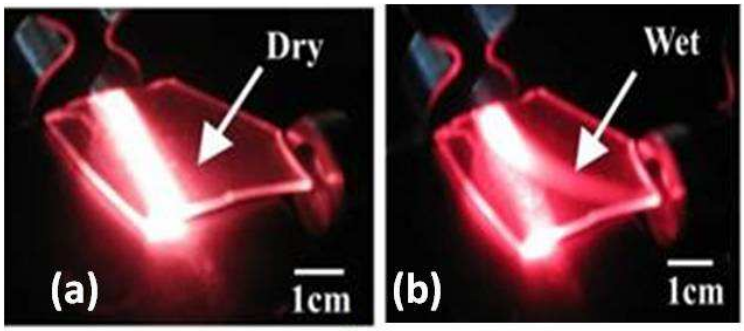

Figure 5.5*: Proof of concept of guiding in NP polymer: a wet device guides the incident light while dry device scatters light. Camera images of (a) dry; and (b) wet device.*

exposed region. A 400 μm multimode (MM) fiber was used to couple light (655 nm) into the waveguide. Similar MM fibers were used to collect light coming from the waveguide onto a HR 2000 spectrometer. The collection fiber was placed on an XYZ translation stage from *Thorlabs Inc.* The setup was used to study the confinement of light in the exposed region. Photon counts obtained at each translation were measured, corresponding to the intensity of light. The experimental setup and intensity variation observed is shown in Fig. 5.6. The intensity of light observed drops gradually as the output fiber translated away from the waveguiding region in both the X and Y dimensions. This clearly indicated confinement of light within the exposed region.

5.1.2 Characterization of Waveguides

The SLCWs were characterized by measuring the losses in the waveguide. Four types of losses occur in rectangular waveguides with bends: input and output coupling, transition, radiation and propagation loss [85, 119]. All the losses are explained in detail in Chapter 3. As the shape of the waveguides were not optimized, our initial characterization studies only included propagation and bend loss.

Propagation loss in NP SLCW was studied using substitution techniques. As standard cutback techniques were destructive, waveguides of different lengths were UV patterned in the same NP polymer device. With the assumption that all the waveguides were subjected to similar coupling losses, the substitution technique was used to measure the propagation losses in these waveguides. A 90° bend was introduced into the pattern such that multiple waveguides with different propagation lengths can be incorporated into a 1.5 cm $\times$ 1.5 cm NP polymer chip. Thus a UV lithography mask

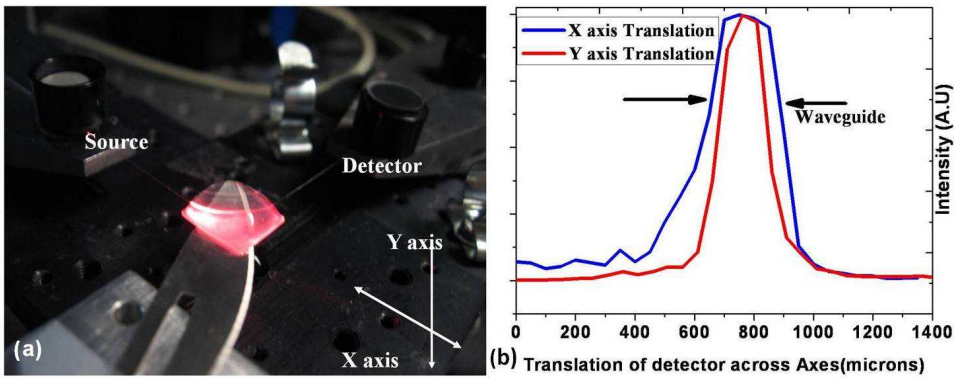

***Figure 5.6**: Proof of confinement of light within exposed regions. (a) Experimental setup; (b) intensity variation of light in exposed regions as the detector was translated along the X and Y-axis.*

was designed in L-Edit software such that a 90° bend waveguide of radius, R = 2 mm, was designed sandwiched between straight waveguides of varying lengths 2 mm, 4 mm, 6 mm etc.

Waveguides of cross section 200 μm×200 μm were defined with UV lithography masks as shown in Fig. 5.7b, inset. The experiment setup used for measuring the losses is shown in Fig. 5.7a. A He-Ne laser (632 nm) was butt coupled onto the SLCW exposed region using a 62.5/125 μm MM fiber. The light was coupled out into an optical spectrum analyser (OSA) (Ando AQ-6315A). The incident optics, collection optics and device were mounted on XYZ translation stages from *Thorlabs.Inc* (MBT616). This was used to precisely align waveguide device with input and collection fiber. Comparison of optical power coupled into and out of each waveguide provides the attenuation/loss observed in them. The loss in waveguides were expressed in dBs. The propagation loss along a straight waveguide was obtained by subtracting the losses from 90° bend waveguide of radius, R = 2 mm. This removes the coupling and radiation losses. Radiation losses were observed in the curved section of the waveguides (Chapter 3). The propagation loss was evaluated by plotting waveguide loss as a function of propagation length. In Fig. 5.7b, a linear fit to the data gives the propagation loss per millimeter (mm) observed in NP waveguides. The constant A represents the transition losses when light propagates through different types of waveguides (straight and bend). A transition loss of 3.8 ± 0.5 dB and a propagation loss of 0.62 ± 0.03 dB/mm were obtained in the photo-oxidation modified NP SLCWs.

Bending/radiation loss in these waveguides were also evaluated experimentally. A UV mask with 90° bend of different bend radii ranging from 1.75 mm to 11.75 mm was designed for the purpose. Each of the bend waveguides

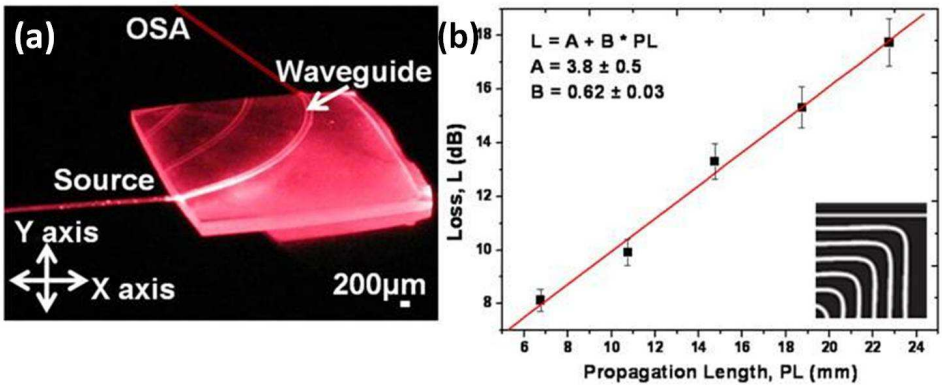

***Figure 5.7**: (a) Experimental setup for measuring propagation and bend loss in the photooxidation modified NP LCW; (b) loss (L) in waveguides with different lengths as a function of propagation length (PL). The solid curve is a linear fit to the measured data. (Inset) 2 cm×2 cm UV mask designed for measuring propagation loss in NP polymer SLCW.*

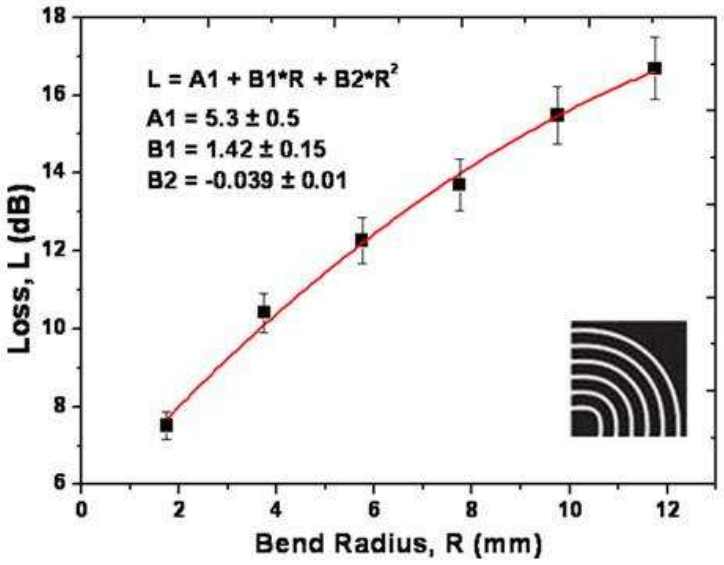

***Figure 5.8**: Loss (L) in waveguides with different bend radius as a function of bend radius (R). The solid curve is a polynomial fit to the measured data. (Inset) 2 cm×2 cm UV mask designed for measuring radiation loss in NP polymer SLCW.*

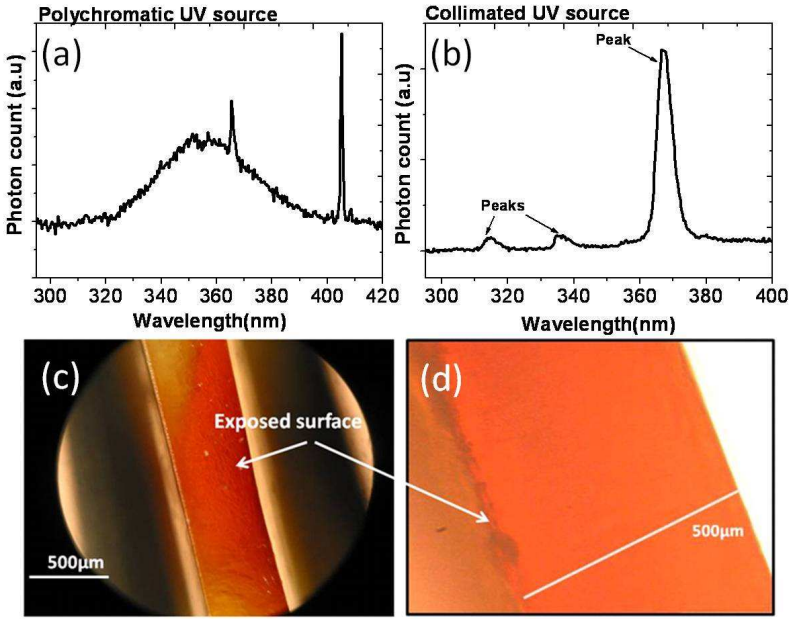

***Figure 5.9**: UV spectra emitted from the UV irradiation sources. (a) UV polychromatic source; (b) collimated UV source; (c) cross section of polychromatic UV source irradiated waveguides, infiltrated with NaOH solution, (d) cross section of collimated UV source irradiated waveguides, NaOH infiltrated.*

were sandwiched between 2 mm long straight waveguides. Loss in the bend region was obtained by removing the coupling and propagation losses from the straight waveguide section in the design. The loss in the bend region was plotted as a function of bend radii as shown in Fig. 5.8. The total loss obtained in the region was a sum of transition, propagation and radiation loss in the curved/bend region of the waveguide. This was seperately interpreted by fitting a polynomial to the plotted data. The intercept A1 partially indicates transition losses when light propagates from the straight section to the bend section of the waveguide. The linear coefficient B1 contributes mainly to the propagation and partially to the radiation losses in the bend region. Each bend waveguide has a propagation length of $\frac{\pi}{2}\times$R (R is bend radius). Since propagation loss/mm in these straight waveguides were evaluated to be 0.62 dB/mm from Fig. 5.7, the coefficient B1 was expected to be $\frac{\pi}{2}\times$ B coefficient in Fig. 5.7. The value obtained was larger than expected and this was attributed to the fabrication differences in each devices. With increasing bend radii, waveguides have longer propagation length and lesser degree of bend. These factors reduce the radiation loss in these bend waveguides, while propagation losses increase. As the bend radii were not within the limit for considerable losses, the magnitude of the total loss was mainly goverened by propagation losses in these waveguides.

This can be clearly observed by comparing total losses from straight and larger bend radius waveguides. The coefficient B2 in Fig. 5.8 provides the radiation losses in these waveguides which were observed to be very low. Thus in our waveguide design, propagation losses dominate. A bend loss of 0.81 dB/90° bend for the smallest bend radius, 1.75 mm was evaluated. Even with present loss values the waveguides were comparable with other currently available waveguide technologies [120].

Even though losses in photo-oxidation modified NP polymer waveguides were comparable with current technologies, fabrication uncertainities in individual devices was noticed to be larger than expected. The uncertainity was mainly due to the uncollimated polychromatic (300-400 nm) UV source used for modifying the devices. The source spectrum is shown in Fig. 5.9a. The uncollimated source contributes to surfaces roughness in waveguides. In addition, the broadness of the source peak contributes to the non uniform depths in the waveguides. Fig. 5.9c shows the cross section observed in photo-oxidation modified NP polymer. The image was taken as the devices were infiltrated with a NaOH solution of 5% solids in DI water. NaOH infiltrated regions give better contrast in microscope images so UV modified regions can be clearly distinguished by this method. The figure clearly indicates that compared to the back surface the surface facing the source was modified more. This was mainly due to UV absorption of unmodified and modified NP polymers (as shown in Fig. 5.10a). The penetration depth of different wavelengths of light in NP polymer is also shown in Fig. 5.10b. Penetration depth is the depth of the material at which the intensity of light hitting the surface gets reduced by a factor of e (Euler's number) [121]. In the range 300-400 nm, NP polymer absorbance reduces with increased wavelength, hence longer wavelengths penetrate the polymer more. So the surface facing the light source was mainly modified by lower wavelengths and their penetration reduced across the thickness of the polymer offering lesser modification. After 24 h of exposure to UV, NP polymer samples showed an increased absorption in the visible range mostly close to UV-blue regions. This also imparts a slight yellowish colour to the sample which makes them unsuitable for optical measurements in the entire visible range.

To improve the fabrication technique and losses, a collimated high power source from Newport was used. The spectral emission of the source in the UV range is also shown in Fig. 5.9b. Unfortunately, exposures of the NP polymer in the presence of oxygen with the newer source did not provide similar results as in the polychromatic source. Fig. 5.9d shows cross section images with NaOH infiltrated waveguides. The modified regions were very hazy compared to previous transparent samples. In addition, the hydroxyl and carboxyl concentration gradient as observed in Fig. 5.9c was also missing. As the modifying UV irradiation wavelength for both sources varied a lot, the photo-oxidaition in the NP polymer was not repeatable. From stud-

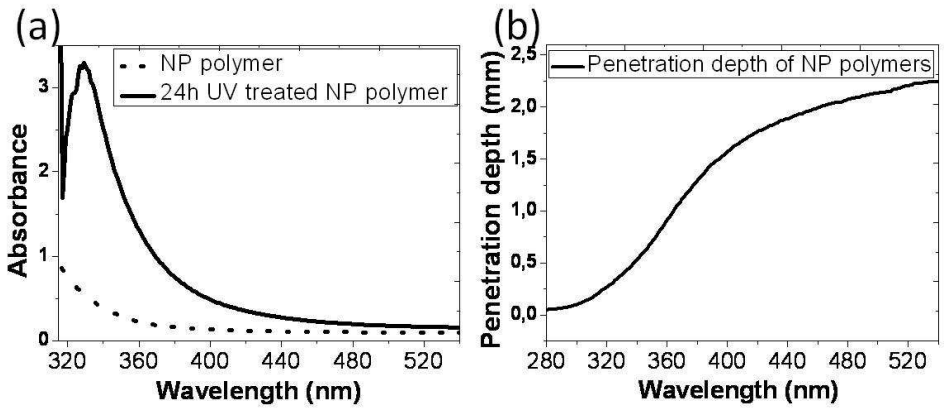

***Figure 5.10**: (a) UV-Visible absorption spectra of NP 1,2 PB polymers before and after photooxidation for 24 h; (b) Penetration depth of radiation ranging from 300-550 nm across a 500 µm thick NP polymer sample [112].*

ies of Sagar et al. [112] it was observed that the photo-oxidation induced in these NP polymers was attributed to UV intensity in the range 300-350 nm. In the newer source, the intensity of these wavelengths were too low to produce efficient modification. Hence the modification technique using photo-oxidaiton had to be replaced by other options. The new approach opted to modify the surfaces was inspired from works of collaborators Berthold and Sagar et al. [100].

5.2 Thiol-ene click chemistry modified waveguides

To improve losses in NP SLCW another surface modification method was used. Thiol-ene click chemistry was used to modify the air-polymer interface and thus induce hydrophilicity in NP polymers. This section deals with the thiol-ene click chemistry employed in the LiCorT project.

In the LicorT project, some of the NP polymer fabrication techniques were improved with the help of co-workers. The solvent casting method was modified to make uniform thick NP polymers. In the new fabrication, thin (100 μm) NP polymer sheets were formed by making a sandwich between two single side polished silicon wafers of 10 cm diameter. Unlike solvent casting in a petri dish, this technique reduced cracking of the NP polymer sheets. The silicon wafers were coated with low surface energy fluorinated organosilane molecule using Molecular Vapor Deposition (MVD). The PB-PDMS diblock was mixed with cross linker and solvent casted on these polished silicon wafers. This was then vacuum dried for 7 h and pressed onto another polished wafer with steel spacers of 100 μm. The spacer determined

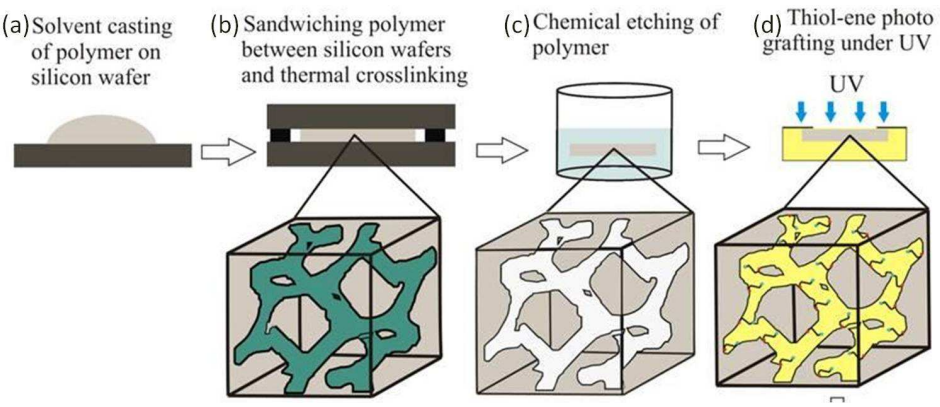

***Figure 5.11**: New fabrication technique for thin and uniform NP polymer waveguides. (a) The solvent casting step is carried out on fluorinated silicon wafers; (b) sandwiching between wafers with spacer ensures uniform polymer film thickness; (c) crosslinked thin film/sheet of polymer is chemically etched using etchant TBAF; (d) thiol-ene photografting under UV source. The sample is then washed and dried [117].*

the thickness of the polymer. The sandwich was pressed together under vacuum in a specially designed pneumatic compression press for 30 min at 4 bars [117]. Similar fabrication steps as in Chapter 4 were used in cross linking and etching the NP polymer. The new fabrication technique is schematically represented in Fig. 5.11.

The different thiols used to modify the air-polymer surface were MSA and MESNA (Chapter 4). On attaching thiols to the surface, hydrophilicity was induced as MSA have two terminal carboxylic groups and MESNA have a sulphonated salt end. Benzophenone (BP) was used as the PI initially. As 2-dimehoxy-2-phenyl acetophenone (DMPA) gave more efficient results and reduced colouring of samples, BP was replaced with DMPA in the later stage of the project. The degree of thiol reaction using water uptake techniques was studied by collaborators [117]. Contrast curve was used to monitor the transition of NP polymer from hydrophobic film to hydrophilic. This method gave a reasonable idea of the exposure time required for MSA and MESNA thiols to produce hydrophilicity in NP polymers.

To verify hydrophilicity induced due to grafting of thiol groups onto the polymer, contact angle measurements were performed on MSA and MESNA samples. Fig. 5.12 gives the contact angle measured for untreated hydrophobic, MSA treated and MESNA treated NP polymer samples. A 1 μl droplet of DI water was placed on the NP polymer surface. The CA was recorded 10 s after the droplet was deposited on the surface. The exposure time used for treating NP polymers with MSA and MESNA were 30 min and 4 min respectively. Contact angle values of 35 $\pm 2^{\circ}$ and 24 $\pm 2^{\circ}$ was measured in

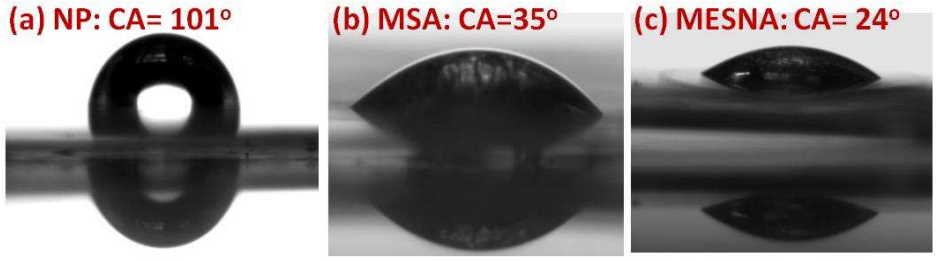

***Figure 5.12**: Contact angle meaurement for (a) untreated NP polymer; (b) MSA treated NP polymer; and (c) MESNA treated NP polymer. The values were measured 10 s after 1 μl droplet of water was placed on the NP polymer surface [100].*

MSA and MESNA treated samples. This clearly indicated surface wetting compared to hydrophobic NP polymers (101 $\pm 3°$). Note that the CA values obtained for NP polymer samples used in photooxidation modified waveguides were 66°. The increased hydrophobicity in the newly fabricated samples were attributed to the modifications made in fabrication technique. In the previous fabrication technique, the starting material was solvent casted in a petri dish. The casted polymers upper and lower surfaces were subjected to different surface tensions as one surface faced the glass of the petri dish and the other faced air (lower surface tension side). Due to high surface tension in the glass, the polymer surface towards petri dish developed a thin ($\approx$ 2-10 nm) layer of PB called a skin layer. The skin layer did not have a uniform thickness and, one could expect it to contain cracks within. The skin layer was not seen on the low surface tension side. In new fabrication techniques, sandwiching between two MVD coated wafers offered very high surface tension to both sides of the polymer. This ensured uniform skin layer on both sides of the polymer offering a highly hydrophobic surface. The two different CA measured in untreated NP polymers was due to evenly distributed skin layers in the newly fabricated thin NP polymers.

FTIR measurements of MSA and MESNA treated samples were taken and compared with untreated NP polymers (Fig. 5.13). The C=C peak at 904 cm^{-1} was reduced when the NP polymers were treated with MSA and MESNA, indicating consumption of the vinyl unsaturation. There were some additional peaks developed at 1710 cm^{-1} due to carbonyl groups in MSA and at 1050 cm^{-1} and 1220 cm^{-1} due to S=O (symmetric and antisymmetric stretching in MESNA treated NP polymers).

5.2.1 MSA grafted waveguides

100 μm$\times$100 μm waveguides were patterned on NP polymer using MSA thiol grafting. A photolithography mask as shown in Fig. 5.14c: inset was

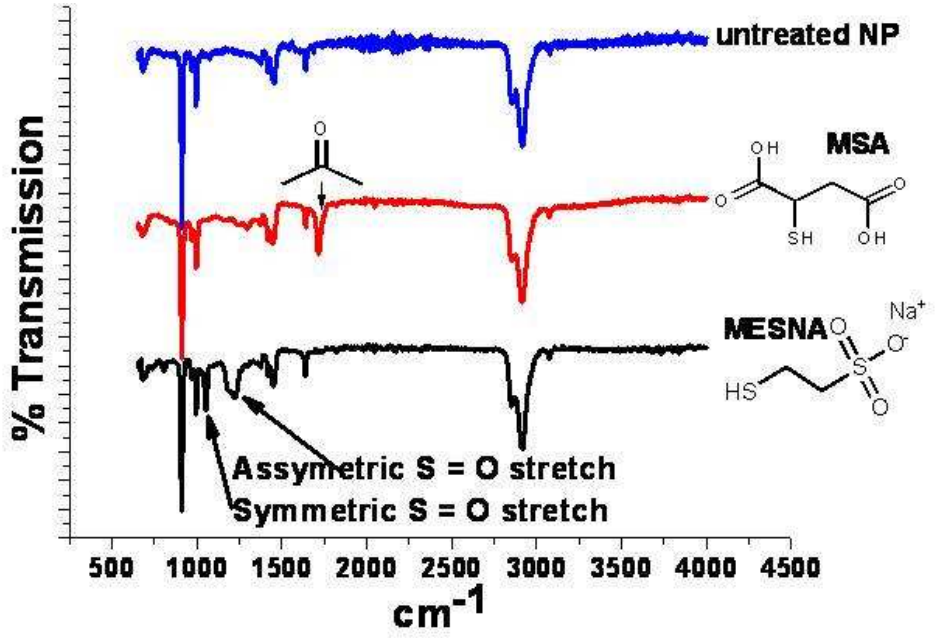

***Figure 5.13**: FTIR meaurement for (a) untreated NP polymer; (b) MSA treated NP polymer; and (c) MESNA treated NP polymer [100].*

used to make bend waveguides of bend radius, R = 3 mm, sandwiched between straight waveguide sections of length ranging from 2 mm to 16 mm. The waveguide devices were immersed in DI water for 10 min. Waveguide devices were characterized by measuring their propagation losses. Like in photo-oxidation modified waveguides, the substitution technique was used to measure the propagation losses. Some setup modifications were introduced to increase ease of device handling and reduce device losses. The device was sandwiched between two 100 μm thick fluorinated ethylene propylene (FEP) sheets of low refractive index (n=1.38). The polymer stack was then sandwiched between 5 mm thick polycarbonate blocks. Such a sandwich design was used to make the handling of thin NP polymer sheets easier. In addition to mechanical support, FEP polymers reduced the index contrast between the infiltrated polymer and clad in the y axis (Fig. 5.14b).

The modified experimental setup is schematically illustrated in Fig. 5.14a and a camera image is also showed in Fig. 5.14d. A He-Ne laser (632 nm) was butt coupled onto the waveguide using 62.5/125 μm MM fiber. The fiber with similar dimension as the waveguide was used. A 400 μm core MM fiber was used to guide light out of the waveguide into a photodiode from *Ophir Electronics*, PD 300. A large core output fiber was used to collect all the light coming out of the waveguide. This improvement in the setup was used to reduce the coupling losses due to fiber waveguide

alignment in the measurement. The laser light was split into two beams using a polarization insensitive beam splitter (*Thorlabs Inc*). One of the beams were coupled onto a photodiode (*Ophir Electronics*, PD 300) for reference and the other launched onto an MM input fiber for coupling into the device. The reference signal was used to monitor fluctuations in the laser source during measurements. The split ratio of the beam was determined at every measurement to reduce calculation errors. A microscope was mounted vertically above the setup, to assist with alignment of insertion and collection optics. The I_{in} (Fig. 5.14b) in each waveguide was determined from the I_{ref} and split ratio. Propagation loss was evaluated by plotting total Loss, L in dB from each waveguide as a function of propagation length. A linear fit to the data provides the propagation losses per millimeter. A propagation loss of 0.26 ± 0.01 dB/mm was evaluated in these waveguides. The waveguides developed had lower loss compared to photo-oxidaiton modified waveguides.

Drying in water infiltrated MSA devices was studied. A wet NP device was mounted in the setup with light coupled in and out of one of the waveguides. This was aligned such that the maximum intensity was recorded from the photodiode. As shown in Fig. 5.15, 10 min after the measurement was started, the device dried and the intensity at the ouput dropped (no more guiding in the waveguides). 15 min after the measurement, water was added to the device from the sides, also shown in Fig. 5.15. The intensity measured was higher than previous values. This is likely due to the formation of an index matching water layer between input fiber and the waveguide. The value gradually drops but was recovered by realigning the fiber. 1 h after realignment, the intensity drops to very low values. As realigning did not improve the value, this was confirmed to be a case of drying in the devices. Water was added and the larger intensity values returned.

5.2.2 MESNA grafted waveguides

To characterize the MESNA grafted waveguides, similar propagation loss measurements as in previous cases were used. Fig. 5.16 shows the measured propagation loss in MESNA grafted waveguides. A propagation loss of 0.54 ± 0.5 dB/mm and a coupling loss of 2.5 ± 0.5 dB was measured in these waveguides.

To summarize, three different techniques developed for modifying the NP polymer surfaces were characterized. Contact angle measurements and FTIR spectroscopy was used to evaluate the water infiltration and water uptake in the modified polymers. Propagation loss measurements were used to characterize the waveguides. A propagation loss of 0.62 ± 0.3 dB/mm, 0.26 ± 0.5 dB/mm and 0.54 ± 0.5 dB/mm was observed from photo-

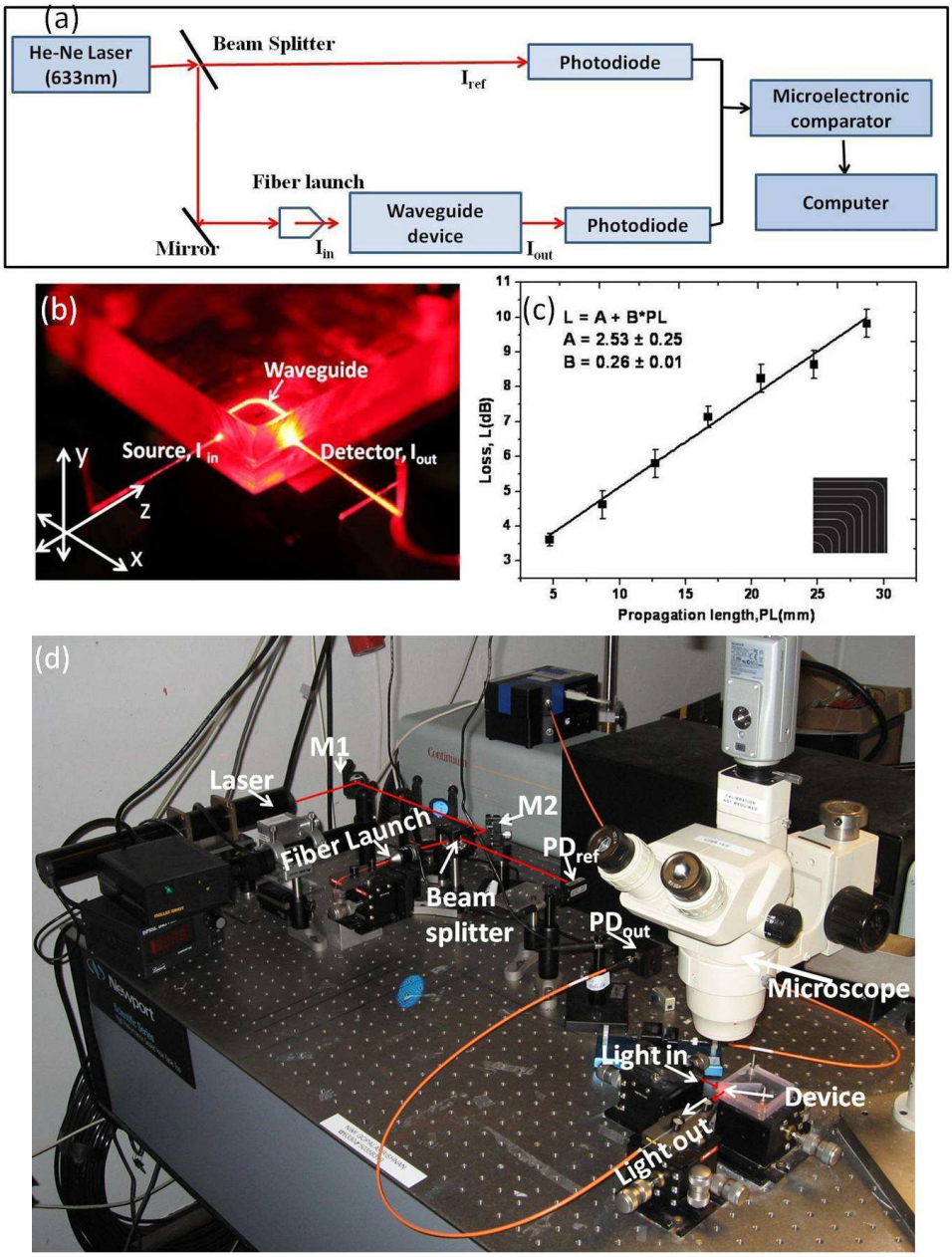

***Figure 5.14**: Propagation loss measurements in MSA grafted waveguides(a) Schematic illustration of the experimental setup of propagation loss measurement; (b) a close up view on the setup at the waveguide device; (c) loss measured in each waveguide as a function of propagation length; (inset) UV lithography mask design; (d) Image of experimental setup used.*

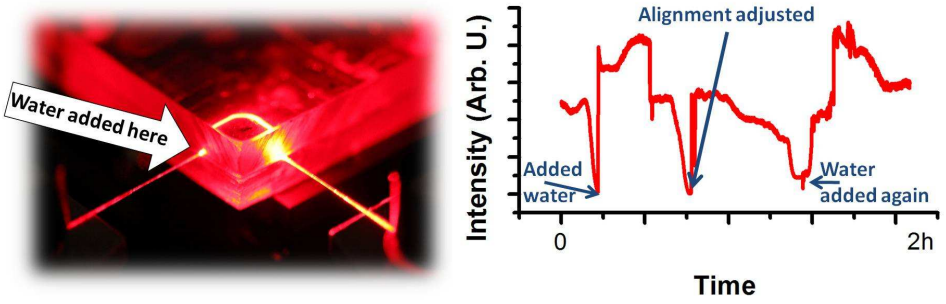

Figure 5.15: *Water drying measurement in MSA modified NP polymers. The water added site is also shown in the figure.*

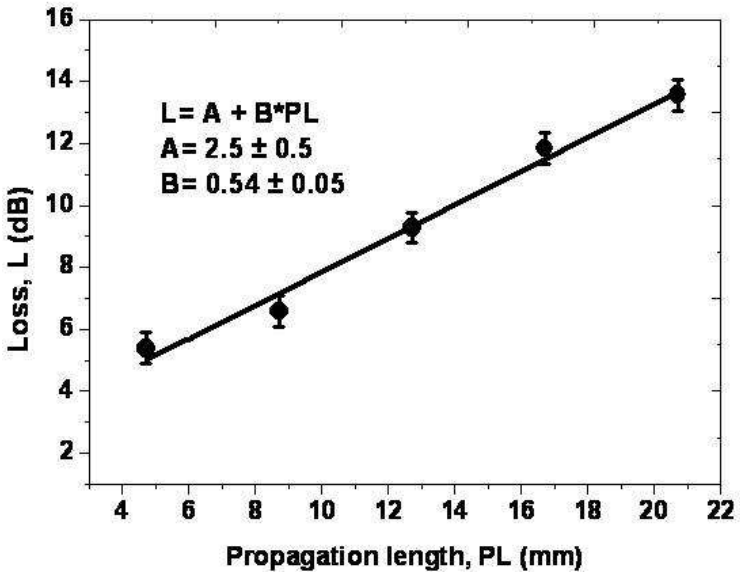

Figure 5.16: *Propagation loss measurements in MESNA grafted waveguides. Loss measured in each waveguide as a function of propagation length.*

Comparison	**Photooxidation**	**MSA**	**MESNA**
UV exposure time	24h	30min	4min
CA	56°	35°	34°
FTIR peaks	3100-3670cm^{-1}, 1710 cm^{-1}	1710 cm^{-1}	1050cm^{-1}, 1220cm^{-1}
Total processing time	24h	2.5h	2h
PL (dB/mm)	0.62±0.03	0.26±0.05	0.54±0.05

***Table 5.1**: Comparison of results attained in the three different surface modification techniques used in this study.*

oxidation modified, MSA and MESNA grafted waveguides respectively. Table 5.1 compares the results obtained in the three methods. The contact angle measured at 1 min after the droplet was placed on the photooxidation modified surface was used to compare with results from 10 s measurements.

Chapter 6

Applications of SLCW

This chapter introduces some optofluidic applications of the NP SLCW platform. The section explains how the SLCW waveguides can be used as a size based nanofilter. Different analytical techniques and their results are given. The chapter is concluded with references to other feasible applications of the technology and a summary.

6.1 Nanofiltering in NP SLCW

Optical properties of fluids are exploited to extract valid information in many fields of science like physics, chemistry and biology. To give some examples, water quality measurements, waste water treatment [122, 123], disease detection [124, 125] and in general food sector [126] and process industries all exploit optical propeties of liquids to access information. Low volumes of samples and reagents, longer interation lengths between fluid and optical fields, inexpensive detection techniques, shorter sampling times make LCW technology a suitable candidate for these kinds of applications. One of the traditional method to monitor liquids is to measure their transmittance using a spectrometer. But in turbid liquids [127] like blood or milk, multiple scattering centers can cause erroneous interpretation of the data. Thus to control the optical properties of the turbid solutions, large scatteing particles are seperated from the solution. Centrifugation or filtering is the most adapted and known techniques in the field. However, integrating a centrifuge system onto an optofluidic platform is difficult to be realised. Thus, filtering via membranes can be adopted for optofluidic systems. Silicon, ceramic or inorganic materials are usually used as size based filtration

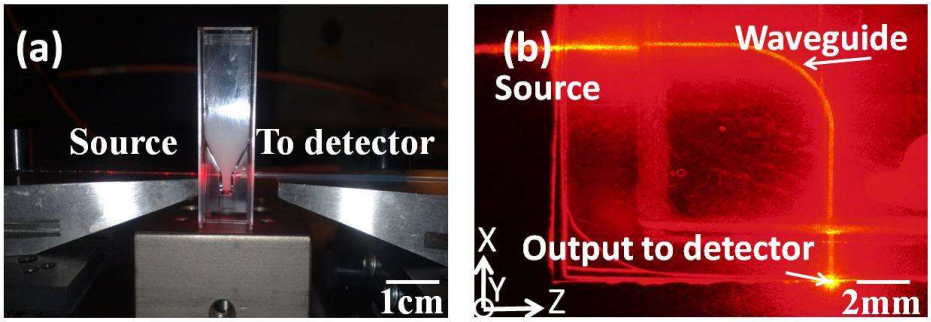

***Figure 6.1**: Experimental setup for measuring propagation loss of red light (633 nm) in milk with 0.5% fat (a) in cuvette; and (b) in NP LCW. Scattering from large fatty particles make it difficult to tranmit light through milk with 0.5% fat in cuvette while filtered milk solution transmits and guides light efficiently in NP LCW.*

membranes [128, 129, 130, 131]. Compared to the conventional filtration membranes, polymer based filters are shown to be more robust [132, 133], although there are numerous challenges that restrict their integration in lab on a chip systems. Clogging of polymer filtering membranes is a significant issue which is avoided by using thin films of order $\approx 1\mu$m. Yet these aggravate fabrication complications for small scale integration requiring additional mechanical support. Furthermore, filtering membranes are governed by the principles of diffusion (under pressure changes much smaller than in cases of reverse osmosis) resulting in unfavourably longer detection times [134]. All these challenges restrict integration of polymer filtering membranee onto lab-on-a-chip devices.

The developed NP SLCWs (thiol-ene modified devices are used) guide light when the nanopores of the exposed region were filled with water/aqueous solution. The optical behaviour of guided light can be used to abstract information about the core region and thus about the infiltrated solution [135, 136]. As such, an optofluidic sensor can be developed using these NP SLCWs. The size of the nanopore in the polymer matrix was $\approx$ 14 nm [99]. Owing to this nano sized porosity, larger particles dissolved in the infiltrating aqueous solution are kept away from entering the nanopores. This property of NP SLCW was exploited to develop a nanofiltering LCW without additional processing steps. As the infiltration in these waveguides were governed by capillary forces [137], unlike available filtration membranes, these NP SLCWs can offer significantly reduced processing and detection time.

To examine whether these NP polymer LCWs can be employed to study turbid liquids, milk with 0.5% fat was used. For turbid solutions like milk, a standard cuvette transmittance measurement exhibits low throughput as

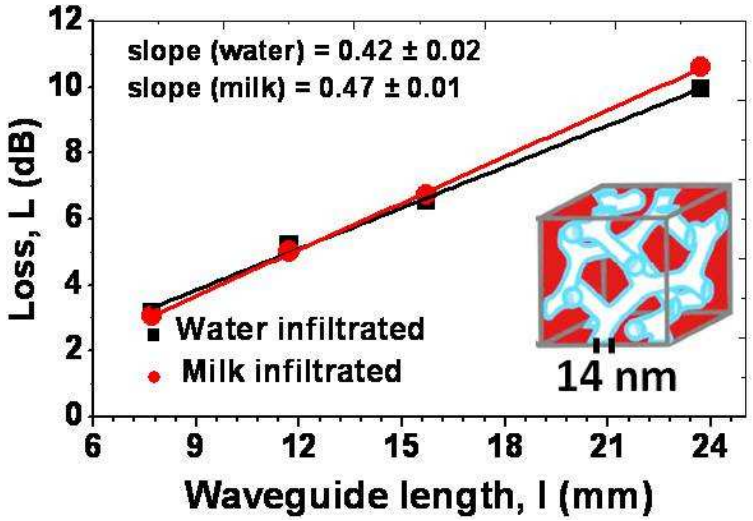

Figure 6.2: *Propagation loss measurements in water and milk infiltrated NP polymer waveguides.*

the light is either absorbed or scattered by the large particles (Fig. 6.1a). However, milk infiltrated NP polymer waveguides were able to guide red light (Fig. 6.1b). Compared to a loss of 10.6 dB/mm in cuvettes, 633 nm He-Ne laser butt coupled onto the waveguide was subjected to only a loss of only 0.05 dB/mm. Fig. 6.2 shows loss measurements in water and milk infiltrated NP SLCWs (ref Chapter 5 for propagation loss calculations). Propagation losses measured from water infiltrated devices vary only slightly from milk infiltrated devices. This was attributed to low milk absorption at 633 nm.

6.2 Proof of filtering

The concept of filtering was demonstrated using two fluorophores of different sizes and fluorescence, mixed in an aqueous solution. The choice of suitable fluorophores for demonstrating filtering was made based on their fluorescence spectra and size. As the pores are nano sized, micrometer sized fluorophores were expected to be excluded from entering the polymer. Align Flow- flow cytometry alignment beads of 2.5 μm from *Invitrogen* (Cat.No.A14835) were used as the large fluorophore. From infiltration measurements (Chapter 5 Proof of concept) it was known that rhodamine 6G molecules enter the nanopores. Thus nanometer sized fluorophore chosen was Rhodamine 6G perchlorate from *Sigma Aldrich* (252441-1G) and a stock solution of 1.8 mM in ethanol was made. The fluorescent rhodamine dye fluoresces at 560±10 nm when excited using green light (532 nm), and do not fluoresce under red (655 nm) excitation. The beads selected for

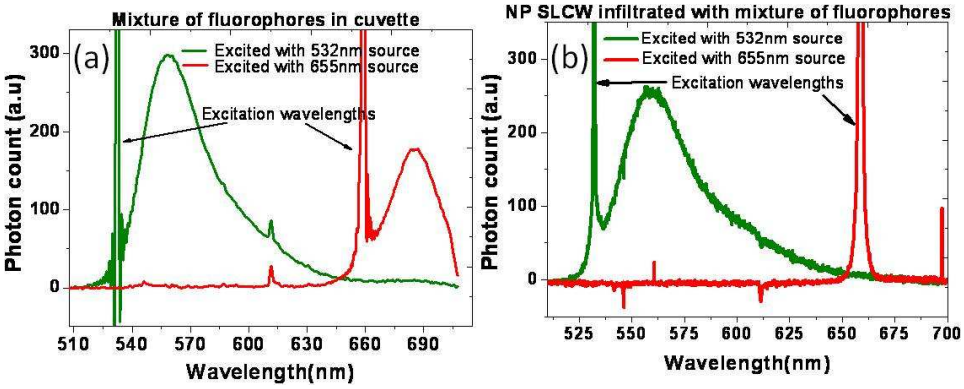

***Figure 6.3**: Fluorescence spectra of mixture of Rhodamine 6G and 2.5 μm beads when excited with green and red lights. (a) Spectra in cuvette; (b) spectra in infiltrated device.*

the experiment have excitation at 630-660 nm and emission at 670-720 nm. Therefore, the fluorophores chosen were easily distinguishable from their fluorescence emission. Hence, presence of one of these fluorophores in 1,2-PB nanoporous polymer can be determined from their fluorescence spectra. A solution of 0.25% solids beads and 0.92 μM concentration of rhodamine dye was made by diluting the respective stock solutions in DI water. Fluorescent spectra of the mixture in cuvette was recorded using a spectrometer (*Ocean Optics* HR 2000) on excitation with red (655 nm) and green (532 nm) laser light (shown in Fig. 6.3a). 15 mW diode pumped solid state green laser was used for the purpose. The collection optics in the setup (similar to propagation loss measurement for photo-oxidation modified devices Chapter 5) were kept 90° to the incident source to avoid spectrometer saturation (also ref Fig. 6.1a).

A waveguide of dimensions 500 μm×500 μm×10 mm was made using photo oxidation induced modification (Chapter 4) in NP polymers. The NP polymer was immersed in the mixture solution for 30 min. The polymer was removed and its surface was cleaned using DI water. The waveguides were excited from above and the collection optics were placed at the end of the waveguide. Such an experimental setup was adapted because of waveguiding restrictions in the photo-oxidation modified NP polymers. Under green and red excitation it was observed that NP polymers immersed in mixture of beads and rhodamine provided fluorescence signal only in green excitation. This verifies the absence of 2.5 μm beads in the waveguides (Fig. 6.3b).

With better performing thiol-ene modified NP polymers, the filtering results were repeated. Instead of using fluorophores with highly differing sizes, fluorophores of sizes comparable to the size of nanopore were used. Unfortunately, fluorescence spectra of the chosen fluorophores were not dis-

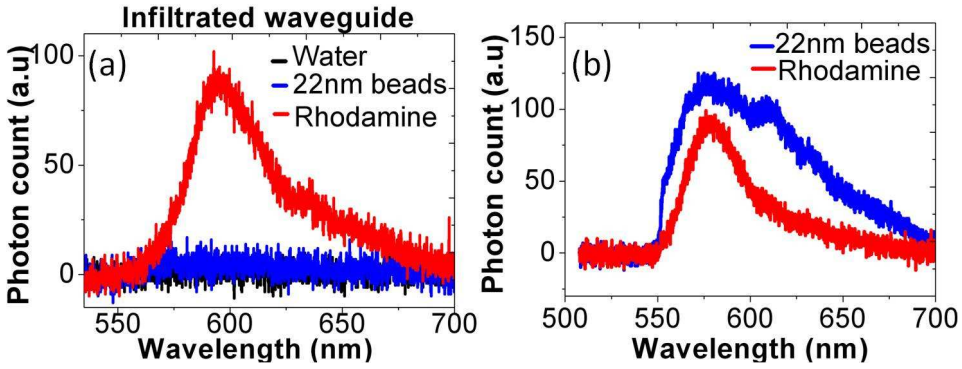

***Figure 6.4**: Fluorescence spectra of fluorophores infiltrating the waveguide device (a) Spectra obtained from waveguide devices immersed in Rhodamine B, 22 nm beads and water; (b) fluorescence spectra of the fluorophores observed in a cuvette for reference.*

tinguishable as in the previous case. Fluorescing organic dye, Rhodamine B (≈10 Å) [138, 139, 140] and 22 nm red fluorescing polystyrene beads (*Duke scientific*) were used for the purpose. Unlike Rhodamine 6G, Rhodamine B can be more efficiently diluted in water. Both fluorophores fluoresces under green (532 nm) excitation and have specific fluorescence spectra as shown in Fig. 6.4b, determined from cuvette measurements. Solutions of 2.14 μM Rhodamine B and 1% solids 22 nm red fluorescing beads were prepared in DI water. The choice of fluorophore concentration was made by measuring their fluorescence signal in cuvettes. Concentrations with comparable fluorescence signals were adopted. A source of 532 nm coupled onto a 62.5/125 μm core MM fiber was used to excite fluorescent solutions of Rhodamine B and 22 nm beads in a cuvette with sample volume 100 μl and propagation length 10 mm. The collected spectra from the cuvette was coupled onto a spectrometer using a 400 μm core MM fiber. A long pass filter (FEL0550 from *Thorlabs Inc*) at the laser wavelength was used to avoid spectrometer saturation.

Waveguides of dimension 100 μm × 100 μm were defined in NP polymers by UV assisted thiol-ene click chemistry. Two different waveguide devices were immersed in the prepared Rhodamine B and 22 nm bead solutions seperately for 30 min (to ensure complete loading). The incident and collection optics used in the experimental setup was similar to that of the cuvette measurement. The fluorescence emmision from the excited waveguides are shown in Fig. 6.4a. Water infiltrated waveguides have no specific fluorescence emission under green excitation, while Rhodamine dye infiltrated waveguides show fluorescence signals at 590 nm, giving a clear indication of Rhodamine presence in the nanopores. On the other hand, devices immersed in 22 nm red fluorescing beads have no significant fluorescence signal in the waveg-

uides.

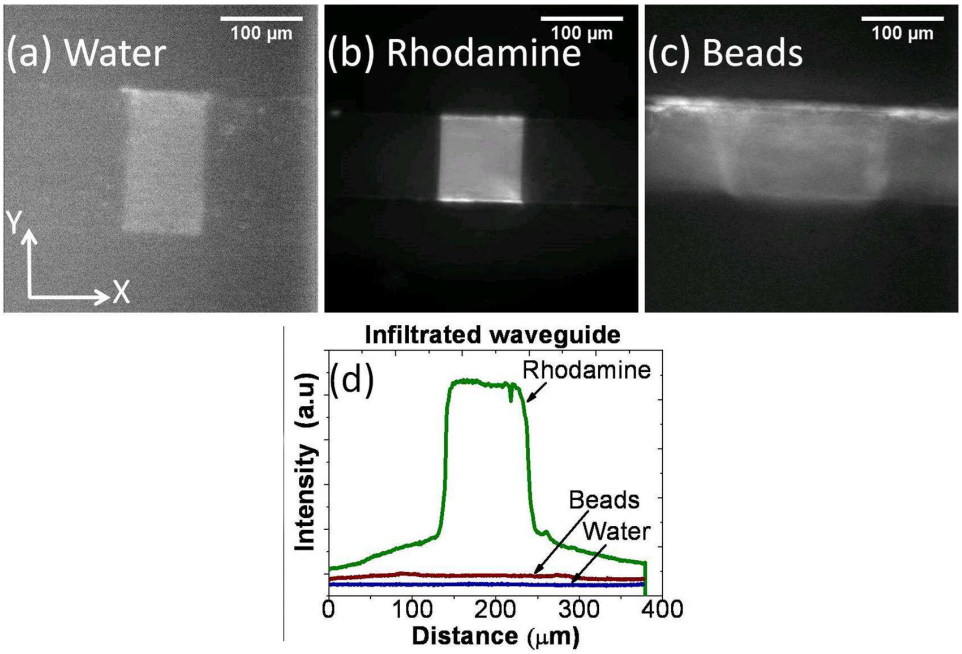

Figure 6.5*: Fluorescence images (a) of water infiltrated device; (b) of Rhodamine B infiltrated device; (c) waveguides immersed in 22 nm bead solution; (d) fluorescencce signal profile across the waveguide device in the X-axis.*

6.2.1 Fluorescence imaging of NP polymers

Fluorescence imaging of NP polymers was performed to confirm that the fluorescence signal obtained from Rhodamine B infiltrated waveguides was from the entire volume of the waveguide and not exclusively from the surfaces [141]. Fluorescence microscopy [142] can be used to detect even very small fluorescence signals from the fluorophores. Cross sections of the devices immersed in Rhodamine B and 22 nm fluorescing beads solutions and water were compared using fluorescence microscopy. In an inverted fluorescence microscope (*Nikon* ECLIPSE TE 2000, filter set G2E/C), an excitation filter ensures a narrow band green excitation (540 $\pm$ 10 nm) which is reflected using a dichroic mirror (reflects below 560 nm) and focused onto the waveguide cross section using a 20 $\times$ magnifying water immersion microscope objective (filter set G2E/C). Emitted fluorescence signal is collected and transmitted through the dichroic and emission filter (560-650 nm) onto a CCD camera (Cascade II, 512, *Roper Scientific INC, Photometrics*).

A java based image processing program *Image J* was used to analyse the fluorescence images from the waveguides. Fig. 6.5a, b and c shows the flu-

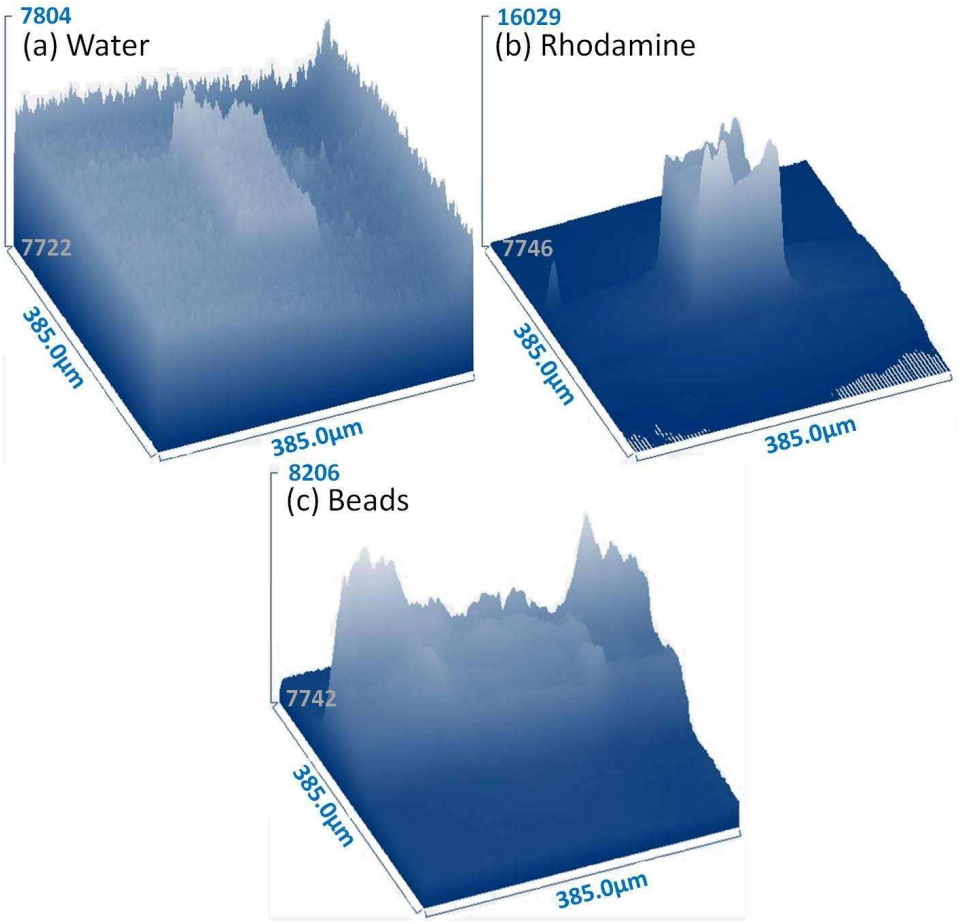

***Figure 6.6**: Surface profile of the images (a) of water infiltrated device; (b) of Rhodamine B infiltrated device; (c) of devices immersed in 22 nm bead solution.*

orescence images of devices immersed in water, Rhodamine B and 22 nm beads solutions. In all three images the core region of the waveguide gives higher signal than the cladding region. The is attributed to the autofluorescence and waveguiding properties of the NP polymers. Even though the contrast in these images show some fluorescence signal, an intensity profile or a gray value scan across the device clearly confirms that these signals can be neglected (Fig. 6.5d). Only in Rhodamine infiltrated waveguides were the signals strong enough to be assumed as fluorescence. The fluorescence intensity profile across the device confirms uniform distribution of rhodamine through out the waveguide volume. In addition, it also proves the confinement of Rhodamine only to the exposed region [143].

To examine whether fluorophores were thouroughly washed and do not stick to the upper and lower surfaces of the NP polymer, a surface plot of the entire

image was taken. A surface plot displays three dimensional graph of the intensities of pixels in a grayscale. The surface plot of the 3 devices immersed in the different solutions are shown in Fig. 6.6. In Rhodamine infiltrated devices, the intensity at the upper and lower surface of the NP polymer was observed to be slightly higher than intensity from the waveguide. This was assumed to be due to sticking of the dye onto the polymer surface. For devices immersed in 22 nm beads, at one surface signal was higher and lay outside the waveguiding region. This was assumed to be due to background signals from the unfocused sites in the polymer cross section. The cross section of the waveguide was taken by dicing the polymer waveguide using normal razor blades, which may have caused uneven surfaces at the cross section. As images were taken focusing onto a single plane in the device cross section, signals from the upper and lower planes add to the background noise. The slight increase in signal from devices immersed in 22 nm beads solutions were assumed to be from such a situation. In water infiltrated devices, no significant intensity variations were observed.

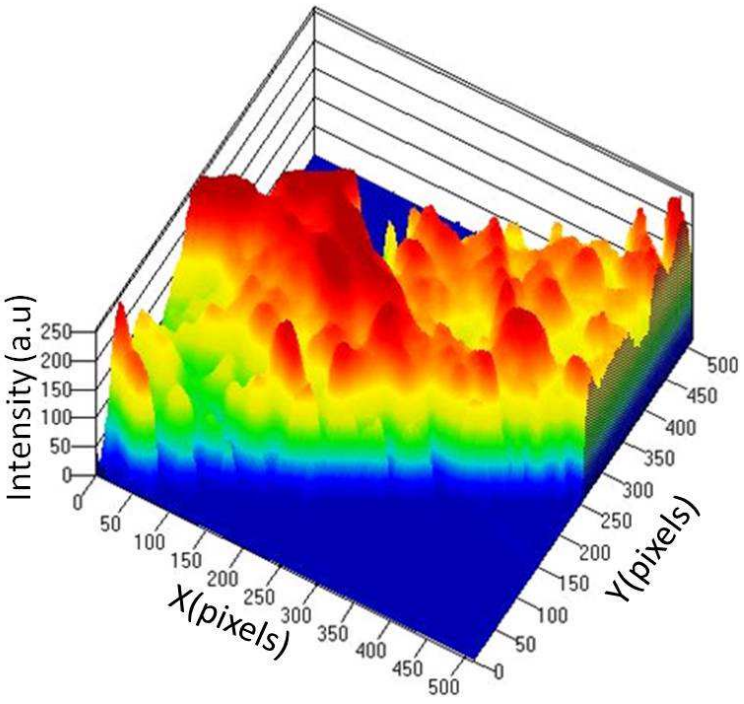

***Figure 6.7**: Confocal images of Rhodamine B infiltrated devices.*

Confocal microscopy was used to increase optical resolution of the images. Unlike conventional fluorescence microscopy, where all parts of the sample in the light path are excited increasing background noise, pin-hole based focusing in confocal microscopy reduces out of focus signal and thus improves

the signal to noise ratio. Fig. 6.7 shows the confocal images of Rhodamine infiltrated devices. The image was taken half way through polymer bulk. The colour (rainbow) variation represents the intensity of the dye within the region.

6.3 Absorption measurements in NP SLCW

Absorption spectroscopy is one of the most widespread and sought after tools for quantitative analysis to determine the concentrations of various chemicals or biological analytes. The concept was developed based on the fact that compounds absorb certain visible wavelengths efficiently while some are transmitted. The absorbance of certain wavelengths in a medium can be quantified using Lambert Beer law. It states that transmittance of light though a sample logarithmically depends on the absorption coefficient, α, of the absorbing species and the distance (l) travelled by light in the medium.

$$T = \frac{I}{I_0} = 10^{\alpha l} = 10^{\varepsilon l c} \tag{6.1}$$

where the absorption coefficient is product of molar absorptivity, ϵ (extinction coefficient) and c, concentration of the absorber species. I_0 and I is the intensity of the input and output light in the medium respectively. The transmittance of liquids can be expressed in absorbance as

$$A = -log_{10}\left(\frac{I}{I_0}\right) = \varepsilon l c. \tag{6.2}$$

Thus absorbance of a medium for a fixed path length will linearly vary with concentration of the absorber (ref Chapter 3). Many label free optical detection schemes are based on this theory.

NP SLCWs form an efficient LCW and nanofilter [144, 145]. To study whether NP based LCW platform can be used as an efficient optofluidic device for absorption based optical detection, devices were infiltrated with absorber species. A stock solution of 1.8 mM Rhodamine B was diluted to 1.07, 2.14, 3.21, 4.28 and 12.85 μM concentrations with DI water [146]. Absorbance of different concentrations of Rhodamine dye at excitation wavelength 532nm was measured in a 10 mm long disposable cuvette. A similar experimental setup as in previous measurements was used. Absorbance was expected to be linearly dependent on Rhodamine concentration. The slope of linear fit in Fig. 6.8 gives the constant of proportion in Lamberts Beer relation. The slope obtained was 0.0862 and the expected value was 0.0864 as ϵ of Rhodamine at 533 nm is 86471 cm^{-1} M^{-1} [147]. To test whether NP SLCW can be used as a label free optical sensor, Rhodamine dye was

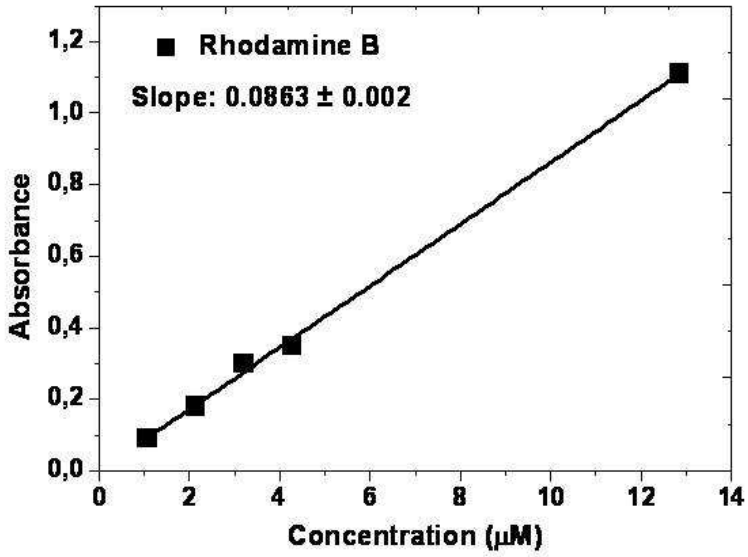

***Figure 6.8**: Lamberts Beer relation evaluated for Rhodamine B in a cuvette of propagation length 10 mm.*

infiltrated into the nanopores. If the optical field within the waveguide efficiently interacts with the absorber dye, Lamberts Beer relation could be obtained in dye infiltrated devices. Propagation loss in each device was expected to increase as a linear function of the dye concentration.

Absorbance in NP polymers were measured in terms of propagation loss changes occuring in the device when infiltrated with the dye. Owing to manufacturing difference i.e. difference in number of grafted functional groups at the nanopores, propagation loss measured in the waveguide devices vary among devices. Therefore, absorbance for different Rhodamine B concentrations were measured seperately in different devices. Propagation loss for different NP waveguide devices were measured by infiltrating with water. Fig. 6.9a shows propagation loss evaluated for 3 different devices. Note that the propagation loss varies among devices and the measured value was expected to vary by a value 0.05 dB/mm among devices. Separate devices were filled with different concentrations of Rhodamine B. With an absorber species in the nanopores, the propagation loss in each device was expected to increase and should be a function of the concentration of absorber species within the pores. Fig. 6.9b shows the results obtained from cuvette and NP polymer waveguide devices.

The results obtained were not consistent with cuvette measurements. Unlike in cuvettes, where the propagation loss for a unit length of propagation increased with concentration, in NP polymer devices the measurements were erroneous. The concentration series chosen might be too low to be detected

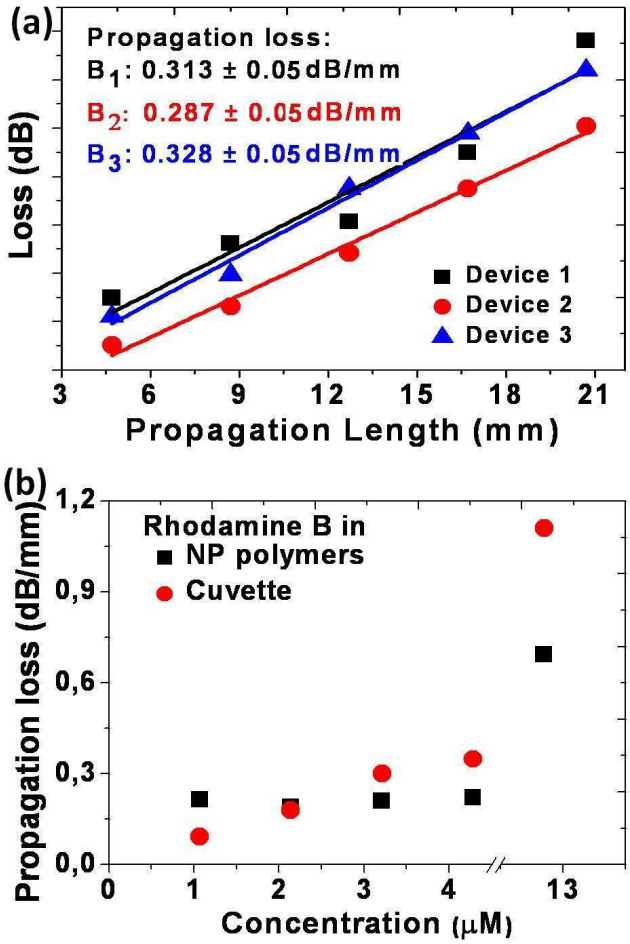

***Figure 6.9**: (a) Propagation loss measurements in different NP waveguide devices; (b) additional loss introduced by the absorbing dye. With concentration, the loss per mm of light propagation should increase, confirmed by cuvette measurements.*

by the devices. The least observed propagation loss in these MSA modified devices, when infiltrated with water, were 0.28 dB/mm. As such, the concentration of Rhodamine that absorbs within this limiting factor will not be detected by the devices. Values at the lower end of the concentration series almost lie in this range so mostly concentration above 5 μM might be detected. This was assumed and further experiments in this regard are yet to be carried out.

Quantifying the chemistry volumes, improved manufacturing and greater understanding of the grafted thiol group on the polymer-air interface etc. would help to reduce the propagation loss measurement errors. Since the NP polymer devices were aimed at being used as one time use devices,

some improvements for reducing device to device value difference should be considered.

This chapter thus gives one of the optofluidic applications of these NP polymer device. It was demonstrated that NP SLCW can be used efficiently to monitor optical properties of turbid fluids. Unlike in a cuvette measurement where fat particles in milk (turbid solutions) restricts transmittance of light, due to nanofiltering in the NP SLCW, light propagates in milk filled devices allowing long interaction length between liquid and optical field. A propagation loss measurement was carried out and compared for milk in cuvette and NP waveguide devices. The nanofiltering was proved by filling the nanopores with fluorophores of different sizes. 2.5 μm and 22 nm sized fluorescing beads were kept away from entering the nanopores. Rhodamine 6G and Rhodamine B fluorescent dyes were used to observe the infiltration in the nanopores. Uniform infiltration was proved by imaging the infiltrated device cross section using fluorescence microscopy and confocal microscopy. The possibility of implementing label free detection in NP SLCW was also discussed. Though the measurements were not fully successful, some improvements were suggested. If label free detection can be integrated onto these NP SLCW devices, it can be used as a platform, for example to, detect analytes in blood.

Chapter 7

Conclusion

Through this Ph.D project, a platform for liquid core waveguiding was developed from nanoporous coblock polymers. The work consisted of design, fabrication and characterization of the developed LCW with a focus on application in biosensing.

The growing need for fast, efficient and low cost diagnostics has given optofluidic devices an important role in medical field. To enhance the performance of optofluidic devices as sensors, recent application has adapted liquid core waveguiding technologies. When conventional guiding mechanisms were used, the unavailabilty of a suitable cladding material (low index cladding material, index lower than $\approx$1.33) restrict implementation of liquid core guiding in optofluidic devices. A number of approaches to solve this problem have been developed which were briefly discussed in Chapter 2. Moderate optical properties, implementation difficulties, integration on to planar optics, some molecular interactions etc. limit the utility of some of these developed LCW in medical applications. A different approach of developing LCW is suggested and demonstrated in this thesis. Nanoporous polymers developed from coblock polymer assemblies form a very suitable candidate for cladding materials. The effective refractive index of such diblock copolymer self assemblies can be calculated as a weighted average of their individual polymer blocks. By proper designing and synthesis, the polymer materials can be tuned for the right effective refractive index. Compared to the many approaches discussed in Chapter 2, the core of the developed LCW in the project is not completely made of liquid. The core of the nanoporous waveguide is a solid-liquid 'alloy', hence an appropriate acronym for these waveguides would be solid-liquid core waveguides (SLCW). Furthermore, these SLCW can be an alternative for LCW and would overcome

the cladding material issues restricting the mass applications of LCW technology. The index of the core is not limited by the liquid flowing through, hence issues of a low index cladding is not prominent in the technology developed in this project.

The basic theory behind waveguiding and attenuation in waveguides has been presented. The nanoporous polymers from which the waveguides were developed were obtained from PB-*b*-PDMS self assembling coblock polymers. PB can be easily funtionalized at a later stage in development, which was one of the deciding factors for the choice of material. The sacrificial porogen approach, where minority component of the assembling block (PDMS) is selectively removed from the phase separated polymer hybrid, was used to introduce porosity in the nanopores. Nanoporous polymers with 44% volume porosity was developed. This makes the effective index of the developed material to be n_{eff}= 1.26. This work was done in close collaboration with LiCorT project partners from DTU Chemical Engineering and DTU Nanotech, Technical University of Denmark.

Ndoni et al. [99] and Berthold et al. [100] has shown that surface modification of the air-polymer interface can make these naturally hydrophobic NP polymers hydrophilic. In this thesis, UV assisted chemistry was used to introduce hydrophilic functional groups in the air-polymer interface. This made the UV exposed regions surface wettable. The induced hydrophilicity was then exploited to fill the nanopores with aqueous solution. Fluorophore infiltration was used to prove the water intake in the modified polymer region. Analytical techniques like FTIR spectroscopy were used to analyse modified samples. Contact angle measurements also helped with proving the hydrophilicity induced in these polymers. On infiltrating with aqueous solution, the effective refractive index of the nanoporous polymers was increased by a value Δn_{eff}=0.17. The region with increased index surrounded by unwettable NP polymers was used to confine and guide visible light. Characterization of the waveguides were done by evaluating their losses. Substitution method was used to evaluate the propagation losses in these waveguides.

Two different methods were used for forming hydrophilic ends at the polymer-air interface. Controlled photo-oxidation of nanoporous polymers for 24 h rendered the hydrophobic polymer hydrophillic. The UV induced reactions in presence of oxygen attacks the pendant double bonds in the 1,2-PB polymer to form carboxyl and hydroxyl photo products. A transition loss of 3.8±0.5 dB and a propagation loss of 0.62±0.03 dB/mm were obtained in the photo-oxidation modified NP SLCWs. A bend loss of 0.81 dB/90° bend for the smallest bend radius, 1.75 mm was also measured. For improving the processing time, the losses observed and the reproducibilty of functional devices, a new method of surface modification was adopted. The second

method of making hydrophilicity at the air-polymer interface was to use thiol-ene click chemistry. Hydrothiolation or attaching thiols onto the double bonds in the polymer was initiated using initiators in the presence of UV light (I line: 365 nm). The project makes use of two different thiols for the purpose. Grafting the two thiols at the pendant bonds make the surface hydrophilic as carboxyl groups of MSA and sulphonated salt end group in MESNA were hydrophilic. In MSA loaded NP polymers, a UV exposure of 30 min grafted the carboxylic groups. The devices obtained using this modification showed a propagation loss of 0.26 $\pm$0.05 dB/mm. In MESNA loaded NP polymers, a UV exposure of only 4 min grafted the sulphonated salt ends onto the pendant double bonds. A propagation loss of 0.54$\pm$0.05 dB/mm was neasured in these devices. It was documented that thiol-ene click modified waveguides were an advantage over the photo-oxidation modified NP polymers. The decision for the most preffered modification chemistry has not been made. Modification using photo-oxidation was discarded due to very low reproducibility and long processing time. For thiol-ene chemistry modified devices, eventhough, MESNA devices have high propagation loss compared to MSA devices, processing time in the former was an attractive feature for doing some further work in this direction. The decision for the most preffered thiol for thiol-ene modification is still pending.

An optofluidic application for NP polymer LCW was also discussed in this project. The potential application of using NP polymer platform as a suitable optofluidic device to analyse turbid liquids was discussed. Milk with 0.5% fat was used for the purpose. Compared to a loss of 10.6 dB/mm in cuvettes, milk in NP LCW showed only 0.05 dB/mm. To prove size based filtration, fluorophores of sizes $>$ 14 nm and $<$ 14 nm (nanopore size) were used. Fluorescence spectroscopy, fluorescence imaging and confocal imaging were used to confirm Rhodamine B (size $<$ 14 nm) infiltration and filtering out of 2.5 μm and 22 nm fluorescing beads from the nanopores of NP polymers. The possibility of implementing label free detection in NP SLCW was also discussed. The combined effect of waveguiding and nanofilering make NP LCW a promising platform for new applications in optofluidics, such as large surface area like fluorescence based analysis devices and lab-on-a-chip medical devices.

7.1 Outlook: Improvements

The devices were developed primarily for making one-time-use devices. Thus if propagation loss and other values for different devices vary too much, such a technology will be difficult to implement as intended. To improve the performance of NP SLCW, some fabrication and measurements suggestions are given in this section. Photo-oxidation modified NP polymers were difficult to

reproduce. By implementing the developed (Chapter 5: Characterization of waveguides) polymer manufacturing, their performance may improve. However, owing to long processing times compared to other modification technique, photo-oxidation will be a poor choice to pursue. Accordingly, this section only deals with improvements for thiol-ene modified devices.

For thiol-ene modification, the aluminium chuck design (Chapter 4:Thiol-ene click chemistry) can be further improved for reducing the amount of thiol solution used. Designing a holder for UV mask and a holder for the wafer shaped polymer (like in standard photolithography) will allow fabrication reproducibility. In this work, the distance from the sample and the exposure source was adjusted manually, which might change the mask alignment and contact with thiol solution. If this step can be automated, this will also ensure similar fabrication conditions.

The UV exposure times chosen in the modifications were decided on such that modification was observed over the entire cross section of the device. Due to time constraints, experiments evaluating propagation loss for different UV exposure times were not carried out in the project. Such an experiment would determine the UV exposure time required for funcitonalizing the exposed regions fully, as well as the least required exposure time. To improve coupling losses in these waveguides, wall roughness of the waveguide edges should be addressed. In the project, the devices were diced out from the polymers using normal razor blades. Using micromilling for dicing the devices would improve the edge roughness and reduce coupling loss in these devices. Also in current techniques, FEP (n= 1.35) sheets form the cladding layers in x direction (Chapter 3: Modes in planar waveguides). By using NP polymer clad layers in the x direction, light can be confined in similar conditions as in z direction. To improve the experimental setup, fiber optic beam splitters (fiber couplers) are suggested in place of free space beam splitters. This will account for the additional error that occurs due to misalignment of the input and collection fibers. Bend loss measurements may further improve characterization of these devices.

For the nanofiltering application discussed in the thesis, fluorescence based detection was demonstrated. Ideally, these polymer devices will be used as an inexpensive label free detection technique. To quantify the sensitivity in these devices, certain absorbing dyes with high quantum efficiency should be infiltrated and their absorption should be measured as a function of infiltrating concentration. The device physics, such as diffusion should be modeled both analytically and numerically.

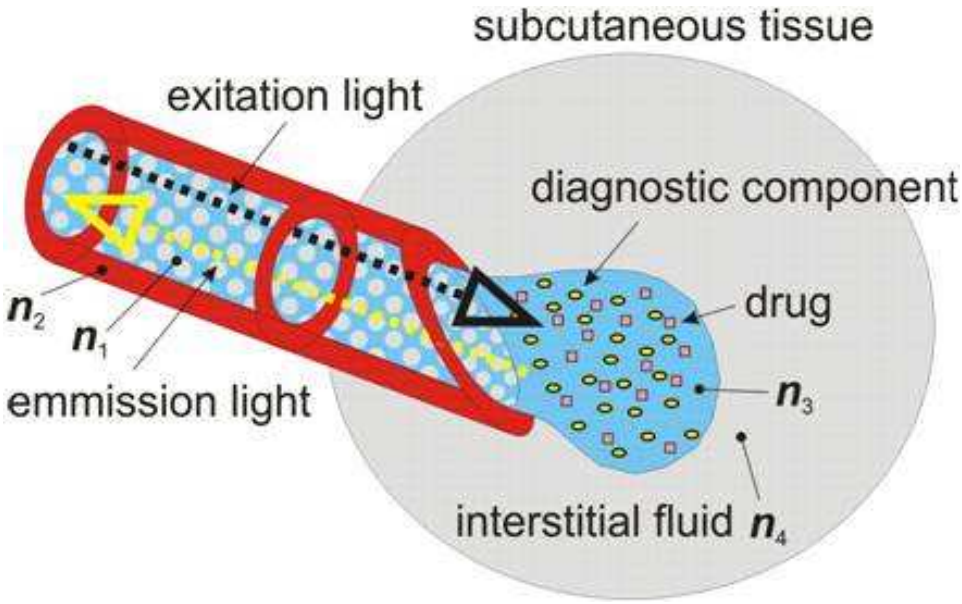

***Figure 7.1**: Schematic representation of a possible microneedle application for NP polymers.*

7.2 Future scope

Development of such low index nanoporous materials with controlled morphology and engineered chemical and mechanical properties can lead to highly promising sensing platforms for life sciences. With proper automation and device integration such a material platform could be developed to a diagnostic level where self treatment may be possible. One such possible application is a microneedle for drug delivery combined with integrated label free sensing [148]. Fig. 7.1 schematically shows a possible NP polymer design for microneedles. The modified LCW channel could simultaneously be used to deliver drugs as well as light guiding and optical sensing.

7.2.1 NP polymer dye lasers

Another possible application of these NP polymers is to use them as an optofluidic light source. Microfabricated liquid dye lasers or optofludic dye lasers are widely used as integrated light sources [50, 18]. The optical gain medium of the lasers are organic dye molecule in solvents like alcohol/water [149], or cast into the solid matrix [150]. The optical feedback of these lasers are provided by integrated optical components like mirrors [151], gratings [152], photonic crystals [153]. The developed NP SLCWs can be used as a suitable platform for developing such optofluidic lasers. Some experiments

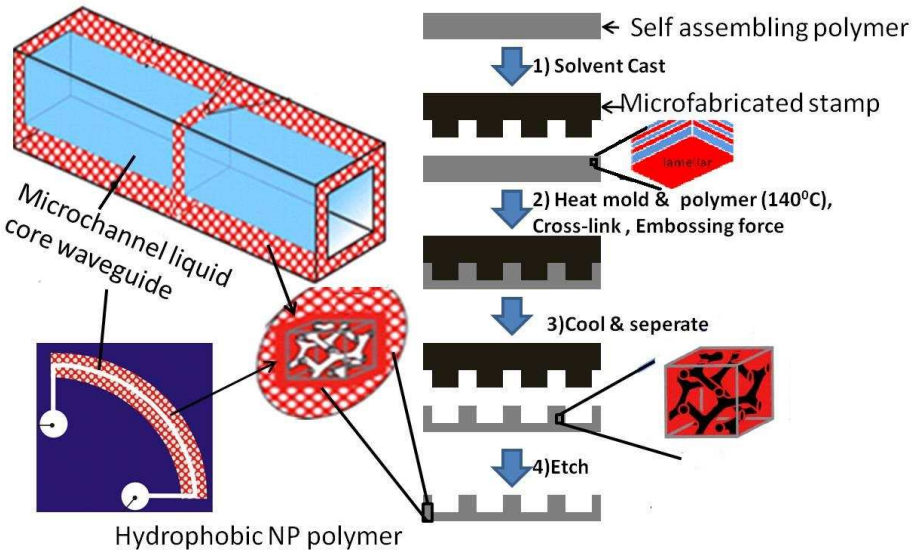

***Figure 7.2**: Schematic representation of a possible nanoporous cladding waveguide fabrication. The waveguides are also schematically represented.*

were carried out to check whether organic dyes could be infiltrated into the NP polymer matrix. Since THF is a good solvent for PB polymer, Rhodamine 6G dye dissolved in THF can be easily casted onto the polymer matrix. Fabricated NP polymers were immersed in Rhodamine 6G dye solution in THF overnight. These dye doped devices were then subjected to UV assisted thiol-ene chemistry for introducing surface modification. A pulsed laser at 532nm was used to obtain efficient spontaneous emission from these Rhodamine 6G doped devices. In principle, an optofluidic laser can be devloped by integrating an optical feedback to this system.

7.2.2 Nanoporous cladding waveguides

The fabricated NP polymer surfaces were modified chemically and were used to guide light. The core in these waveguides were made up of solid polymer with nanopores filled with liquid. They form solid liquid core waveguides. The developed NP polymers form a suitable cladding material for liquid core waveguiding as their n_{eff} =1.26. Microfluidic channels with liquid core surrounded by a lower refractive index nanoporous material can be developed using these polymers. Using silicon stamps, the waveguide patterns can be embossed on to the solvent casted polymer (starting material used in NP SLCW). With partial cross linking, the polymer soldifies and is separated from the stamp. Another partially cross linked polymer can then be casted alongside for making device lid. Following this, two polymers can

be fully cross linked together to attain the devices. Such a microchannel could be filled with liquid and light can guided through. Fig. 7.2 gives a schematic representation of the fabrication suggested along with the waveguides. Some initial work regarding such an application was carried out in this project. Challenges exists, such as difficulties in delaminating the polymer from stamp, cracking of finished devices, liquid filling difficulties etc. This is a promising future prospective for NP polymers.

Bibliography

[1] K Sasaki, F Ohno, A Motegi, and T Baba. Arrayed waveguide grating of 70x60 mu m(2) size based on Si photonic wire waveguides. *ELECTRONICS LETTERS*, 41(14):801–802, JUL 7 2005.

[2] Robert D Waterbury, Wensheng Yao, and Robert H Byrne. Long pathlength absorbance spectroscopy: trace analysis of fe(ii) using a 4.5m liquid core waveguide. *Analytica Chimica Acta*, 357(1-2):99 – 102, 1997.

[3] Demetri Psaltis, Stephen R. Quake, and Changhuei Yang. Developing optofluidic technology through the fusion of microfluidics and optics. *Nature*, 442(7101):381–386, 2006.

[4] Brian Bilenberg, Torben Rasmussen, Soren Balslev, and Anders Kristensen. Real-time tunability of chip-based light source enabled by microfluidic mixing. *Journal of Applied Physics*, 99(2):023102, 2006.

[5] P. Domachuk, M. Cronin-Golomb, B. Eggleton, S. Mutzenich, G. Rosengarten, and A. Mitchell. Application of optical trapping to beam manipulation in optofluidics. *Opt. Express*, 13(19):7265–7275, Sep 2005.

[6] Morten Gersborg-Hansen and Anders Kristensen. Optofluidic third order distributed feedback dye laser. *APPLIED PHYSICS LETTERS*, 89(10), SEP 4 2006.

[7] Mads Brokner Christiansen, Joanna Malgorzata Lopacinska, Mogens Havsteen Jakobsen, Niels Asger Mortensen, Martin Dufva, and Anders Kristensen. Polymer photonic crystal dye lasers asoptofluidic cell sensors. *Opt. Express*, 17(4):2722–2730, Feb 2009.

[8] Hao Li and Xudong Fan. Characterization of sensing capability of optofluidic ring resonator biosensors. *APPLIED PHYSICS LETTERS*, 97(1), JUL 5 2010.

[9] Xiaole Mao, Sz-Chin Steven Lin, Michael Ian Lapsley, Jinjie Shi, Bala Krishna Juluri, and Tony Jun Huang. Tunable Liquid Gradient Refractive Index (L-GRIN) lens with two degrees of freedom. *LAB ON A CHIP*, 9(14):2050–2058, 2009.

[10] Jinjie Shi, Zak Stratton, Sz-Chin Steven Lin, Hua Huang, and Tony Jun Huang. Tunable optofluidic microlens through active pressure control of an air-liquid interface. *MICROFLUIDICS AND NANOFLUIDICS*, 9(2-3):313–318, AUG 2010.

[11] Aram J. Chung and David Erickson. Optofluidic waveguides for reconfigurable photonic systems. *Opt. Express*, 19(9):8602–8609, Apr 2011.

[12] Jong-Min Lim, Se-Heon Kim, Jae-Hoon Choi, and Seung-Man Yang. Fluorescent liquid-core/air-cladding waveguides towards integrated optofluidic light sources. *Lab Chip*, 8:1580–1585, 2008.

[13] Allen H. J. Yang and David Erickson. Optofluidic ring resonator switch for optical particle transport. *Lab Chip*, 10:769–774, 2010.

[14] John T. Gohring, Paul S. Dale, and Xudong Fan. Detection of her2 breast cancer biomarker using the optofluidic ring resonator biosensor. volume 7682, page 768209. SPIE, 2010.

[15] Gaoshan Huang, Vladimir A. Bolan os Quin ones, Fei Ding, Suwit Kiravittaya, Yongfeng Mei, and Oliver G. Schmidt. Rolled-up optical microcavities with subwavelength wall thicknesses for enhanced liquid sensing applications. *ACS Nano*, 4(6):3123–3130, 2010.

[16] Aaron R. Hawkins and Holger Schmidt. Optofluidic waveguides: II. Fabrication and structures. *MICROFLUIDICS AND NANOFLUIDICS*, 4(1-2):17–32, JAN 2008.

[17] Holger Schmidt and Aaron R. Hawkins. Optofluidic waveguides: I. Concepts and implementations. *MICROFLUIDICS AND NANOFLUIDICS*, 4(1-2):3–16, JAN 2008.

[18] Aaron R.Hawkins and Holger Schmidt, editors. *Handbook of Optofluidics*. CRC Press, London, 2010.

[19] H. Schmidt. *Optical Guided-wave Chemical and Biosensors II,'Liquid-Core Waveguide Sensors'*.

[20] R.G.Hunsperger. *Integrated optics*. Springer, sixth edition, 2009.

[21] K.Okamoto. *Fundamentals of optical waveguides*. Elsevier, second edition, 2006.

[22] Allan.W.Snyder and John.D.Love, editors. *Optical Waveguide Theory*. Chapman and Hall, London, 1983.

[23] M.Born and E.Wolf. *Principles of Optics*. A Wheaton and Co Ltd, Exeter, sixth edition, 1983.

[24] S. Ginestar, F. van Dijk, A. Accard, F. Poingt, F. Pommereau, L. Le Gouezigou, O. Le Gouezigou, F. Lelarge, B. Rousseau, J. Landreau, J. P. Vilcot, and G. H. Duan. Tunable dual-mode DFB laser for millimetre-wave signal generation. *EUROPEAN PHYSICAL JOURNAL-APPLIED PHYSICS*, 53(3), MAR 2011.

[25] Benedicte Lebeau and Plinio Innocenzi. Hybrid materials for optics and photonics. *CHEMICAL SOCIETY REVIEWS*, 40(2):886–906, 2011.

[26] JirI[combining acute accent] Homola, Sinclair S. Yee, and G?nter Gauglitz. Surface plasmon resonance sensors: review. *Sensors and Actuators B: Chemical*, 54(1-2):3 – 15, 1999.

[27] Christoph Vannahme, Sönke Klinkhammer, Uli Lemmer, and Timo Mappes. Plastic lab-on-a-chip for fluorescence excitation with integrated organic semiconductor lasers. *Opt. Express*, 19(9):8179–8186, Apr 2011.

[28] Richard M. Parker, James C. Gates, Martin C. Grossel, and Peter G. Smith. An integrated optofluidic bragg grating device to measure the dynamic composition of a fluid system. In *Conference on Lasers and Electro-Optics*, page JWA61. Optical Society of America, 2010.

[29] I.K. Ilev and R.W. Waynant. All-fiber-optic evanescent liquid level and leak sensor. In *Lasers and Electro-Optics, 1999. CLEO '99. Summaries of Papers Presented at the Conference on*, pages 157 –158, may 1999.

[30] C. Monat, P. Domachuk, and B. J. Eggleton. Integrated optofluidics: A new river of light. *NATURE PHOTONICS*, 1(2):106–114, FEB 2007.

[31] Torsten Beck, Mario Hauser, Tobias Grossmann, Dominik Floess, Simone Schleede, Julian Fischer, Christoph Vannahme, Timo Mappes, and Heinz Kalt. Pmma-micro goblet resonators for biosensing applications. volume 7888, page 78880A. SPIE, 2011.

[32] Bjorn Agnarsson, Saevar Ingthorsson, Thorarinn Gudjonsson, and Kristjan Leosson. Evanescent-wave fluorescence microscopy using

symmetric planar waveguides. *Opt. Express*, 17(7):5075–5082, Mar 2009.

[33] Ian M. White, John Gohring, Yuze Sun, Gilmo Yang, Scott Lacey, and Xudong Fan. Versatile waveguide-coupled optofluidic devices based on liquid core optical ring resonators. *Applied Physics Letters*, 91(24):241104, 2007.

[34] Venumadhav Korampally, Somik Mukherjee, Maruf Hossain, Rosalynn Manor, Minseong Yun, Keshab Gangopadhyay, Luis Polo-Parada, and Shubhra Gangopadhyay. Development of a Miniaturized Liquid Core Waveguide System With Nanoporous Dielectric Cladding-A Potential Biosensing Platform. *IEEE Sensors Journal*, 9(12):1711–1718, DEC 2009.

[35] Sung Hwan Cho, Jessica Godin, and Yu-Hwa Lo. Optofluidic Waveguides in Teflon AF-Coated PDMS Microfluidic Channels. *IEEE PHOTONICS TECHNOLOGY LETTERS*, 21(15):1057–1059, AUG 1 2009.

[36] Jong-Min Lim, Se-Heon Kim, and Seung-Man Yang. Liquid–liquid fluorescent waveguides using microfluidic-drifting-induced hydrodynamic focusing. *Microfluidics and Nanofluidics*, 10:211–217, 2011. 10.1007/s10404-010-0649-5.

[37] R Altkorn, I Koev, RP VanDuyne, and M Litorja. Low-loss liquid-core optical fiber for low-refractive-index liquids: fabrication, characterization, and application in Raman spectroscopy. *Appl. Opt.*, 36(34):8992–8998, DEC 1 1997.

[38] P Dress and H Franke. Increasing the accuracy of liquid analysis and pH-value control using a liquid-core waveguide. *REVIEW OF SCIENTIFIC INSTRUMENTS*, 68(5):2167–2171, MAY 1997.

[39] Hiromi Takiguchi, Azusa Tsubata, Makoto Miyata, Tamao Odake, Hiroki Hotta, Tomonari Umemura, and Kin ichi Tsunoda. Liquid core waveguide spectrophotometry for the sensitive determination of nitrite in river water samples. *Analytical Sciences*, 22(7):1017–1019, 2006.

[40] Jian Ma, Purnendu K. Dasgupta, William Blackledge, and Gerry R. Boss. Cobinamide-Based Cyanide Analysis by Multiwavelength Spectrometry in a Liquid Core Waveguide. *ANALYTICAL CHEMISTRY*, 82(14):6244–6250, JUL 15 2010.

[41] A Datta, IY Eom, A Dhar, P Kuban, R Manor, I Ahmad, S Gangopadhyay, T Dallas, M Holtz, F Temkin, and PK Dasgupta. Microfabrication and characterization of Teflon AF-coated liquid core waveguide

channels in silicon. *IEEE SENSORS JOURNAL*, 3(6):788–795, DEC 2003.

[42] R Manor, A Datta, I Ahmad, M Holtz, S Gangopadhyay, and T Dallas. Microfabrication and characterization of liquid core waveguide glass channels coated with Teflon AF. *IEEE SENSORS JOURNAL*, 3(6):687–692, 2003.

[43] Dahu Qi and Andrew J. Berger. Chemical concentration measurement in blood serum and urine samples using liquid-core optical fiber Raman spectroscopy. *Appl. Opt.*, 46(10):1726–1734, APR 1 2007.

[44] M Holtz, PK Dasgupta, and GF Zhang. Small-volume raman spectroscopy with a liquid core waveguide. *Analytical Chemistry*, 71(14):2934–2938, JUL 15 1999.

[45] Asahi Glass Co. http://www.bellexinternational.com/, May 2011.

[46] Jennifer Halldorsson, Nina B. Arnfinnsdottir, Asta B. Jonsdottir, Björn Agnarsson, and Kristjan Leosson. High index contrast polymer waveguide platform for integrated biophotonics. *Opt. Express*, 18(15):16217–16226, Jul 2010.

[47] H Takiguchi, T Odake, M Ozaki, T Umemura, and KI Tsunoda. Liquid/liquid optical waveguides using sheath flow as a new tool for liquid/liquid interfacial measurements. *APPLIED SPECTROSCOPY*, 57(8):1039–1041, AUG 2003.

[48] DB Wolfe, RS Conroy, P Garstecki, BT Mayers, DV Vesenov, MA Fischbach, KE Paul, M Prentiss, and GM Whitesides. Dynamic control of liquid-core/liquid-cladding optical waveguides. In *2005 Conference on Lasers & Electro-Optics (CLEO), Vols 1-3*, pages 1680–1682, 2010 MASSACHUSETTS AVE NW, WASHINGTON, DC 20036 USA, 2005. OPTICAL SOC AMERICA. Conference on Lasers and Electro-Optics (CLEO), Baltimore, MD, MAY 22-27, 2005.

[49] M Brown, T Vestad, J Oakey, and DWM Marr. Optical waveguides via viscosity-mismatched microfluidic flows. *APPLIED PHYSICS LETTERS*, 88(13), MAR 27 2006.

[50] Zhenyu Li and Demetri Psaltis. Optofluidic dye lasers. *Microfluidics and Nanofluidics*, 4:145–158, 2008. 10.1007/s10404-007-0225-9.

[51] WP Risk, HC Kim, RD Miller, H Temkin, and S Gangopadhyay. Optical waveguides with an aqueous core and a low-index nanoporous cladding. *OPTICS EXPRESS*, 12(26):6446–6455, DEC 27 2004.

[52] Jasenka Memisevic, Venumadhav Korampally, Shubhra Gangopadhyay, and Sheila A. Grant. Characterization of a novel ultra-low

refractive index material for biosensor application. *SENSORS AND ACTUATORS B-CHEMICAL*, 141(1):227–232, AUG 18 2009.

[53] Vilson R. Almeida, Qianfan Xu, Carlos A. Barrios, and Michal Lipson. Guiding and confining light in void nanostructure. *Opt. Lett.*, 29(11):1209–1211, Jun 2004.

[54] Soon Thor Lim, Ching Eng Png, and Aaron J. Danner. Embedded air core optical nano-waveguides. *JOURNAL OF THE OPTICAL SOCIETY OF AMERICA B-OPTICAL PHYSICS*, 27(10):1937–1941, OCT 2010.

[55] Allen H. J. Yang, Sean D. Moore, Bradley S. Schmidt, Matthew Klug, Michal Lipson, and David Erickson. Optical manipulation of nanoparticles and biomolecules in sub-wavelength slot waveguides. *NATURE*, 457(7225):71–75, JAN 1 2009.

[56] Cicero Martelli, John Canning, Katja Lyytikainen, and Nathaniel Groothoff. Water-core fresnel fiber. *Opt. Express*, 13(10):3890–3895, May 2005.

[57] John Canning, Elizabeth Buckley, and Katja Lyytikainen. Propagation in air by field superposition of scattered light within a fresnel fibre. In *Optical Fiber Communication Conference*, page MF2. Optical Society of America, 2003.

[58] X. Zhu, A. Schülzgen, H. Li, H. Wei, J. V. Moloney, and N. Peyghambarian. Coherent beam transformations using multimode waveguides. *Opt. Express*, 18(7):7506–7520, Mar 2010.

[59] P YEH, A YARIV, and CS HONG. ELECTROMAGNETIC PROPAGATION IN PERIODIC STRATIFIED MEDIA .1. GENERAL THEORY. *JOURNAL OF THE OPTICAL SOCIETY OF AMERICA*, 67(4):423–438, 1977.

[60] Yoel Fink, Daniel J. Ripin, Shanhui Fan, Chiping Chen, John D. Joannopoulos, and Edwin L. Thomas. Guiding optical light in air using an all-dielectric structure. *J. Lightwave Technol.*, 17(11):2039, Nov 1999.

[61] Kristopher J. Rowland, Shahraam Afshar V., Alexander Stolyarov, Yoel Fink, and Tanya M. Monro. Spectral properties of liquid-core bragg fibers. In *Conference on Lasers and Electro-Optics/International Quantum Electronics Conference*, page CThE2. Optical Society of America, 2009.

[62] Pochi Yeh, Amnon Yariv, and Emanuel Marom. Theory of bragg fiber. *J. Opt. Soc. Am.*, 68(9):1196–1201, Sep 1978.

[63] P YEH and A YARIV. BRAGG REFLECTION WAVEGUIDES. *OPTICS COMMUNICATIONS*, 19(3):427–430, 1976.

[64] P Russell. Photonic crystal fibers. *SCIENCE*, 299(5605):358–362, JAN 17 2003.

[65] P. Roberts, F. Couny, H. Sabert, B. Mangan, D. Williams, L. Farr, M. Mason, A. Tomlinson, T. Birks, J. Knight, and P. St. J. Russell. Ultimate low loss of hollow-core photonic crystal fibres. *Opt. Express*, 13(1):236–244, Jan 2005.

[66] W. Jin, H. F. Xuan, and H. L. Ho. Sensing with hollow-core photonic bandgap fibers. *MEASUREMENT SCIENCE & TECHNOLOGY*, 21(9, Sp. Iss. SI), SEP 2010.

[67] Rebecca Newhouse Jin Z. Zhang Xuan Yang, Chao Shi and Claire Gu. Hollow-Core Photonic Crystal Fibers for Surface-Enhanced Raman Scattering Probes. *International Journal of Optics*, 2011, 2011.

[68] CJM Smith, H Benisty, S Olivier, M Rattier, C Weisbuch, TF Krauss, RM De La Rue, R Houdre, and U Oesterle. Low-loss channel waveguides with two-dimensional photonic crystal boundaries. *APPLIED PHYSICS LETTERS*, 77(18):2813–2815, OCT 30 2000.

[69] Y Sugimoto, Y Tanaka, N Ikeda, Y Nakamura, K Asakawa, and K Inoue. Low propagation loss of 0.76 dB/mm in GaAs-based single-line-defect two-dimensional photonic crystal slab waveguides up to 1 cm in length. *OPTICS EXPRESS*, 12(6):1090–1096, MAR 22 2004.

[70] M Loncar, D Nedeljkovic, T Doll, J Vuckovic, A Scherer, and TP Pearsall. Waveguiding in planar photonic crystals. In Robbins, DJ and Trezza, JA and Jabbour, GE, editor, *SILICON-BASED AND HYBRID OPTOELECTRONICS III*, volume 4293 of *PROCEEDINGS OF THE SOCIETY OF PHOTO-OPTICAL INSTRUMENTATION ENGINEERS (SPIE)*, pages 94–99, 1000 20TH ST, PO BOX 10, BELLINGHAM, WA 98227-0010 USA, 2001. SPIE, SPIE-INT SOC OPTICAL ENGINEERING. Conference on Silicon-based and Hybrid Optoelectronics III, SAN JOSE, CA, JAN 23-24, 2001.

[71] David Erickson, Troy Rockwood, Teresa Emery, Axel Scherer, and Demetri Psaltis. Nanofluidic tuning of photonic crystal circuits - art. no. 647513. In Sidorin, Y and Waechter, CA, editor, *Integrated Optics: Devices, Materials, and Technologies XI*, volume 6475 of *PROCEEDINGS OF THE SOCIETY OF PHOTO-OPTICAL INSTRUMENTATION ENGINEERS (SPIE)*, page 47513, 1000 20TH ST, PO BOX 10, BELLINGHAM, WA 98227-0010 USA, 2007. SPIE, SPIE-INT SOC OPTICAL ENGINEERING. Conference on Integrated Optics - Devices, Materials, and Technology XI, San Jose, CA, JAN 22-24, 2007.

[72] JL ARCHAMBAULT, RJ BLACK, S LACROIX, and J BURES. LOSS CALCULATIONS FOR ANTIRESONANT WAVE-GUIDES. *JOURNAL OF LIGHTWAVE TECHNOLOGY*, 11(3):416–423, MAR 1993.

[73] David Erickson, Troy Rockwood, Teresa Emery, Axel Scherer, and Demetri Psaltis. Nanofluidic tuning of photonic crystal circuits. *Opt. Lett.*, 31(1):59–61.

[74] M. A. Duguay, Y. Kokubun, T. L. Koch, and Loren Pfeiffer. Antiresonant reflecting optical waveguides in sio[sub 2]-si multilayer structures. *Applied Physics Letters*, 49(1):13–15, 1986.

[75] Thomas Delonge and Henning Fouckhardt. Integrated optical detection cell based on bragg reflecting waveguides. *Journal of Chromatography A*, 716(1-2):135 – 139, 1995. 7th International Symposium on High Performance Capillary Electrophoresis.

[76] Evan J. Lunt, Bin Wu, Jared M. Keeley, Philip Measor, Holger Schmidt, and Aaron R. Hawkins. Hollow ARROW Waveguides on Self-Aligned Pedestals for Improved Geometry and Transmission. *IEEE PHOTONICS TECHNOLOGY LETTERS*, 22(15):1147–1149, AUG 1 2010.

[77] D. Yin, Holger Schmidt, J. Barber, and A. Hawkins. Integrated arrow waveguides with hollow cores. *Opt. Express*, 12(12):2710–2715, 2004.

[78] DL Yin, JP Barber, AR Hawkins, and H Schmidt. Waveguide loss optimization in hollow-core ARROW waveguides. *OPTICS EXPRESS*, 13(23):9331–9336, NOV 14 2005.

[79] Dongliang Yin, Holger Schmidt, John P. Barber, and Aaron R. Hawkins. Highly sensitive fluorescence detection from optimized liquid-core arrow waveguides. In *Conference on Lasers and Electro-Optics/Quantum Electronics and Laser Science and Photonic Applications Systems Technologies*, page CTuD5. Optical Society of America, 2005.

[80] R. Bernini, E. De Nuccio, A. Minardo, L. Zeni, and P. M. Sarro. Liquid-core/liquid-cladding integrated silicon ARROW waveguides. *OPTICS COMMUNICATIONS*, 281(8):2062–2066, APR 15 2008.

[81] S. Kuhn, P. Measor, E. J. Lunt, B. S. Phillips, D. W. Deamer, A. R. Hawkins, and H. Schmidt. Loss-based optical trap for on-chip particle analysis. *Lab Chip*, 9:2212–2216, 2009.

[82] efibertools. http://www.efibertools.com/generic-liquid-light-guide-8mm-core-1-5-meter/, May 2011.

[83] LUMATEC (DE) produces liquid lightguides (fibers) improved UV transmission. http://www.lumatec.de/ehome/ehome.htm, May 2011.

[84] Cristiano M B Cordeiro, Christiano J S de Matos, Eliane M dos Santos, Alexandre Bozolan, Jackson S K Ong, Tilon Facincani, Giancarlo Chesini, Alfredo R Vaz, and Carlos H Brito Cruz. Towards practical liquid and gas sensing with photonic crystal fibres: side access to the fibre microstructure and single-mode liquid-core fibre. *Measurement Science and Technology*, 18(10):3075, 2007.

[85] Ioannis Papakonstantinou, Kai Wang, David R. Selviah, and F. Aníbal Fernández. Transition, radiation and propagation loss in polymer multimode waveguide bends. *Opt. Express*, 15(2):669–679, 2007.

[86] Shiyang Zhu, Q. Fang, M. B. Yu, G. Q. Lo, and D. L. Kwong. Propagation losses in undoped and n-doped polycrystalline silicon wire waveguides. *OPTICS EXPRESS*, 17(23):20891–20899, NOV 9 2009.

[87] Charles Kittel. *Introduction to Solid State Physics*. John Wiley and Sons, eighth edition, 2005.

[88] D E Aspnes. Local-field effects and effective-medium theory: A microscopic perspective. *American Journal of Physics*, 50(8):704–709, 1982.

[89] Wilfried Heller. Remarks on refractive index mixture rules. *The Journal of Physical Chemistry*, 69(4):1123–1129, 1965.

[90] R. Rotomskis, V. Vaicaitis, and A. Piskarskas. Time-resolved absorption spectroscopy of hematoporphyrin and its photoproducts. *Chemical Physics Letters*, 202(3-4):233 – 236, 1993.

[91] Henrik Bruus, editor. *Theoretical Microfluidics*. Oxford University Press Inc., New York, 2008.

[92] P. Huber, S. Gruener, C. Schaefer, K. Knorr, and A. V. Kityk. Rheology of liquids in nanopores: A study on the capillary rise of water, n-Hexadecane and n-Tetracosane in mesoporous silica. *EUROPEAN PHYSICAL JOURNAL-SPECIAL TOPICS*, 141:101–105, FEB 2007. 3rd International Workshop on Dynamics in Confinement, Grenoble, FRANCE, MAR 23-26, 2006.

[93] William A. Phillip, Javid Rzayev, Marc A. Hillmyer, and E. L. Cussler. Gas and water liquid transport through nanoporous block copolymer membranes. *JOURNAL OF MEMBRANE SCIENCE*, 286(1-2):144–152, DEC 15 2006.

[94] G Martic, J De Coninck, and T.D Blake. Influence of the dynamic contact angle on the characterization of porous media. *Journal of Colloid and Interface Science*, 263(1):213 – 216, 2003.

[95] Edward W. Washburn. The dynamics of capillary flow. *Phys. Rev.*, 17(3):273–283, Mar 1921.

[96] A SCHWARCZ. SURFACE-TENSION OF POLYMER MIXTURES AND COPOLYMERS. *JOURNAL OF POLYMER SCIENCE PART B-POLYMER PHYSICS*, 12(6):1195–1205, 1974.

[97] BB SAUER and NV DIPAOLO. SURFACE-TENSION AND DYNAMIC WETTING OF POLYMERS USING THE WIHELMY METHOD - APPLICATIONS TO HIGH MOLECULAR-WEIGHTS AND ELEVATED-TEMPERATURES. *JOURNAL OF COLLOID AND INTERFACE SCIENCE*, 144(2):527–537, JUL 1991.

[98] L KORSON, DROSTHAN.W, and FJ MILLERO. VISCOSITY OF WATER AT VARIOUS TEMPERATURES. *JOURNAL OF PHYSICAL CHEMISTRY*, 73(1):34–&, 1969.

[99] Sokol Ndoni, Li Li, Lars Schulte, Piotr Przemyslaw Szewczykowski, Thomas Willum Hansen, Fengxiao Guo, Rolf Henrik Berg, and Martin Etchells Vigild. Controlled photooxidation of nanoporous polymers. *Macromolecules*, 42:3877–3880, 2009.

[100] A. Berthold, K. S. Sagar, M. B. Christiansen, and S. Ndoni. Patterned hydrophilization of nanoporous 1,2-PB by thiol-ene photochemistry. *accepted for publication in Macromolecular Rapid communications* , 2011.

[101] MW Matsen and FS Bates. Origins of complex self-assembly in block copolymers. *MACROMOLECULES*, 29(23):7641–7644, NOV 4 1996.

[102] M STAMM and DW SCHUBERT. INTERFACES BETWEEN INCOMPATIBLE POLYMERS. *ANNUAL REVIEW OF MATERIALS SCIENCE*, 25:325–356, 1995.

[103] D.R.Salem. *Structure formation in polymeric fibers*. Carl Hanser Verlag, Munich,Germany, 2001.

[104] MA Hillmyer. Nanoporous materials from block copolymer precursors. In *BLOCK COPOLYMERS II*, volume 190 of *ADVANCES IN POLYMER SCIENCE*, pages 137–181. SPRINGER-VERLAG BERLIN, HEIDELBERGER PLATZ 3, D-14197 BERLIN, GERMANY, 2005.

[105] David A. Olson, Liang Chen, and Marc A. Hillmyer. Templating nanoporous polymers with ordered block copolymers. *CHEMISTRY OF MATERIALS*, 20(3):869–890, FEB 12 2008.

[106] S. Ndoni, C. M. Papadakis, F. S. Bates, and K. Almdal. Laboratory-scale setup for anionic polymerization under inert atmosphere. *Review of Scientific Instruments*, 66:1090–1095, February 1995.

[107] Wikipedia. http://en.wikipedia.org/wiki/polybutadiene, May 2011.

[108] S Ndoni, ME Vigild, and RH Berg. Nanoporous materials with spherical and gyroid cavities created by quantitative etching of polydimethylsiloxane in polystyrene-polydimethylsiloxane block copolymers. *Journal of the American Chemical Society*, 125(44):13366–13367, 2003.

[109] Lars Schulte, Anne Grydgaard, Mathilde R. Jakobsen, Piotr P. Szewczykowski, Fengxiao Guo, Martin E. Vigild, Rolf H. Berg, and Sokol Ndoni. Nanoporous materials from stable and metastable structures of 1,2-PB-b-PDMS block copolymers. *POLYMER*, 52(2):422–429, JAN 21 2011.

[110] WV ANDREW, TBK KHOO, and DT JACOBS. TESTING THE LORENTZ-LORENZ RELATION IN THE NEAR-CRITICAL BINARY FLUID MIXTURE ISOBUTYRIC ACID AND WATER. *JOURNAL OF CHEMICAL PHYSICS*, 85(7):3985–3991, OCT 1 1986.

[111] James.E.Mark, editor. *Polymer Data Handbook*. Oxford University Press, New York, second edition, 1999.

[112] K. S Sagar, N Gopalakrishnan, M. B Christiansen, A Kristensen, and S Ndoni. Photolithographic fabrication of hydrophilic solid-liquid core waveguides by thiol-ene chemistry. *Submitted to Journal of micromechanics and microengineering*, 2011.

[113] M Piton and A Rivaton. Photooxidation of polybutadiene at long wavelengths (lambda¿300nm). *POLYMER DEGRADATION AND STABILITY*, 53(3):343–359, 1996.

[114] Nimi Gopalakrishnan, Kaushal S. Sagar, Mads Brokner Christiansen, Martin E. Vigild, Sokol Ndoni, and Anders Kristensen. Uv patterned nanoporous solid-liquid core waveguides. *OPTICS EXPRESS*, 18(12):12903–12908, JUN 7 2010.

[115] Tasdelen M. A. Uygun, M. and Y. Yagci. Influence of type of initiation on thiol–ene “click” chemistry. *Macromolecular Chemistry and Physics*, 211:103–110, 2010.

[116] B.A Lowe. Thiol-ene ”click” reactions and recent applications in polymer and materials synthesis. *POLYMER CHEMISTRY*, 1:17–36, 2010.

[117] K. S. Sagar, N. Gopalakrishnan, M. B. Christiansen, A. Kristensen, and S. Ndoni. Photolithographic fabrication of solid-liquid core waveguides by thiol-ene chemistry. *submitted to Journal of Micromechanical Engineering*, 2011.

[118] S. Bakkialakshmi and T. Menaka. Fluorescence enhancement of rhodamine 6g by forming inclusion complexes with [beta]-cyclodextrin. *Journal of Molecular Liquids*, 158(2):117 – 123, 2011.

[119] Sami Musa, Albert Borreman, Abgail A. M. Kok, Mart B. J. Diemeer, and Alfred Driessen. Experimental study of bent multimode optical waveguides. *Appl. Opt.*, 43(30):5705–5707, 2004.

[120] P. Steinvurzel, B. Kuhlmey, T. White, M. Steel, C. de Sterke, and B. Eggleton. Long wavelength anti-resonant guidance in high index inclusion microstructured fibers. *Opt. Express*, 12(22):5424–5433, Nov 2004.

[121] R.G.Hunsperger. *The Feynman Lectures on Physics*. Addison-Wesley, second edition, 2005.

[122] K Eiane, DL Aksnes, and J Giske. The significance of optical properties in competition among visual and tactile planktivores: A theoretical study. *ECOLOGICAL MODELLING*, 98(2-3):123–136, MAY 30 1997.

[123] Jee-Eun Min, Joo-Hyung Ryu, and Yu-Hwan Ahn. Spatial and temporal variations of the inherent and apparent optical properties in the sea areas around korea. In *REMOTE SENSING OF THE COASTAL OCEAN, LAND, AND ATMOSPHERE ENVIRONMENT*, Proceedings of SPIE-The International Society for Optical Engineering, 2010.

[124] VV Tuchin. Optical clearing of tissues and blood using the immersion method. *JOURNAL OF PHYSICS D-APPLIED PHYSICS*, 38(15):2497–2518, AUG 7 2005.

[125] Valery.V.Tuchin, editor. *Handbook of Optical Biomedical Diagnostics*. SPIE Press, 2002.

[126] A.S. Grandison and M. J. Lewis, editors. *Seperation processes in the Food and Biotechnolgy Industries- Principles and Applications*. Woodhead Pub, Cambridge,England, second edition, 1996.

[127] W. Schr?er, J. K?ser, and F. Kuhnen. Light-scattering in turbid fluids: The single-scattering intensity. *Journal of Molecular Liquids*, 134(1-3):40 – 48, 2007. EMLG/JMLG 2005 Special Issue, Annual Meeting of the EMLG/JMLG 2005.

[128] Tejal A. Desai, Derek J. Hansford, Lara Leoni, Matthias Essenpreis, and Mauro Ferrari. Nanoporous anti-fouling silicon membranes for biosensor applications. *Biosensors and Bioelectronics*, 15(9-10):453 – 462, 2000.

[129] Veldhuis G.J. Kuiper S. Van Rijn, C.J.M. Nanosieves with microsystem technology for microfiltration applications. *Nanotechnology*, 9(4):343–345, 1998. cited By (since 1996) 40.

[130] Christian Leger, Helio De L. Lira, and Russell Paterson. Preparation and properties of surface modified ceramic membranes. part ii. gas and liquid permeabilities of 5 nm alumina membranes modified by a monolayer of bound polydimethylsiloxane (pdms) silicone oil. *Journal of Membrane Science*, 120(1):135 – 146, 1996.

[131] M.Mulder. *Basic principles of membrane technology*. Kluwer, Dordrecht, second edition, 2003.

[132] M Lazzari and MA Lopez-Quintela. Block copolymers as a tool for nanomaterial fabrication. *ADVANCED MATERIALS*, 15(19):1583–1594, OCT 2 2003.

[133] Chia-Jung Chang, Chung-Shi Yang, Yun-Ju Chuang, Hwa-Seng Khoo, and Fan-Gang Tseng. Micro-patternable nanoporous polymer integrated with microstructures for molecular filtration. *NANOTECHNOLOGY*, 19(36), SEP 10 2008.

[134] Sun-Tak Hwang. Fundamentals of membrane transport. *KOREAN JOURNAL OF CHEMICAL ENGINEERING*, 2011.

[135] A. M. Zheltikov. Ray-optic analysis of the (bio)sensing ability of ring-cladding hollow waveguides. *Appl. Opt.*, 47(3):474–479, Jan 2008.

[136] E. P. Furlani, R. Biswas, and N. M. Litchinitser. Analysis of an Optofluidic Biochemical Sensor. *NSTI-Nanotech*, 3:66–69, 2010.

[137] Ville Jokinen and Sami Franssila. Capillarity in microfluidic channels with hydrophilic and hydrophobic walls. *MICROFLUIDICS AND NANOFLUIDICS*, 5(4):443–448, OCT 2008.

[138] V Buschmann, KD Weston, and M Sauer. Spectroscopic study and evaluation of red-absorbing fluorescent dyes. *BIOCONJUGATE CHEMISTRY*, 14(1):195–204, JAN-FEB 2003.

[139] GD Qian and MQ Wang. Study on the microstructural evolution of silica gel during sol-gel-gel-glass conversions using the fluorescence polarization of rhodamine b. *JOURNAL OF PHYSICS D-APPLIED PHYSICS*, 32(18):2462–2466, SEP 21 1999.

[140] Jian-Han Huang, Ke-Long Huang, Su-Qin Liu, A-Ting Wang, and Chen Yan. Adsorption of rhodamine b and methyl orange on a hypercrosslinked polymeric adsorbent in aqueous solution. *COLLOIDS AND SURFACES A-PHYSICOCHEMICAL AND ENGINEERING ASPECTS*, 330(1):55–61, NOV 20 2008.

[141] J. R. Lakowicz and A. Lakhtakia. *Principles of fluorescence spectroscopy*. Springer Series, New York, third edition, 2006.

[142] J. W. Lichtman and J. A. Conchello. Fluorescene microscopy. *Nature Methods*, 2:910–919, 2005.

[143] N Gopalakrishnan, M. B. Christiansen, and A Kristensen. Nanofiltering in nanoporous solid liquid core waveguides. *submitted to Optics Letters*, 2011.

[144] Fredrik Uhlin, Jonas Pettersson, Anders Fernstrom, and Lars-Goran Lindberg. Complementary parameter for dialysis monitoring based on UV absorbance. *HEMODIALYSIS INTERNATIONAL*, 13(4):492–497, OCT 2009.

[145] DO Forcato, MP Carmine, GE Echeverria, RP Pecora, and SC Kivatinitz. Milk fat content measurement by a simple UV spectrophotometric method: An alternative screening method. *JOURNAL OF DAIRY SCIENCE*, 88(2):478–481, FEB 2005.

[146] N.O. Mchedlov-Petrosyan and Yu.V. Kholin. Aggregation of rhodamine b in water. *Russian Journal of Applied Chemistry*, 77:414–422, 2004. 10.1023/B:RJAC.0000031281.69081.d0.

[147] H Du, RCA Fuh, JZ Li, LA Corkan, and JS Lindsey. PhotochemCAD: A computer-aided design and research tool in photochemistry. *PHOTOCHEMISTRY AND PHOTOBIOLOGY*, 68(2):141–142, AUG 1998.

[148] Mark R. Prausnitz. Microneedles for transdermal drug delivery. *Advanced Drug Delivery Reviews*, 56(5):581 – 587, 2004. Breaking the Skin Barrier.

[149] Wuzhou Song, Andreas E. Vasdekis, Zhenyu Li, and Demetri Psaltis. Low-order distributed feedback optofluidic dye laser with reduced threshold. *Applied Physics Letters*, 94(5):051117, 2009.

[150] Søren Balslev, Andrej Mironov, Daniel Nilsson, and Anders Kristensen. Micro-fabricated single mode polymer dye laser. *Opt. Express*, 14(6):2170–2177, Mar 2006.

[151] B Helbo, A Kristensen, and A Menon. A micro-cavity fluidic dye laser. *Journal of Micromechanics and Microengineering*, 13(2):307, 2003.

[152] Zhenyu Li, Zhaoyu Zhang, Axel Scherer, and Demetri Psaltis. Mechanically tunable optofluidic distributed feedback dye laser. *Opt. Express*, 14(22):10494–10499, Oct 2006.

[153] Felipe Bernal Arango, Mads Brokner Christiansen, Morten Gersborg-Hansen, and Anders Kristensen. Optofluidic tuning of photonic crystal band edge lasers. *Applied Physics Letters*, 91(22):223503, 2007.

Appendix A

List of Publications

A.1 Journal Articles

- **Nimi Gopalakrishnan**, Mads Brøkner Christiansen and Anders Kristensen.
  Nanofiltering via integrated liquid core waveguides.
  Submitted to Optics Letters, May **(2011)**.

- Kaushal S. Sagar, **Nimi Gopalakrishnan**, Mads Brøkner Christiansen, Anders Kristensen and Sokol Ndoni.
  Photolithographic fabrication of solid-liquid core waveguides by thiol-ene chemistry.
  Submitted to Journal of micromechanics and microengineering, April**(2011)**.

- **Nimi Gopalakrishnan**, Kaushal S. Sagar, Mads Brøkner Christiansen, Martin E. Vigild, Sokol Ndoni and Anders Kristensen.
  UV patterned nanoporous solid-liquid core waveguides.
  Optics Express, **18**(12), 12903-12908 **(2010)**.

A.2 Proceedings

- **Nimi Gopalakrishnan**, Mads B. Christiansen, Sokol Ndoni, Anders Kristensen, Kaushal S. Sagar, Martin. E. Vigild
  Nanoporous polymer liquid core waveguides.
  Lasers and Electro-Optics, Conference on and Quantum Electronics

and Laser Science Conference (CLEO/QELS): Novel waveguides **1**, (2010).

- Mads B. Christiansen, **Nimi Gopalakrishnan**, Sokol Ndoni, Anders Kristensen, Kaushal S. Sagar
  UV defined nanoporous liquid core waveguides.
  Sensors, 2010 IEEE **979**, (2010).

A.3 Conference Contributions (personally given)

- **Nimi Gopalakrishnan**, Anton Berthold, Kaushal S. Sagar, Mads Brøkner Christiansen, Sokol Ndoni and Anders Kristensen.
  Thiolene click chemistry modified Nanoporous Waveguides.
  Accepted for poster presentation at: EOSOF Munich, Germany (2011).
- **Nimi Gopalakrishnan**, Kaushal S. Sagar, Mads Brøkner Christiansen, Martin E. Vigild, Sokol Ndoni and Anders Kristensen.
  Nanoporous polymer liquid core waveguides.
  Accepted for oral presentation at: CLEO/IQEC, San Jose, CA, USA (2010).
- **Nimi Gopalakrishnan**, Kaushal S. Sagar, Mads Brøkner Christiansen, Martin E. Vigild, Sokol Ndoni and Anders Kristensen.
  Optofluidic applications using 1,2-PolyButadine nanoporous diblock copolymer.
  Accepted for poster presentation at: DFS First Nordic meeting, Kgs. Lyngby, Denmark (2009).
- **Nimi Gopalakrishnan**, Kaushal S. Sagar, Mads Brøkner Christiansen, Sokol Ndoni, Martin E. Vigild, Ole Hassager and Anders Kristensen.
  UV written Liquid Core Waveguides in 1, 2-Polybutadine (1,2-PB) nanoporous polymers.
  Accepted for poster presentation at: MNE, Ghent, Belgium (2009).
- **Nimi Gopalakrishnan**, Kaushal S. Sagar, Mads Brøkner Christiansen, Sokol Ndoni, Martin E. Vigild and Anders Kristensen.
  1, 2-Polybutadine nano-porous liquid core polymer waveguides.
  Oral presentation at: COMS, Copenhagen, Denmark (2009).